University of Alberta

Characterization of Suspended Frazil and Surface Ice in Rivers Using Sonars

by

Tadros Ibrahim Riad Ghobrial

A thesis submitted to the Faculty of Graduate Studies and Research
in partial fulfillment of the requirements for the degree of

Doctor of Philosophy

in

Water Resources Engineering

Civil and Environmental Engineering Department

Fall 2012
Edmonton, Alberta

Abstract

This research describes laboratory and field experiments aiming at developing techniques for obtaining quantitative measurements of suspended frazil ice and surface ice characteristics in rivers using sonars. A series of laboratory experiments were conducted to correlate the sonar backscatter signal from a high (546 kHz) and low (235 kHz) frequency units with direct measurements of frazil concentration. The sonar measurements showed that the high frequency unit is more sensitive to the presence of suspended frazil particles than the low frequency unit, especially at lower concentrations. A strong correlation was found between the acoustic relative backscatter from both sonar units and the measured concentrations. This calibration was conducted over a range of frazil mass concentrations between 0.012 and 0.135 % and the majority of observed frazil particles were disk shaped, varying in diameter from 0.25 to 4.25 mm.

An algorithm has been developed to measure surface ice characteristics using field data from the high and low frequency sonars, a 2 MHz current profiler, and a monitoring station, deployed on the North Saskatchewan River in the north east of Edmonton, AB, Canada, during the 2009/2010 freeze-up season. The validity and the accuracy of these measurements were tested and results are presented. Over the entire season, pans/rafts drafts ranging from 0.1 to 1.0 m and pan/raft lengths ranging from 0.6 to 8.0 m were measured. The sonar proved to be very accurate in detecting the exact surface ice conditions locally above the sonar beam.

Acoustic field data gathered during suspended frazil events have been processed and analyzed to provide estimates of frazil concentration and particle sizes using laboratory regression equations and fluid disk scattering model. In total, eight frazil events were detected with the sonars during the field deployment. Preliminary linkages between the meteorological (air and water temperatures) and surface ice conditions measured at the site, and the duration and magnitude of the detected frazil events are presented. Concentrations ranging between 0.01 and 0.05% and disk radii between 0.13 and 0.21 mm have been estimated from the field data.

Acknowledgments

I sincerely express my gratitude to my supervisors, Dr. Mark Loewen and Dr. Faye Hicks, whose expertise, understanding, and patience, added considerably to my graduate experience. I learned from them how to think critically, professionally and most of all how to conduct high quality research. I appreciate the long periods of time they spent on revisions and discussions to help improve the outputs of this research. I deeply thank Dr. Loewen for his day-to-day directions to my research and whose vast knowledge with laboratory instrumentations and data analysis was a major key to the success for this research. I'm very grateful to Dr. Hicks, one of Canada's leading river ice experts, who introduced me to the world of River Ice engineering, and because of her, I got the chance to work on one of the most demanding areas of research in this field. I'm very thankful to my supervisors for provided me with the opportunity to participate in several conferences and workshops and to interact directly with other ice researchers. I highly appreciate Dr. Peter Steffler, Dr. Mark Loewen, Dr. Faye Hicks, Dr. Steven Daly, Dr. Yang Liu, and Dr. Lorenz Sigurdson for sitting on the final oral examination committee and providing me with their valuable suggestions regarding my Ph.D. thesis.

This research was mainly funded by the Natural Sciences and Engineering Research Council of Canada (NSERC) through a Collaborative Research and Development (CRD) Grant and through NSERC Discovery Grants to Dr. Mark Loewen and Dr. Faye Hicks. I'm grateful for that support and the efforts that Dr. Loewen and Dr. Hicks did to assure continuous funding for me and my family during the entire PhD duration. Also I acknowledge the financial support and advices of the industrial partners: BC Hydro, Manitoba Hydro, Ontario Power Generation, CEATI International Inc., and ASL Environmental Sciences. I thank Professor Dave Sego and Christine Hereygers for providing access to the cold room facility at the University of Alberta, and Perry Fedun for his technical support in the laboratory setup. I also thank Chris Krath, Josh Maxwell, Robyn Andrishak, and David Watson, for their assistance with the field deployment, and Vincent McFarlane for helping me with the laboratory experiments during summer 2010. A special thanks to my friend Samy Soliman from the department of Electrical and Computer Engineering at the University of Alberta for helping me with MATLAB programming. I'm also grateful to H. Haag and M. Cummings from EPCOR for providing access to the deployment site.

My deepest appreciation and love goes to my wife and best friend, Mariam, for her never-ending support and unconditional love which gave me the confidence to complete this research to my best performance. I also want to express my love and

gratitude to my parents: my father Dr. Ibrahim Ghobrial for inspiring me to pursue my graduate studies since the first day of my undergraduate program, my mother Mary, my sister Irene, and my brother Riad, for the continuous prayers, support, love and encouragement they provided me through my entire life. I also extend my heartfelt thanks to my in-laws, relatives and friends who were always keen to be updated about my research and wished me luck all the time.

Finally, I express my sincerest gratitude to Jesus Christ my God who made this dream come true and was always giving me the strength and support especially during the darkest moments of my life.

Table of Contents

List of Tables

List of Figure

CHAPTER 1: Introduction

1.1 Background and Motivation

The first and most important stage of ice cover formation over northern rivers is frazil ice generation. Fig. 1.1 shows a schematic diagram of frazil ice evolution in rivers during freeze-up. If the air temperature is below 0°C for a significant period of time, the water body loses heat to the atmosphere until the water becomes supercooled (i.e. cooled to slightly below 0°C). Once seed particles of ice (e.g. snow, frozen water droplets) are introduced into turbulent supercooled flow, large quantities of frazil ice particles are created very quickly (Daly, 2008). Latent heat released by the production of new frazil particles causes the water temperature to rise again and reach ~0°C (Michel, 1978). Typically, frazil particles are disk shaped and range in diameter from a fraction of a millimeter up to several millimeters and from 1 to 100 μm in thickness (Martin, 1981).

In supercooled water, frazil particles are very adhesive (termed 'active' frazil), and tend to stick to each other and form frazil flocs. Eventually these frazil flocs reach a sufficient size for buoyant effects to overcome the entraining effects of fluid turbulence and they float to the surface and form frazil slush (Martin, 1981). As ice is less dense than water, a portion of the floating frazil slush is exposed above the water and soon freezes, creating 'pancake ice' (also known as 'pan ice' or 'frazil pans'), as illustrated in Fig. 1.1. Frazil pans frequently slide on top of one another during collisions, creating longer floating pan accumulations known as frazil rafts or floes (Tsang, 1982). Frazil pans/rafts can exceed 2 m in diameter and 1 m in thickness (Osterkamp and Gosink, 1983). As surface concentrations of frazil pans/rafts approach 100%, congestion occurs and 'bridging' becomes likely. Bridging is the phenomenon that occurs when congestion of ice floes becomes so severe that their movement ceases at a site along the river (Hicks, 2009). Typical bridging locations are at tight bends and at locations where the channel narrows,

such as between bridge piers, at natural flow constrictions, or at constrictions created by border ice growth (Beltaos, 1995).

Once bridging occurs, incoming pans lengthen the accumulation in the upstream direction. This may occur by juxtapositioning (pans configured edge to edge) or by hydraulic thickening caused by entrainment and/or under turning of surface ice (Dow Ambtman et al., 2011). In both cases, the leading edge of the ice accumulation propagates upstream, although the rate will be much higher in the case of juxtapositioning. After the frazil pans and rafts come to rest, the underlying frazil slush may also stop moving. However, if the mean water velocity and turbulence are strong enough, frazil slush may be dislodged and move along the underside of the stationary ice cover or become re-entrained in the flow (Shen and Wang, 1995).

Frazil ice particles often cause severe problems at hydraulic structures during freeze-up in rivers. They can form thick slush layers that interfere with navigation, block water intakes used for drinking water, manufacturing, and oil refining by accumulating over the intakes screens (Clark and Doering, 2006; Ettema et al., 2009). One of the most adverse impacts is the blockage of water intakes at hydroelectric power plants that can cause a complete shutdown of the generators for significant amounts of time. Many engineering solutions have been investigated and developed to minimize intake blockage by frazil ice (Daly, 1991). Reviews of frazil ice characteristics and mechanism of formation are available in the literature (Martin, 1981; Tsang, 1982; Ettema et al., 1984; Daly, 1984, 1994, and 2008); however, development of effective solutions to mitigate frazil ice problems has proven difficult because of a lack of accurate frazil ice concentration and particle size measurements in rivers. Also, numerical models (e.g. CRISSP, HEC-RAS, River2D) that have been widely used to study ice cover formation and progression (e.g. Andrishak and Hicks, 2008; Beltaos and Burrell, 2010; Shen, 2010), have never been validated with continuous surface ice field measurements; and, in these models frazil ice properties such as particles size and rise velocity are computed empirically, or treated as calibration parameters (Shen,

2002). The fundamental problem was that there was no practical and robust method to measure suspended frazil and surface ice characteristics during freeze-up in rivers.

A method to accurately measure frazil ice concentrations and surface ice properties (i.e. pans drafts, lengths, and surface concentration) in rivers would be very beneficial. For the first time, frazil ice formation and evolution theories (upon which numerical models are built) could be validated using field data. Hydroelectric power generation companies could use the system to monitor frazil ice concentrations near water intake structures in rivers; which would allow them to take remedial actions before concentrations reach critical levels and intakes become completely blocked. The method could also be used to provide real time measurements of surface ice drafts and concentrations that have the potential to interfere with navigation in rivers and canals.

Frazil concentrations observed in laboratory studies ranged between: 0.065 to 0.609% in a flume (Ettema et al. 2003); 0.10 to 0.17 % in a counter-rotating flume (Ye et al. 2004); and 0.012 % to 0.135 % in a frazil tank (Ghobrial et al., 2012). A number of methods have been developed to measure frazil ice concentration in rivers. These include methods based on: laser Doppler velocimetry (Schmidt and Glover, 1975); water conductivity (Tsang, 1985), pumping water samples (Lever et al., 1992), and electromagnetic pulses (Yankielun and Gagnon, 1999). However, thus far all of these have proven to be impractical for use in the field. Frazil concentration in rivers (often expressed as the number of particles per unit volume) was estimated to be in the order of 10^4 to 10^7 particles/m^3 (Osterkamp and Gosink, 1983; Daly, 1994). The only direct measurement of frazil ice concentration in the field was reported by Tsang (1984 and 1986) and ranged from 0 to 0.25% on the Beauharnois Canal, Quebec and from 0 to 0.03% on the Lachine Rapids on the St. Lawrence River, Quebec.

Frazil disk diameters ranging from 0.04 to 6.00 mm have been measured in laboratory experiments (Daly and Colbeck, 1986; Clark and Doering, 2006;

McFarlane et al., 2012) and it was found that the particles size distributions could be fitted by a log-normal distribution with a mean diameter ranging between 0.2 and 1.3 mm. Frazil particles sampled in rivers ranged between 0.1 and 5.0 mm in diameter (Osterkamp, 1978; Osterkamp and Gosink, 1982 & 1983; Wueben, 1984; Morse and Richard, 2009). However, in these field studies limited numbers of frazil particles were manually sampled and as a result there is large uncertainties associated with these measurements. Other than these grab sample measurements there have been no in-situ measurements of frazil ice particles size distribution in rivers that have been reported in the literature.

A variety of methods have been developed to monitor surface ice conditions (i.e. pan concentrations, pan sizes and ice cover formation) such as: observations by personnel (Calkins and Gooch, 1982; Osterkamp and Gosink, 1983; Michel, 1984), satellite remote sensing, such as RADARSAT (Weber et al., 2003; Tracy and Daly, 2003; Unterschultz et al., 2009), aerial photographs (Erb, 1986; Daly et al., 1986), and web-based cameras (Vuyovich et al., 2009). However, each method has its limitations: the observations by personnel is the most accurate but very costly and most of the time the sites are in remote areas that are very hard to access; satellite remote sensing using high resolution Synthetic Aperture Radar (e.g. RADARSAT 2) has the potential to provide good data on surface ice concentrations, however this application has not yet been explored extensively; the photographic methods require no fog, snow or condensation on the camera lenses, but these are a common problem in winter. Any of these methods cannot be used solely to provide a complete monitoring of freeze-up processes, especially that none of these methods can measure ice thicknesses. Accurate and continuous measurements of surface ice characteristics, such as pan formation and ice cover consolidation, are needed both for model validation, and to advance our fundamental understanding of these processes (Shen, 2010).

Ice Profiling Sonars (IPS) [ASL Environmental Sciences Inc., Canada] were originally developed in 1990 to measure ice drafts in the polar ocean regions (Melling and Riedel, 1995). A 420 kHz version of the IPS was used for the first

time to continuously monitor river ice (as opposed to sea ice) drafts and surface concentrations on the St Lawrence River, Quebec starting in the 2000/2001 winter season (Hessami and Morse, 2001; Morse et al., 2003; Richard and Morse, 2008a). A shallow water version of the Ice Profiling Sonar (SWIPS) [ASL Environmental Sciences Inc., Canada] designed to be installed on the river bed and to transmit acoustic pulses up through the water column for a maximum water depth of 20 m was introduced in 2004. The first generation of these sonars was available commercially in two acoustic frequencies: one low (235 kHz) and one high (546 kHz) frequency. These instruments have been deployed successfully in the Peace River, Alberta since the 2004/2005 winter season. These field studies showed that these sonar instruments can detect suspended frazil particles as well as surface ice drafts (Jasek et al., 2005). Jasek and Marko (2007) were able to extract time series measurements of ice drafts and surface ice concentrations on the Peace River using data from both low and high frequency SWIPS. A recent comparison of measured (using the SWIPS instrument) versus modeled (using the CRISSP model) surface ice characteristics by Jasek et al. (2011) showed that using calibrated model parameters, the CRISSP model predictions were in very good agreement with sonar measured drafts and surface ice concentrations. It is important to note that, an algorithm to compute ice drafts and surface concentration from sonar data have never been proposed; and continuous measurements of surface pan/raft lengths using sonar data have never been reported in the literature.

Jasek et al. (2005) were the first to report the detection of fresh water suspended frazil ice using a 235 kHz SWIPS in the Peace River, Alberta. Marko et al. (2006) described the simultaneous deployment of 235 and 546 kHz frequency sonars in the Peace River and found that the high frequency sonar was more sensitive to suspended frazil ice than the lower frequency sonar. Richard and Morse (2008b) used a 420 kHz IPS to detect suspended frazil events near a water intake on the St Lawrence River, Quebec. The severity and duration of the detected frazil events were linked to the possibility of ice blockage of the nearby water intake. Morse

and Richard (2009) used sonar data from a 420 kHz IPS to estimate profiles of relative frazil ice concentration (i.e. concentration in arbitrary units) since the relationship between the acoustic signal and the volumetric concentration was not known.

Researchers studying sediment transport and aquatic organisms in rivers and estuaries have been using acoustic backscatter measurements to estimate the concentration and particle sizes of suspended materials for more than two decades (e.g.: Greenlaw, 1979; Kristensen and Dalen, 1986; Thorne et al., 1993; Thevenot and Kraus, 1993). The acoustic pulses from the sonar are reflected by targets in the water column, and the intensity of the reflected signals is related to the type, size and number of the acoustic targets in the insonified volume (Urick, 1983). Two methods have been used to estimate particles sizes and concentrations from acoustic measurements. The first consisted of establishing regression equation between laboratory sampled concentrations, and the corresponding acoustic signal (Kristensen and Dalen, 1986). However, this method has never been applied to suspended frazil ice. The second method uses theoretical or empirical scattering models that have been developed for different target shapes (e.g. Rayleigh, 1896; Bowman et al., 1969; Stanton, 1989) to predict the particles sizes and concentration from the acoustic signal. This method was used by Marko and Jasek (2010a, b & c) and Richard et al. (2010) to estimate frazil characteristics from sonar data sampled during freeze-up. Marko and Jasek (2010a, b & c) used Rayleigh's (1896) scattering model for small spheres to estimate particle sizes and concentrations using data from both the high (546 kHz) and low (235 kHz) frequency sonars deployed in the Peace River. Richard et al. (2010) deployed a 420 kHz IPS, and a 1228 kHz ADCP in the St. Lawrence River, Canada. The sonar signals were analyzed using Johnson's (1977) scattering model for fluid spheres to estimate the frazil disk radii of the 'acoustically equivalent' spheres and the corresponding frazil concentrations. However, the model predictions presented in these studies could not be validated because in-situ measurements of suspended frazil ice properties were not feasible.

1.2 Research Objectives and Brief Methodology

The primary objective of this research was to develop a technique for obtaining quantitative measurements of suspended frazil ice, and surface ice characteristics using upward looking sonars. The specific objectives of the proposed study are to:

- Use laboratory experiments to determine an empirical relation between the backscattered sonar signals from suspended populations of frazil ice particles and frazil ice concentration.
- Develop an accurate algorithm to compute surface ice drafts, lengths, and concentrations from sonar data.
- Validate the algorithm by visual observations, time lapse photography, and direct measurements of surface ice characteristics in the field.
- Investigate the applicability of the empirical relations derived in the laboratory for estimating suspended frazil concentrations in the field.
- Investigate the applicability of theoretical acoustic scattering models for different particle shapes to estimate frazil ice concentrations and particle sizes.

In order to achieve the above objectives, a series of laboratory controlled experiments were conducted in a specially designed frazil ice tank located in the University of Alberta Cold Room Facility. Two shallow water ice profiling sonars: one low (235 kHz) and one high (546 kHz) frequency were deployed on the bottom of the frazil tank, and direct sieve measurements of frazil ice concentrations were correlated with the corresponding sonar backscatter signal. In addition, field experiments were conducted during the 2009/2010 freeze-up season on the North Saskatchewan River in Edmonton, Alberta. The high and the low frequency sonars, an acoustic Doppler current profiler, and an on-shore monitoring station equipped with digital cameras and temperature sensors were deployed at a site. This field data was used to develop and validate an algorithm that computes the drafts, lengths and surface concentrations of frazil pans and

rafts. During this field deployment, several frazil events were detected by the sonar. The laboratory regression equations were used to estimate frazil concentration from the field sonar data, and the scattering models were used to deduce the corresponding particle sizes.

1.3 Organization of the Thesis

This thesis is in paper format. Each chapter has its own introduction, literature review and list of references. Chapter 2 provides a detail description of the sonar instruments' specifications, principle of operation, and signal processing. Also it describes the experimental setup and the laboratory measurements of suspended frazil ice used to develop the empirical relation that correlate the sonar signal with suspended frazil concentration. Chapter 3 describes the field deployment program (site description, instrumentation, and setup) of the sonar units and presents an algorithm to compute surface ice characteristics from the sonar data. The calibration and validation of this algorithm is also discussed. This chapter also includes a detailed discussion of the freeze-up season and the factors affecting surface ice measured at the site. Chapter 4 presents a review of suggested theoretical scattering models, their applicability to the laboratory results and to the field detected frazil ice. Also the validity of the laboratory achieved correlations to estimate suspended frazil concentration in the field is discussed in this chapter. Conclusions and recommendations for future work were summarized in Chapter 5.

There are three appendices to the thesis: Appendix A describes a preliminary investigation of the porosity and sound speed of frazil slush layer in the laboratory. Appendix B presents results of a simplified heat transfer model to compute frazil concentration in the laboratory conditions. Appendix C contains all of the MATLAB programs developed in this study.

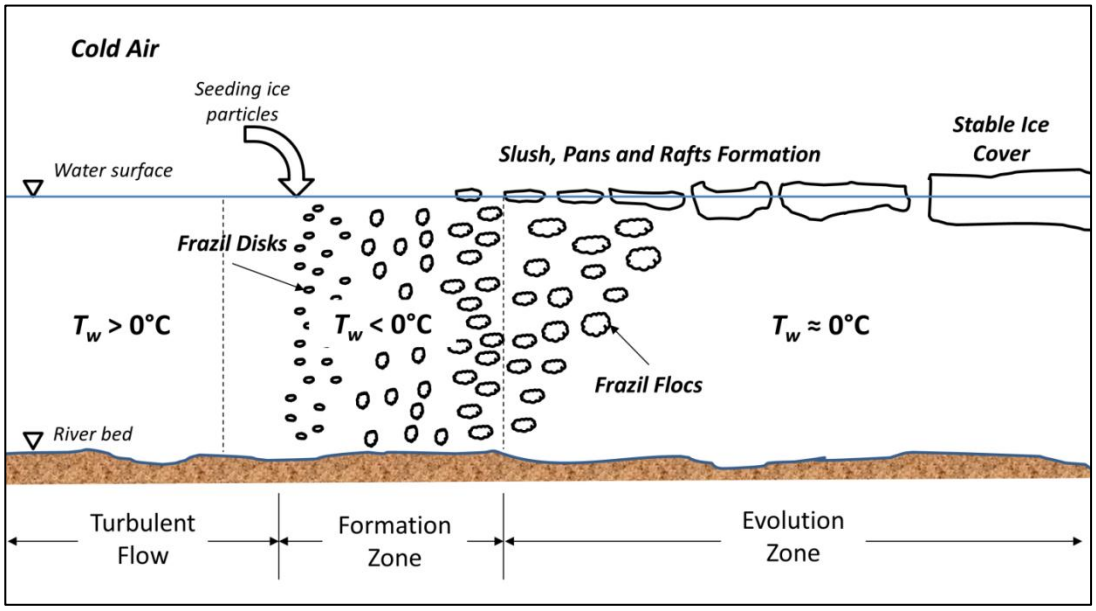

Fig. 1.1. Schematic diagram of frazil ice evolution in rivers during freeze-up, adapted from Michel (1978) and Daly (2008).

References

Andrishak, R. and Hicks, F.E., 2008. Simulating the Effects of Climate Change on the Winter Regime of the Peace River. Canadian Journal of Civil Engineering, 35: 461-472.

Beltaos, S., 1995. Rivers Ice Jams. Water Resources Publications, LLC, Colorado, USA. 372 pages.

Beltaos, S. and Burrell, B., 2010. Ice-Jam model testing: Matapedia River case studies, 1994 and 1995. Cold Regions Science and Technology 60, 29-39.

Bowman, J.J., Senior, T.B.A., Uslenghi, P.L.E. (Eds.), 1969. Electromagnetic and Acoustic Scattering by Simple Shapes. North-Holland, Amsterdam. 728 pp.

Calkins, D.J. and Gooch, G., 1982. Ottauquechee River - Analysis of freeze-up processes. Proceedings from the 2nd CRIPE Workshop, Edmonton, Alberta, 2-37.

Clark, S., and Doering, J.C., 2006. Laboratory Experiments on Frazil-Size Characteristics in a Counter Rotating Flume. Journal of Hydraulic Engineering, 132(1), 94-101.

Daly, S.F., 1984. Frazil ice dynamics. CRREL monograph 84-1. U.S. Army Corps of Engineers, Engineering Research & Development Center, Cold Regions Research and Engineering Laboratory, Hanover, N.H., 46 pp.

Daly, S.F., 1991. Frazil Ice Blockage of Intake Trash Racks. Cold Regions Technical Digest No. 91-1.

Daly, S.F., 1994. International Association for Hydraulic Research Working Group on Thermal Regimes: Report on Frazil Ice. U.S. Army Corps of Engineers Special Report 94-23. 43p.

Daly, S.F., 2008. Evolution of frazil ice, 19th IAHR International Symposium on Ice, Vancouver, BC, Canada, pp. 29-47.

Daly, S.F., and Colbeck, S., 1986. Frazil Ice Measurements in CRREL's Flume Facility. Proc. Syrup. Ice 1986. Int. Assoc. Hydraul. Res., Iowa City, Iowa, pp. 427--438.

Daly, S.F., Carey, K.L., Gatto, L., Anderson, V.H., and Arend, R., 1986. Mapping River Ice Conditions Using Videographic Techniques. Proceedings of the 4th Workshop on the Hydraulics of Ice Covered Rivers CRIPE, Montréal, Canada, pp. B-2.1 – B-2.14

Doering, J.C., and Morris, M.P., 2003. A Digital Image Processing System to Characterize Frazil Ice. Canadian Journal of Civil Engineering, 30: 1–10.

Dow Ambtman, K., P. Steffler and F. Hicks, 2011. Analysis of the Stability of Floating Ice Blocks", ASCE Journal of Hydraulic Engineering, 137(4): 412-422.

Erb, T.L., 1986. Aerial Photographic Interpretation of River Ice. Proceedings of the 4th Workshop on the Hydraulics of Ice Covered Rivers CRIPE, Montréal, Canada, pp. B-6.1 – B-6.15.

Ettema, R., Chen, Z., and Doering, J., 2003. Making Frazil Ice in a Large Ice Tank. Proceedings of the 12th Workshop on the Hydraulics of Ice Covered Rivers, Committee on River Ice Processes and the Environment, Edmonton, Canada, 13 pp.

Ettema, R., Karim, M.F., Kennedy, J.F., 1984. Laboratory Experiments on Frazil Ice Growth in Supercooled Water. Cold Regions Science and Technology, 10: 43-58.

Ettema, R., Kirkil, G., and Daly, S.F., 2009. Frazil ice concerns for channels, pump-lines, penstocks, siphons, and tunnels in mountainous regions. Journal of Cold Regions Science and Technology, 55: 202-211.

Ghobrial, T.R., Loewen, M.R., and Hicks, F.E., 2012. Laboratory calibration of upward looking sonars for measuring suspended frazil ice concentration. Cold Reg. Sci. Technol. (70): 19-31.

Greenlaw, C.F. 1979. Acoustical estimation of zooplankton populations. Limnology and Oceanography 24(2): 226–242.

Hessami, M., and Morse, B. 2001. Évaluation de la capacité des instruments ADCP et IPS à caractériser les paramètres de la glace. Canadian Coast Guard, Charlottetown, P.E.I.

Hicks, F.E., 2009. An Overview of River Ice Problems. invited paper, Journal of Cold Regions Science and Technology, Special Issue on River Ice, 55:175-185.

Jasek, M., Marko, J.R., Fissel, D., Clarke, M., Buermans, J., Paslawski, K., 2005. Instrument for detecting freeze-up, mid-winter and break-up processes in rivers. In Proceedings of 13th Workshop on Hydraulic of Ice-Covered Rivers, Hanover, NH. 34p.

Jasek, M., and Marko, J.R., 2007. Instrument for Detecting Suspended and Surface Ice Runs in Rivers. 14th Workshop on the Hydraulics of Ice Covered Rivers, Quebec City, Canada. 30p.

Jasek, M., Ghobrial, T.R., Loewen, M.R., Hicks, F.E., 2011. Comparison of CRISSP modeled and SWIPS measured ice concentrations on the Peace

River. In Proceedings of 16th Workshop on River Ice Winnipeg, Manitoba, pp 249-273.

Johnson, R. K., 1977. Sound scattering from a fluid sphere revisited, J. Acoust. Soc. Am., 61(2), 375-377. (Erratum: Sound scattering from a fluid sphere revisited, J. Acoustic. Soc. Am., 63(2), 626, 1978.)

Kristensen, A., and Dalen, J., 1986. Acoustic estimation of size distribution and abundance of zooplankton. J. Acoust. Soc. Am. 80 (2): 601- 611.

Lever, J., Daly, S., Rand, J., Furey, D., 1992. A Frazil Ice Concentration Meter. Proceedings of the 11th IAHR Symposium, Banff, Canada, 1362-1376 .

Marko, J.R., Fissel, D.B., Jasek M., 2006. Recent Developments in Ice and Water Column Profiling Technology. Proceedings of the 18th IAHR International Symposium on Ice, Sapporo, Japan, 8pp.

Marko, J.R., Jasek, M., 2010a. Sonar Detection and Measurements of Ice in a Freezing River I: Methods and Data Characteristics. Cold Regions Science and Technology. 63, 121–134.

Marko, J.R., Jasek, M., 2010b. Sonar Detection and Measurement of Ice in a Freezing River II: Observations and Results on Frazil Ice. Cold Regions Science and Technology. 63, 135–153.

Marko, J.R., Jasek, M., 2010c. Frazil Monitoring by Multi-frequency Shallow Water Ice Profiling Sonar (SWIPS): Present Status. Proceedings of the 20th IAHR International Symposium on Ice, Lahti, Finland, June 14 to 18, 2010.

Martin, S., 1981. Frazil ice in rivers and oceans. Annual Review of Fluid Mechanics, **13**: 379-397.

McFarlane, V., Loewen, M.R., and Hicks, F.E., 2012. Laboratory Experiments to Determine Frazil Ice Properties. Proceedings of the Annual General Conference of the Canadian Society of Civil Engineers, Edmonton, Alberta, Canada, June 6 to 9, 2012.10p.

Melling, H. and Riedel, D.A., 1995. The underside topography of sea ice over the continental shelf of the Beaufort Sea in the winter of 1990. J. Geophys. Res. 100(C7): 13641-13653.

Michel, B., 1978. Ice accumulations at freeze-up or breakup, Proceedings, IAHR Symposium on ice problems, Lulea, Sweden, pp. 301-317

Michel, B., 1984. Comparison of field data with theories on ice cover progression in large rivers. Canadian Journal of Civil Engineering, 11(4), pp. 798-814.

Morse, B., Hessami, M., Bourel, C., 2003. Characteristics of ice in the St. Lawrence River. Canadian journal of Civil Engineering 30, 766–774.

Morse, B., and Richard, M., 2009. A Field Study of Suspended Frazil Ice Particles. Cold Regions Science and Technology, Volume: 55, pp 86–102.

Osterkamp, T.E., 1978. Frazil ice formation: A review. Journal of the hydraulic division, ASCE, 104(HY9): 1239-1255.

Osterkamp, T.E., and Gosink, J., 1982. Selected Aspects of Frazil Ice Formation and Ice Cover Development in Turbulent Streams. Proceedings of the 2nd Workshop on the Hydraulics of Ice Covered Rivers, Edmonton, Alberta, pp. pp. 131-147.

Osterkamp, T.E., and Gosink, J., 1983. Frazil Ice Formation and Ice Cover Development in Interior Alaska Streams. Journal of Cold Regions Science and Technology, v 8 p 43-56.

Rayleigh, J., 1896. The Theory of Sound, Vol. 2 (Dover, New York, 1945).

Richard, M. and Morse, B., 2008a. Surface ice observations on the St. Lawrence River, Proceedings of the 19th IAHR International Symposium on Ice, Vancouver, Canada.

Richard, M. and Morse, B., 2008b. Multiple frazil ice blockages at a water intake in the St. Lawrence River. Cold Regions Science and Technology, 53(2): 131-149.

Richard, M., Morse, B., Daly, S.F. and J. Emond, 2010. Quantifying suspended frazil ice using multi-frequency underwater acoustic devices. River Research and Applications. DOI: 10.1002/rra.1446.

Schmidt, C.C., Glover, J.R., 1975. A Frazil Ice Concentration Measuring System Using a Laser Doppler Velocimeter. J. Hydraulic Research, 13(3): 299-314.

Shen, H. T., 2002. Development of a comprehensive river ice simulation system. 16th International Symposium on Ice, Dunedin, New Zealand, Vol. 1, 142-148.

Shen, H. T., 2010. Mathematical modeling of river ice processes. Cold Regions Science and Technology: 62, 3–13.

Shen, H.T. and Wang, D.S., 1995. Under cover transport and accumulation of frazil granules. Journal of hydraulic engineering (ASCE), 121(2): 184-195.

Stanton, T.K., 1989. Simple approximate formulas for backscattering of sound by spherical and elongated objects. J. Acoustic. Soc. Am. 86 (4) 1499-1510.

Svensson, U., and Omstedt, A., 1994. Simulation of supercooling and size distribution in frazil ice dynamics. Cold Regions Science and Technology, Volume: 22, Pages: 221-233.

Thevenot, M.M., and Kraus, N.C., 1993. Comparison of Acoustical and Optical Measurements of Suspended Material in the Chesapeake Estuary. J. Marine Environmental Engineering, 1: 65– 79.

Thorne, P.D., Hardcastle, P.J., and Soulsby, R.L., 1993. Analysis of Acoustic Measurements of Suspended Sediments. Journal of Geophysical Research, vol:98, No: C1, pages:899-910.

Tracy, B. T., and Daly, S. F., 2003. River ice delineation with RADARSAT SAR. Proc., 12th Workshop on the Hydraulics of Ice Covered Rivers, CGU HS Committee on River Ice Processes and the Environment, Edmonton, Alta., Canada.

Tsang, G., 1982. Frazil and anchor ice : a monograph. Subcommittee on Hydraulics of Ice-Covered Rivers. NRC Subcommittee on Hydraulics of Ice Covered Rivers, Ottawa, Ont., iv, [93] p.

Tsang, G., 1984. Concentration of frazil in flowing water as measured in laboratory and in the field. Proceedings of the 7th IAHR Ice Symposium, 1984, Hamburg, Germany.

Tsang, G., 1985. An Instrument for Measuring Frazil Concentration. Cold Regions Science and Technology, Volume: 10, Issue: 3, Pages: 235-249

Tsang, G., 1986. Preliminary report on field study at Lachine Rapids on cooling of river and formation of frazil and anchor ice. Proceedings of the 4th Workshop on the Hydraulics of Ice Covered Rivers, Montréal, Canada, pp. F5.1-5.51.

Unterschultz, K., Van der Sanden, J., and Hicks, F.E., 2009. Potential of RADARSAT-1 for the Monitoring of River Ice: results of a case study on the Athabasca River at Fort McMurray, Canada. Journal of Cold Regions Science and Technology, Special Issue on River Ice, 55:238-248.

Urick, R.J., 1983. Principles of Underwater Sound. 3rd Edition. McGraw-Hill, Inc., 423 pp.

Vuyovich, C.M., Daly, S.F., Gagnon, J.J., Weyrick, P., Zaitsoff, M., 2009. Monitoring River Ice Conditions Using Web-Based Cameras. Journal of Cold Regions Engineering, Vol. 23, No. 1, pp 1-17.

Weber, F., Nixon, D., and Hurley, J., 2003. Semi-automated classification of river ice types on the Peace River using RADARSAT-1 synthetic aperture (SAR) imagery. Canadian Journal of Civil Engineering, 30(1), 11-27.

Wueben, J.L., 1984. The rise pattern and velocity of frazil ice, CRIPE, Proceedings of the 3rd Workshop on the Hydraulics of Ice Covered Rivers, Fredericton, NB.

Yankielun, N., Gagnon, J., 1999. Laboratory Tests of a Time-Domain Reflectometry System for Frazil Ice Detection. Canadian Journal of Civil Engineering, 26: 168–176.

Ye, S.Q., Doering, J.C., Shen, H.T., 2004. A Laboratory Study of Frazil Evolution in a Counter Rotating Flume. Canadian Journal of Civil Engineering, 31(6), 899-914.

CHAPTER 2: Laboratory Calibration of Sonars for Measuring Suspended Frazil Ice Concentration[1]

2.1 Introduction

Frazil ice particles often cause severe problems at hydraulic structures during freeze-up in rivers. Active frazil readily adheres to trash racks and screens, blocking municipal and industrial water intakes. Frazil can also form thick slush layers that interfere with navigation or can precipitate freeze-up ice jams. A key factor limiting our ability to predict river ice cover development processes, and to design appropriate mitigation schemes, is the inability to actually measure suspended frazil ice particle concentrations in rivers. Many methods for measuring frazil ice concentrations have been investigated, including techniques based on: changes in electrical conductivity (Tsang, 1985); laser Doppler velocimetry (Schmidt and Glover, 1975); pumping water samples (Lever et al,. 1992); electromagnetic pulses (Yankielun and Gagnon, 1999); underwater photography (Daly and Colbeck, 1986) and image processing systems (Doering and Morris, 2003). However, none of these methods have been proven sufficiently accurate or robust for use in the field. Thus at present, there is no practical method to measure suspended frazil ice concentrations during freeze-up in rivers.

An upward looking sonar; called the Shallow Water Ice Profiling Sonar (SWIPS) [ASL Environmental Sciences Inc., Canada] was originally developed to measure ice drafts in rivers. This device is designed to be installed on the river bed and to transmit acoustic pulses up through the water column. The acoustic signals are reflected by targets in the water column and the intensities of these reflected signals are used to differentiate between different targets types. Currently shallow water ice profiling sonars with two different acoustic transmitting frequencies are

[1] A slightly modified version of this chapter was published in the journal of Cold Reg. Sci. Technol. (70): 19-31

available commercially: a low frequency unit (235 kHz) and a high frequency unit (546 kHz).

Ice profiling sonars have been deployed successfully in the Peace River, Canada each winter since 2004-2005 (Jasek et al., 2005).Those field studies were the first to show that the 235 kHz unit could detect the presence of suspended frazil ice; however, they found that the acoustic returns from suspended frazil particles were somewhat weak at this frequency. Marko et al. (2006) described the simultaneous deployment of the 235 and 546 kHz frequency units in the Peace River. They found that the high frequency sonar was more sensitive to suspended frazil ice than the lower frequency sonar. However, they observed that the lower frequency unit was better for measuring slush layer properties.

Richard and Morse (2008) used a 420 kHz Ice Profiling Sonar (IPS) designed for deep water use, to monitor frazil ice blockage at a water intake in the St. Lawrence River. Morse and Richard (2009) conducted a detailed study of hydraulic, meteorological and ice data on the St. Lawrence River. In this study sonar data from the 420 kHz IPS was used to estimate relative frazil ice concentrations (i.e. concentration in arbitrary units) since the relationship between the acoustic signal and the frazil concentration was unknown. Marko and Jasek (2010a, b & c) monitored surface ice growth and relative changes in frazil concentration using sonar data from both the high and low frequency units deployed in the Peace River. They used the ratio of the signal strength from the high and low frequency sonars to estimate frazil ice particle diameters using Rayleigh's (1896) scattering theory for small spherical particles. Richard *et al.* (2010) deployed a 420 kHz IPS and a 1228 kHz ADCP in the St. Lawrence River, Canada, and used the ratio of the acoustic signal to estimate frazil ice concentration and particles diameters using Johnson's (1977) scattering theory.

The objective of this study was to investigate whether it is possible to calibrate the shallow water ice profiling sonar to quantitatively measure frazil ice concentration in rivers. To achieve this, a laboratory study was conducted in the Civil

Engineering Cold Room Facility at the University of Alberta. The experiments consisted of generating frazil ice in a turbulent tank while deploying both the high and low frequency sonars to detect the suspended frazil ice particles. Preliminary results from this study, reported by Ghobrial et al. (2009), showed that a correlation does exist between frazil concentration and the intensity of the raw sonar signals.

2.2 Sonar Instrument

2.2.1 Principle of Operation

The ice profiling sonar transmits acoustic pulses into the water column at a specific frequency and records the intensity of reflected sound at the transducer as function of time with respect to the transmitted pulse. For monostatic sonars (i.e. transmitter and receiver are in the same transducer) such as these; the reflected sound from targets is referred to as the backscattered sound (Urick, 1983). The instrument records the time for the acoustic pulse to be transmitted to, and reflected from, an insonified target and converts this into range (distance) above the transducer as follows,

$$R = \frac{c \times t}{2} \tag{2.1}$$

where R is the range in meters (m), t is the time after transmission, in seconds (s), at which the echo arrives and c is the sound speed in water (m/s) that can be specified by the user.

Fig.2.1 presents a schematic diagram of the signal path through the ice profiling sonar's electronics. The supply input voltage is first transmitted through a pulse generator, then through a power amplifier, before it arrives at the piezoelectric transducer. The transducer then emits sound pressure waves into the water column with a user specified pulse length, τ, which is the duration of the transmitted pulse. The sound waves are then reflected by the insonified targets and backscattered sound arrives back at the transducer where the pressure amplitude is

converted to a voltage signal. This voltage signal then passes through a band pass filter and then a Time-Varying Gain (TVG) board. The TVG board amplifies the backscattered signals as a function of time (i.e. range) to approximately compensate for losses due to spherical spreading of the acoustic beam and absorption of the sound in the water (Lemon et al., 2008). Both sonar units are equipped with variable gain boards. A gain level can be selected from 1 to 4 to adjust the amount of amplification applied to the signal at the receiver. The TVG is an analog circuit and the amplification it provides is based on an assumed speed of sound and absorption coefficient; therefore, its compensation for spreading and absorption losses is only approximate. Further corrections must be implemented by adjusting the medium absorption coefficient and sound speed (Lemon et al., 2008).

After amplification by the TVG, the signal passes through an envelope detector to a 16-bit A/D (analogue to digital) converter. The A/D converter converts the signal amplitude in volts to raw digital counts, N_r, ranging from 0 to 65535 (16-bit). The raw counts were then processed to correct for a number of factors, including the TVG effect and signal losses, and produce calibrated results.

2.2.2 Specifications

Detailed calibrations of both sonars were performed by the manufacturer and the results of these tests and the transducer specifications are summarized in Table 2.1. The instruments can ping (emit a sound pulse) at rates as fast as 1 Hz and have a maximum sampling rate of 64 kHz which corresponds to a cell size of 0.011 m and an accuracy of ± 0.05 m for ice target measurements (Buermans et al., 2010). For the beam-width and transducer diameter listed in Table 2.1, at a water depth of 1.0 m centred above the transducer head, the sampling volume was averaged over a cylinder of approximately 23.54 cm and 42.47 cm in diameter (in the horizontal direction) for the high and the low frequency units, respectively; and 1.1 cm in height (i.e. the cell size in the vertical). This implies that spatial variations less than those numbers in both the horizontal and the vertical

directions will not be detected. The travel time the signal takes to reach the surface and be reflected back to the transducer is approximately 1.4×10^{-3} sec. Variations in the composition of the sampling volume within this time scale is negligible when compared to the mean river velocity of 0.5 m/s or the sampling frequency of 1 sample/sec (1 Hz).

The user specifies the maximum range at which the units receive and record acoustic echoes. The pulse length, τ, can be varied between 10 and 1000 μs. The instrument is equipped with a tilt sensor (range ± 20º, accuracy ± 1.0º, precision 0.1º), a temperature sensor (accuracy 0.1 ºC, precision 0.01 ºC), and an absolute pressure sensor (range 0-206 kPa, accuracy ± 0.2 kPa). The instrument electronics are installed in a steel pressure case that is 25 cm long, 15 cm wide and 15 cm deep.

2.2.3 Signal Pre-Processing

Two pre-processing steps were applied to the raw counts, N_r, to correct for two factors. The first step was to correct for non-linearity of the envelope detector and the second was to correct for differences in the frequency response of the high and low frequency sonars' receiver electronics. The acquisition software supplied by the manufacturer assumes that the envelope detector behaves linearly (i.e. that there is a linear relationship between the received input voltage and the detected output voltage). However, upon measuring input and detected voltages simultaneously, the manufacturer found that the envelope detector was behaving non-linearly at low input voltages. This test data was used to create a table of raw count corrections as a function of input voltage that was then used to correct for this nonlinear behaviour.

In order to quantitatively compare the calibrated output of the high and low frequency sonars, the two instruments must have the same frequency response. However, the manufacturer measured the step responses of the receiver electronics of the two sonars and discovered that the 546 kHz sonar had a faster

frequency response compared to the 235 kHz sonar. Therefore, a second pre-processing step was required to ensure the data from both instruments had the same frequency bandwidth. The measured step responses were used to compute the transfer functions of the two receivers. The transfer functions were used to design a low pass filter that was applied to the high frequency sonar data to reduce its bandwidth so that it matched the low frequency sonar data.

2.2.4 Signal Processing

To convert the pre-processed counts, *N*, into calibrated units, the transducer specifications and the calibration data must be used. The calibrated quantity of interest is the volume backscatter strength, S_v, as it can be analyzed for information about the suspended particle concentration and size distribution (Urick, 1983). S_v is expressed in decibels (dB) per unit volume and is given by,

$$S_v = 10\log_{10}\left(\frac{I_r}{I_i}\right) \tag{2.2}$$

where I_r (W/m^2) is the reflected acoustic intensity and I_i (W/m^2) is the incident acoustic intensity. The acoustic intensity is defined as the rate at which acoustic energy passes through a unit area perpendicular to the direction of propagation (Leighton, 1994). Note that the acoustic intensity is proportional to the square of the sound pressure amplitude.

The sonar transducer records the Echo Level, *EL* (dB), which is the intensity of backscattered sound at the transducer. *EL* is related to S_v by the sonar equation (Urick, 1983) as follows,

$$EL = SL - 2TL + S_v + 10\log_{10}(V_{geo}) \tag{2.3}$$

where *SL* (dB) is the source level defined as the intensity of sound emitted by the transducer, *TL* (dB) is the one way transmission loss of sound in the water, and

V_{geo} is the insonified geometric volume created by the sound pulse at a specific range (m^3). *EL* is also given by,

$$EL = 10\log_{10}\left(\frac{P_r}{P_\circ}\right)^2 \tag{2.4}$$

where P_r is the reflected sound pressure at the receiver (Pa) and P_o is a reference pressure 1.0 m away from the receiver (usually taken as 1 µPa) (Clay and Medwin,1977). The transducer converts the reflected pressure P_r at the receiver to an electrical signal in volts. Using a logarithmic scale, the factor β for converting the recorded counts to detector voltage, consists of two components: the conversion from peak-to-peak voltage ($V_{p\text{-}p}$) to root mean square voltage (V_{RMS}) and theA/D scaling. The relation between $V_{p\text{-}p}$ and V_{RMS} is given by,

$$V_{p-p} = 2\sqrt{2}V_{RMS} \tag{2.5}$$

The analog to digital scaling factor for both sonars is 65535 counts for 2.5 volts full-scale input (personal communication with David Lemon, ASL Environmental Inc.). Therefore the factor β is a constant and can be calculated as follows,

$$\beta = 20\log_{10}\left(\frac{65535}{2.5}\times 2\sqrt{2}\right) = 97.4\,\text{dB} \tag{2.6}$$

Eq. (2.4) is then modified to include the transducer receiving response to the applied sound pressure and the factor β (Buermans et al., 2010) as follows,

$$EL + OCV + \beta = 20\log_{10}(P_{Vr}) \tag{2.7}$$

where, *OCV* (the Open Current Voltage) is the transducer receiving response in (dB), and P_{Vr} is the sound pressure at the receiver, expressed in terms of the voltage produced by the transducer relative to a pressure wave of 1.0 µPa. P_{Vr} is given by

$$P_{Vr} = \frac{N}{g[R]} \tag{2.8}$$

where, N are the pre-processed digital counts, and $g[R]$ is the total amplification applied to the signal (gain at the receiver) as a function of range (Buermans et al., 2010).

Using Eq. (2.7) and (2.8), *EL* can be expressed as,

$$EL = 20\log_{10}(N) - G[R] - OCV - \beta \tag{2.9}$$

where $G[R] = 20\log_{10}(g[R])$, is the receiver gain (dB) as a function of range that was measured by the manufacturer during the calibration tests (i.e. the so-called gain curves).

The source level *SL* (dB) is a function of the applied voltage to the transducer and is given by,

$$SL = TVR + 20\log_{10}(V_{Tx}) \tag{2.10}$$

where, *TVR*(dB) is the Transmit Voltage Response of the transducer, and V_{Tx} is the actual RMS voltage (V_{RMS}) applied to the transducer as a function of the supply voltage (Safari and Koray, 2008). *TVR* is the sound pressure, in dB, that the transducer emits for an applied RMS voltage of 1.0 V_{RMS}. The manufacturer calibrated both sonar transmitters, and provided V_{Tx} values as a function of the supply voltage (V).

The transmission loss *TL* (dB) is due to the spherical spreading of the beam and the absorption of the sound in the water. *TL* for one trajectory is calculated as,

$$TL = 20\log_{10}(R) + \alpha R \tag{2.11}$$

where α is the absorption coefficient expressed in dB/m (Urick, 1983). For fresh water at ranges as short as 1.5 m (maximum range in the frazil ice laboratory

tank), or even in shallow river water (~2.5 m deep), the absorption effect will be negligible (Ainslie and McColm, 1998).

The insonified geometric volume V_{geo} (m^3) is given by,

$$V_{geo} = \frac{1}{2} c \tau \psi R^2 \tag{2.12}$$

where τ is the user specific pulse length (s), and ψ the transducer beamwidth defined as the angle separating the two -3 dB points on opposite sides of the sonar transducer beam pattern expressed in steradian (Sr) (Urick, 1983). Backscattered signal power levels are proportional to the pulse length, which is the duration of the transmitted pulse. Therefore, shortening the pulse length decreases the power of the emitted signal. A pulse length of 68 μs is recommended by the manufacturer for field deployments to ensure that enough energy is emitted in the acoustic pulse to overcome signal losses.

Using Eqs. (2.3) through (2.12), the volume backscatter strength, S_v (dB) at a range, R, can be calculated as a function of pre-processed digital count, N, as follows (Lemon et al., 2008),

$$\begin{aligned} S_v &= 20\log_{10}(N) - G[R] - OCV - \beta - TVR - 20\log_{10}\left(V_{Tx}\right) \\ &+20\log_{10}(R) + 2\alpha R - 10\log_{10}\left(\frac{1}{2} c \tau \psi\right) \end{aligned} \tag{2.13}$$

S_v calculations are accurate to within ± 1.5 dB when using the transducer calibration data provided by the manufacturer (personal communication David Lemon, ASL Environmental Sciences).

If a single target or particle exists in the insonified volume, S_v is expressed as,

$$S_v = 10\ \log_{10}\left(\frac{\sigma_{bs}}{A_{ref}}\right) \tag{2.14}$$

where, σ_{bs} (m^2) is the acoustic backscatter cross-sectional area at a distance of 1.0 m from the target's acoustic center, and A_{ref} is a reference area (usually taken as 1 m^2). The backscatter cross section, σ_{bs}, is the ratio of the power reflected by the target (W) to the incident intensity, I_i (W/m^2). In other words, it is the area which, when multiplied by the intensity, equals the power removed from the incident wave and reradiating in all directions. σ_{bs} is a function of the particle size and shape, as well as the particle density and compressibility relative to the medium (Urick, 1983).

If a population of targets (particles) exists within the insonified volume (e.g. multiple frazil particles), S_v (dB) can be expressed in terms of the volume backscattering coefficient s_v (m^{-1}) as follows,

$$S_v = 10 \log_{10}(s_v R_o) \tag{2.15}$$

where R_o is a reference distance (usually 1 m), and s_v is the volume backscatter coefficient or backscattering cross sectional area per unit volume (m^{-1}) for a population of particles (Clay and Medwin,1977). Note that s_v is the linear form of the volume backscatter strength, S_v, and can be arithmetically averaged in time or space.

In the case of multiple particles, the scattering cross sections of individual particles are simply summed. Therefore, s_v at a specific range R (m) can then be expressed as,

$$s_v = \sum_i \left(N_{vi} \sigma_{bs_i} \right) \tag{2.16}$$

where N_{vi} is the number of the ith size of particles per unit volume (m^{-3}) having a backscatter cross section of σ_{bsi} (m^2). This concept is only valid under the condition that individual particles are not in close proximity to each other, such that their scattering fields do not interfere. If the particles are close enough together for their scattering fields to interact (e.g. a high concentration of frazil

particles), the resonance curve of a single particle is broadened and the scattering cross section of a group of particles is less than the sum of individual cross sections (Clay and Medwin,1977).

The objective of this study is to relate the backscattered sonar signals to measured suspended frazil concentrations. Researchers studying sediment transport in rivers and estuaries have been using acoustic backscatter measurements to estimate suspended sediment concentration for more than two decades (e.g.: Thorne et al.,1991; Thevenot and Kraus, 1993). It is not possible to measure and quantify all the acoustic and material characteristics of suspended material required to directly model the volume backscatter strength S_v for particles concentrations (Thevenot et al., 1992; Reichel and Nachtnebel, 1994). As a result, assumptions and simplifications to the problem must be invoked. Following the approach reported by Thevenot *et al.* (1992), the sonar equation can be rewritten as,

$$RB = EL + 2TL = SL + 10\log_{10}(V_{geo}) + S_v \qquad (2.17)$$

where RB (dB) is the relative backscatter. At a given range R, the relative backscatter RB is shifted from the volume backscatter strength S_v by a constant that is a function of the transducer source level and beam width. Accordingly, this constant is different for the high and low frequency sonar units. This approach assumes that the population of particles are homogeneous (i.e. have the same material characteristics), are uniform in shape, and are all the same size. Therefore, the backscatter cross section σ_{bs} is a constant value and, from Eq. (2.16), the volume backscatter coefficient s_v is directly proportional to the number of particles per unit volume, N_v. For particles of uniform size, N_v is directly proportional to particle mass or volume concentration, C and, the volume backscatter strength S_v (dB) is proportional to $\log_{10}(C)$. After appropriate substitutions, Eq. (2.17) can be written in terms of concentration C and relative backscatter RB (dB) as,

$$RB = K_1 + K_2 \times \log_{10}(C) \qquad (2.18)$$

where K_1 is a constant that includes terms for the source level and insonified volume; and K_2 is a constant that includes terms for the volume backscatter strength and the particles mass or volume. To estimate the concentration, Eq. (2.18) can be rearranged as follows,

$$C = 10^{(n+m*RB)} \tag{2.19}$$

where n and m are intercept and slope terms, respectively, that are determined by regression of RB with known C (Gartner, 2002 and 2004). According to the model proposed by Thevenot et al. (1992), S_v is proportional to $\log_{10}(C)$. In Eq. (2.13), at a given range, R, all of the transducer dependent parameters are constants; accordingly, S_v is proportional to $\log_{10}(N^2)$. Therefore, C is proportional to the square of the pre-processed counts, N^2, and to the square of reflected pressure, P_r^2.

2.3 Experimental Setup

The frazil experiments were conducted using a frazil ice tank located in the University of Alberta Cold Room Facility. The cold room is approximately 10 m long by 3 m wide and the air temperature can be varied between +20 °C and -40 °C with ± 2 °C fluctuations. Fig. 2.2 (a) shows a photograph of the custom made frazil ice tank inside the cold room facility. The minimum water depth required for the sonar to operate correctly, and to sample sufficient suspended frazil particles was approximately 1.0 m, therefore the tank depth was set to 1.5 m. Preliminary acoustic tests showed that for a water depth of 1.5 m, a minimum tank width of 0.8 m was needed to avoid acoustic reverberation from the tank side walls. Therefore, the tank was built 0.8 m wide and 1.2 m long. Tempered glass, 19 mm thick (selected because of its excellent optical qualities, resistance to scratching and high tensile strength) was used for the two 1.2 m by 1.5 m side walls to allow imaging and viewing of the frazil ice. Stainless steel plates, 6 mm in thickness, were used for the other two side walls and the tank bottom. This material ensured that corrosion would not be a problem and facilitated the

installation of drains, and connections for mixing propellers. The tank frame was constructed using 75 mm steel channel sections.

As Fig. 2.2 (b) shows, the sonar instruments were mounted on the bottom of the tank pointing upwards, and were held in place with a Plexiglas base plate. Eight, 25 cm diameter plastic trolling motor propellers [Minn Kota, MKP-33Weedless Wedge 2, USA] were used to produce turbulence, two on each side wall and four on the bottom. Four variable speed [Pacific Scientific Inc., NEMA 34 DC, USA] electric motors (1/3 H.P., 15.4 kg.cm of torque, max speed 1750 rpm), were used to drive the propellers. A laser tachometer was used to precisely control the motor speed in order to vary the intensity of the turbulence in the tank. The four electric motors could be attached to any of the 8 propeller couplers, thus making it possible to optimize the turbulence generated inside the tank. Preliminary tests using 3 mm diameter polystyrene beads (specific gravity of 1.04) showed that using only the four bottom propellers produced the most uniform mixing and minimized air bubble entrainment at the surface (which was necessary since air bubbles corrupt the sonar signals). Hollow PVC tubes were used to secure the instruments cables to prevent them from being caught in the propellers or interfering with the sonar signals.

The high and low frequency sonar units were each connected to a personal computer (PC), located outside of the cold room, using 10 m long data cables. Both PCs were equipped with IPS5Link software [ASL Environmental Sciences Inc., Canada] that was used to communicate with the sonars and to set the various sonar parameters such as the pulse length, gain level, sound speed and ping frequency. The tank was filled with tap water and the water temperature was recorded using the high frequency sonar's thermometer. An RTD (Resistance Temperature Detector) electronic thermometer [Fisher Scientific Inc., Traceable RTD Platinum Thermometer, USA], (accuracy ± 0.2 ^{o}C, and resolution of 0.01 ^{o}C) connected to a third PC, was used to record the air temperatures in the cold room. The clocks on the three PCs, and thus the instruments, were synchronized to within one second before each experiment.

The tank was positioned in the cold room between two freezer fans. Ice particles blowing from the cold room freezer fans most likely seeded the supercooled water and initiated frazil formation at different supercooling durations and temperatures. The frazil concentration in supercooled water depends principally on the initial ice seeding volume and the temperature of supercooling at the instant of seeding (Ettema et al., 1984). During the frazil experiments, the initial frazil seeding concentration could not be controlled due to the large size of the experiments.

2.4 Experimental Procedures

2.4.1 Preliminary Experiments

A total of 19 preliminary experiments were conducted to determine the correct sonar settings and to optimize experimental procedures. Different propellers speeds ranging from 100 to 800 rpm were tested and it was found that a speed of 300 rpm was optimum. This speed was high enough to ensure that skim ice did not form on the water surface, but was not so high that air bubbles became entrained. The effect of the cold room air temperature on frazil production was tested at -5,-10, -15 and -20 °C. At -15 and -20 °C the rate of frazil production was very large and the frazil concentration reached a maximum value too rapidly, such that surface skim ice started to form immediately after the propellers were stopped. At -5 °C the frazil concentrations produced did not vary much from one experiment to another. A value of -10 °C was found to be optimal because the rate of frazil production was slow enough to allow time for manual measurements to be conducted and a wide range of final concentrations could be generated. Each experiment was ended at different timing in order to achieve different suspended frazil concentrations.

Direct measurements of frazil ice mass concentration were made using a sieving technique. Three 15.5 cm diameter stainless steel sieves, having a cross sectional area of 0.019 m^2 and mesh size of 1.8 mm, were used for sampling. Three samples were taken from different quadrants of the tank during each test. Sieves with smaller mesh sizes (150 to 750 µm) were tested but they drained too slowly, and

the samples froze before they had drained completely. In order to eliminate any bias error in the sieving measurements caused by capillary water attaching to the mesh of the sieve, 30 sieving experiments were conducted at zero ice concentration (i.e. no frazil ice was present). From these tests, the mass of the water adhering to the sieves was found to range between 5.20 and 8.90 g, with an arithmetic mean of 7.20 g and a standard deviation of 0.92 g. This average adhered ice mass was then subtracted from the measured ice mass to determine the net mass of sieved frazil ice for each sample.

The acoustic pulse length and the gain setting are the main user adjustable parameters affecting the amplitude of the backscattered signal from the sonar units. The preliminary experiments showed that using a pulse length of 68 μs and the maximum gain of four for the low frequency sonar still produced relatively low amplitude returns from suspended frazil. The experiments also showed that, for the high frequency unit, a gain of one and a pulse length of 17 μs were needed to avoid signal saturation. A sound speed of 1403 m/s was used for both units, assuming fresh water at 0 ºC. The maximum ping rate of 1.0 Hz was used for both sonar transducers and sensor data was also collected at the same rate. Table 2.2 summarizes the sonar parameters used during the experiments.

2.4.2 Frazil Experiments

The same procedure was followed during each frazil experiment. First the cold room temperature was set to -10 ºC and the four bottom mounted propellers were set to rotate at 300 rpm. Both sonar units were deployed (i.e. data acquisition was initiated) using the settings summarized in Table 2.2. The water was continuously mixed until it supercooled and frazil ice particles began to appear in the water. The experiment was allowed to run until the frazil ice concentration in the tank reached a specified value (low, medium, or high) based on visual observations. Once the desired concentration of suspended frazil was reached, the propellers were turned off, sonar data acquisition was stopped and independent measurements of frazil concentration and particle sizes were conducted.

The sieving technique was used for direct measurements of frazil concentration. Before the surface started to freeze, the three sieves were lowered down to the tank bottom using strings, moved to an undisturbed spot, and then pulled up vertically to the water surface as illustrated in Fig. 2.3. Each sample was then weighed on a scale [Sartorius, BP12000S, USA] with a resolution of 0.01 g. This sampling method assumed that each sieve collected all the frazil ice particles from a volume of water equal to the area of the sieve times the height of the water column being sieved (see Fig. 2.3). The three sieved samples were weighed and averaged and the mass concentration C (%) of frazil ice was then calculated using the following equation

$$C = \frac{M_i - 7.2}{M_{tot}} \times 100 = \frac{M_i - 7.2}{\rho_w \times V_w + M_i} \times 100 = \frac{M_i - 7.2}{\rho_w \times V_{tot} + (1 - \frac{\rho_w}{\rho_i}) \times M_i} \times 100 \quad (2.20)$$

where M_i is the average ice mass collected by the three sieves (g), ρ_i is the ice density (0.92 g/cm^3), M_{tot} is the total mass (g), V_{tot} is the total volume (cm^3) of water plus ice in the sieved water column, ρ_w is the water density (1 g/cm^3) and V_w is the water volume (cm^3). The sieved water depth was maintained at approximately 1.25 m during each experiment, thus Eq. (2.20) reduces to,

$$C = \frac{(M_i - 7.2)}{23750 - 0.087 \times M_i} \times 100 \quad (2.21)$$

To independently determine the size and shape of the frazil ice particles, samples of the sieved frazil ice were examined under a microscope [Carl Zeiss, SteREO Discovery V.8, Germany]. The microscope was located inside the cold room to avoid melting the samples. Metal tweezers were used to sample frazil particles from the sieve and place them carefully on a microscope viewing slide. For scaling purposes, a clear plastic ruler was taped to the viewing slide with approximately 6 mm of the ruler scale visible. The microscope was equipped with a digital camera mounted directly to the viewing lens to enable direct imaging of the magnified particles.

2.5 Results and Discussion

Following the preliminary testing, a total of 47 complete frazil experiments were conducted. During each experiment, the coefficient of variation (*COV*) of the three sieve samples masses was calculated and frazil experiments with sieve samples having a $COV > 0.2$ were rejected. This value of the *COV* was selected to minimize the effect of anomalous sieve samples on the final frazil concentrations estimates. At concentrations higher than 0.15 %, frazil flocculation was observed in the tank and frazil flocs began sticking to the tank walls and floating to the surface. Flocs have very complex shapes and are much larger in size than individual particles. As a result the acoustic backscatter from suspended flocs was expected to be significantly different than from suspended frazil ice particles. In order to avoid this additional complexity, frazil experiments with concentrations greater than 0.15%, were excluded from further analysis. This screening eliminated 13 frazil experiments, leaving 34 successful experiments. Occasionally, one of the sonar units (either the high or low frequency) failed to acquire data during an experiment. This happened twice for the high frequency sonar and three times for the low frequency sonar. Therefore, there were 29 experiments when both units were acquiring data, two experiments with only low frequency sonar data and three experiments with only data from the high frequency sonar. A summary of the experimental results is presented in Table 2.3.

2.5.1 Frazil Production and Concentrations

During each experiment, frazil particles started to appear in the tank shortly after the water became supercooled. In Fig. 2.4 the measured concentrations C (%) and the corresponding supercooling temperatures T_{sp} (°C) are plotted as a function of the supercooling duration, t_{sp} (min). The supercooling duration is the time from when the water first became supercooled until the moment the sonar data sampling stopped and sieve concentration measurements started. For the frazil experiments, t_{sp} varied from 4 to 21 min. The supercooling water temperature T_{sp} (°C) defined as the final water temperature for each experiment, varied from -0.04

to -0.16 °C. The observed cooling rates, *dT/dt* ranged from 0.006 to 0.012 °C/min with an average value of ~0.01 °C/min. These values are close to the cooling rates of 0.003 to 0.008 °C/min reported by Ye et al. (2004) for frazil experiments in a counter-rotating flume at -10 °C. The data in Fig. 2.4 demonstrates that the cooling rate was approximately constant and that the supercooling temperature was proportional to the supercooling duration. The mass concentration for each experiment was calculated using Eq. (2.21) and was found to range between 0.012 % and 0.135 %. These concentrations are comparable to those observed in previous laboratory studies: e.g., 0.065 to 0.609% (Ettema et al., 2003), and 0.10 to 0.17 % (Ye et al., 2004).

Fig. 2.4 shows that there is no correlation between the supercooling temperature, T_{sp}, and the corresponding suspended frazil ice concentration, C (%), measured at the end of the experiment. This is likely due to variations in the timing and amount of initial seeding particles from one experiment to another.

2.5.2 Frazil Size Measurements

Microscopic images of sieved frazil ice particles were used to determine the size range and shapes of the particles. Particle size measurements were taken during 12 experiments, and 4 to 5 microscope slide samples were imaged in each case. In total, 316 individual frazil ice particles were measured from 70 microscopic images. Fig. 2.5 shows three typical microscopic images of frazil particles samples taken with 10X magnification. The majority of the particles were observed to be circular disks and the average particle diameter was found to be 1.97 mm with a standard deviation of 0.89 mm. The smallest clearly visible particles were 0.25 mm in diameter and the largest particles were approximately 4.25 mm. These sizes are comparable to observations in prior studies; for example: 0.1 to 1.0 mm (Gosink and Osterkamp, 1983), 1 to 6 mm (Beltaos and Dean, 1981), 0.05 to 0.6 mm (Daly and Colbeck, 1986), 1 to 5 mm (Daly, 1994), and 0.04 to 5 mm (Clark and Doering, 2006).

A limitation of these measurements is that the sample sizes were relatively small. At most, five samples could be gathered during an experiment before the particles began to freeze together in the sieve and on the microscope slide. Small sample sizes caused size distributions from individual experiments to vary significantly from one experiment to the next (see Fig. 2.6). For this reason, the individual histograms from the 12 experiments were combined to form a single more statistically significant particle size histogram. This combined particle size histogram is plotted in Fig. 2.7. It is likely bimodal because, even after combining all the data, the sample size is still relatively small. It was believed that this sampling method underestimated the number of small frazil particles for two reasons. First the sieve mesh size of 1.8 mm allows small particles to pass through the sieve, and second, the fact that frazil particles were manually sampled from the sieve and placed under the microscope, limited the minimum particle sizes that were visible and measured. As a result, this technique only provided an approximate range of particle sizes and not a representative size distribution.

2.5.3 Sonar Results

A MATLAB [Mathworks Inc.] code was developed to process the sonar pre-processed counts, N, using Eq. (2.13) to calculate the volume backscatter strength, S_v. Fig. 2.8 presents time series of the water temperature T_w (°C) and sonar data from both the high and the low frequency units for a typical frazil experiment, starting at the onset of supercooling and continuing until the experiment was stopped. S_v is a function of range, R and time, t and its magnitude is indicated by a color scale. The T_w (°C) time series in Fig. 2.8 (a) exhibits the typical supercooling rate dT/dt of 0.01 °C/min during this experiment. Fig. 2.9 presents time averaged profiles of S_v of the background signal (when no frazil was present) and at the end of the experiment (frazil profiles), averaged over 20 seconds (20 profiles) for both sonar units. Profiles presented in Fig. 2.9 and the 2-D time series plots of S_v presented in Fig. 2.8 (b & d) show that the backscatter signal amplitudes did not vary significantly with range above the minimum lookout distance and below the water surface. This indicates that frazil particles were

uniformly distributed throughout the water column. Therefore, the sonar signal was depth averaged from a range of 0.5 to 1.0 m above the transducer. Averaging over this depth range ensures that reverberations from the water surface are not included in the averaging and that all the data is above the minimum lookout distance. Time series of the depth averaged volume backscatter strength S_{vd} (dB) are plotted in Fig. 2.8 (c & e). A low pass filter with a cutoff frequency of 0.033 Hz was applied to the time series data of S_{vd} (dB). The values of the filtered S_{vd} (dB) time series at the end of an experiment were taken as the representative values for that experiment. Fig. 2.8 (f) is a time series plot of the ratio of the (high to low) volume backscatter coefficients. At the start of the experiment (i.e. t = 0 min) the ratio was approximately 3 and it did not increase significantly until t ~ 8 min when frazil ice first appeared in the tank. As the frazil ice concentration increased, the ratio increased, reaching a value of ~90 by the end of this experiment.

As is evident in Fig. 2.8, the high frequency unit was found to be more sensitive than the low frequency unit to the presence of small frazil concentrations in the tank and, as a result, S_v and S_{vd} increased earlier in Fig. 2.8 (b & c) compared to Fig. 2.8 (d & e). The low frequency sonar was less sensitive to the presence of frazil particles due to its lower signal to noise ratio. When a relatively high concentration of 0.12 % was reached, the low frequency signal was ~15 dB above the background noise level, compared to the high frequency unit which was ~35 dB above the noise floor as shown in Fig. 2.9 (a & b). The profiles plotted in Fig. 2.9 also show that for this experiment, S_v values for the high frequency sonar were ~20 dB higher in magnitude compared to the low frequency sonar.

For measured concentrations, C, ranging from 0.012 to 0.135 %, the corresponding S_{vd} values varied from -60 to -45 dB and from -49 to -26 dB for the low and high frequency sonars, respectively (see Table 2.3). Following the approach proposed by Thevenot et al. (1992) (see section 2.2.4); the relative backscatter, RB was calculated from the representative S_{vd} value for each of the frazil experiments using Eq. (2.17). A linear least squares regression algorithm

was used to fit Eq. (2.19) to the measured concentrations, C and corresponding RB values. The resulting regression equations for the high and low frequency sonars, respectively, are

$$C = 10^{(-8.015+0.048*RB)} \tag{2.22}$$

and

$$C = 10^{(-9.363+0.066*RB)} \tag{2.23}$$

Values of the intercept and slope in Eqs. (2.22) and (2.23) are of the same order of magnitude as values reported in the sediment transport literature (e.g. Thevenot et al., 1992 and Gartner, 2004). These regression equations and their 95% confidence limits are plotted in Fig. 2.10 and 2.11, together with the measured values of C and the corresponding RB and S_{vd} for the low and the high frequency sonars, respectively. The coefficients of determination, R^2, were 0.96 and 0.93 for Eqs. (2.22) and (2.23), respectively. The low frequency data had a lower coefficient of determination likely due to its lower signal to noise ratio. The 95% confidence limits for predicting C from RB using Eqs. (2.22) and (2.23), varied from ±0.005% to ±0.025% and from ±0.007% to ±0.033%, for the high and the low frequency sonars, respectively.

The background noise levels (i.e. S_{vd} values when no frazil ice is present in the tank) were found to be -58 dB and -62 dB for the high and low frequency sonars, respectively (see Fig. 2.9). These noise levels correspond to relative backscatter values of 116 dB and 113 dB, respectively. Using these background values, Eqs. (2.22) and (2.23) predict minimum detectable concentrations of 0.0034% and 0.017% for the high and low frequency sonars, respectively. Frazil ice concentrations below these limits will not be detectable.

At concentrations higher than 0.15 %, the high frequency sonar raw counts were sometimes saturated (i.e. N = 65335), although the unit was operated at the lowest

gain of one. The effect of this data saturation is that the high frequency can only be used to measure frazil concentrations less than ~0.15 %. Note that these high signal levels at concentrations greater than 0.15% may be in part caused by floc formation. Data saturation was not a problem with the low frequency sonar even when flocculation occurred in the frazil tank.

In addition to the practical limitations mentioned above, it should be noted that single frequency sonars cannot differentiate between changes in ice concentration and particle size distribution (Gartner, 2004). Thus, a change in the size distribution could be misinterpreted as a change in concentration. As a result, Eqs. (2.22) and (2.23) are applicable only for the frazil particle sizes and shapes for which the instruments were calibrated. That is, if the particle size distribution or shapes are significantly different, additional calibration experiments might need to be conducted and new regression equations derived. In this study, the assumption that the backscatter signal was primarily a function of the frazil concentration was tested. The validity of this assumption is the subject of future experiments.

A number of theoretical acoustic backscatter models have been developed relating the backscatter cross section σ_{bs} of an individual particle, to its size, shape, material properties and the acoustic wavelength (Bowman et al., 1969). The most widely used models were developed for single spherical particles (e.g. Rayleigh, 1896; Anderson, 1950; and Johnson, 1977). These models have been used to predict size distributions and concentration of suspended sediments and marine organisms in estuaries and oceans using acoustic devices (e.g. Kristensen and Dalen, 1986; Gartner, 2004). Richard et al. (2010) and Marko and Jasek (2010a, b & c) predicted frazil ice properties (concentration and particle size) from sonar data using the models of Johnson (1977) and Rayleigh (1896), respectively. Both assumed that the scattering targets were uniform in size and that the concentration of particles is relatively low so that the scattering fields of individual particles did not interfere. The assumption of a uniform particle size means that the volume backscatter coefficient, s_v, is proportional to the backscatter cross section, σ_{bs}, of an individual particle (see Eq. 2.16). Therefore, the ratio of the volume

backscatter coefficients is equal to the ratio of the backscatter cross sections at the two frequencies (i.e. $s_{v1}/s_{v2} = \sigma_{bs1}/\sigma_{bs2}$ where indices 1 and 2 denote the high and low frequencies, respectively). Measurements of the ratio s_{v1}/s_{v2} can then be used to provide estimates of the particle radius, a, using theoretical predictions of $\sigma_{bs1}/\sigma_{bs2}$. The plot of $\sigma_{bs1}/\sigma_{bs2}$ shown in Fig. 2.12, predicted using Johnson's (1977) model, can be used to estimate frazil ice particle sizes (Richard et al., 2010). In Fig. 2.12 at small radii (Rayleigh scattering; $ka << 1$, where k is the wave number) $\sigma_{bs1}/\sigma_{bs2}$ is proportional to $(k_1 / k_2)^4$ and as a result the curve approaches an asymptotic limit of 29.1. At large radii (geometric scattering; $ka > 1$) it reaches an asymptotic limit of 1.0.

For this approach to be applicable the ratio must be between the two asymptotic limits (i.e. $1.0 \leq s_{v1} / s_{v2} \leq 29$. The typical time series of s_{v1} / s_{v2} plotted in Fig. 2.8(f) shows the general trend observed in all of the experiments, and in all but a few cases (only 4 experiments) s_{v1} / s_{v2} exceeded the asymptotic limit of 29.1 by the end of the experiment. In Fig. 2.13 the ratio of s_{v1} / s_{v2} calculated using Eqs. (2.22) and (2.23) is plotted versus frazil concentration C (%). This plot shows that s_{v1} / s_{v2} increased with frazil concentration which is consistent with the general trend observed in the time series data of the ratio s_{v1} / s_{v2} in all experiments. According to Fig. 2.13, the ratio is less than 29.1 for frazil concentrations below 0.025 %. Therefore, prediction of particle diameters using this technique may only be applicable at concentrations below this limit.

2.6 Summary and Conclusions

High and low frequency sonars were used to insonify suspended frazil ice particles in a custom built water tank located in the University of Alberta cold room facility. Direct measurements of frazil ice mass concentrations were conducted using a sieving technique. The measured concentrations ranged from 0.012 % to 0.135 %. Sieved frazil ice particles were examined under a microscope to determine the average shape and size of the particles. The majority of the

observed frazil ice particles were disk shaped and ranged from 0.25 to 4.25 mm in diameter.

A significant correlation was observed between the sonar signals and the frazil concentration measurements. A linear least square regression analysis was used to fit equations proposed by Thevenot et al. (1992) to relate the relative backscatter to the frazil concentration. The resulting coefficients of determination, R^2, were 0.96 and 0.93 for the high and low frequency data, respectively. The maximum concentration that can be measured before saturating the high frequency sonar signal was found to be ~0.15 %. The low frequency sonar signal was never saturated even when frazil flocs were present in the tank. The regression equations predict that the minimum concentrations that can be measured using the high and the low frequency sonars is 0.0034 % and 0.017 %, respectively, due to the background noise level. The data used to produce the empirical regression equations was obtained in a laboratory frazil ice tank under idealized controlled conditions. Therefore, their validity and accuracy when applied to field data is currently unknown and is the subject of ongoing research. The ratio of the volume backscatter coefficient was found to increase with frazil concentration and exceeds the asymptotic limit for $ka \ll 1$ at concentrations greater than 0.025%. This implies that the approach used by Richard et al. (2010) and Marko and Jasek (2010c) to predict frazil ice properties may only be valid at low concentrations.

Tables

Table 2.1. Instrument specifications for the high and low frequency sonar units.

Parameter	**Low freq**	**High freq**
Frequency, *f* (kHz)	235	546
Transducer diameter (mm)	36	25.4
-3dB beamwidth, ψ (degrees, steradian Sr)	(11, 0.02893)	(6, 0.00861)
Transmitting Voltage Response, *TVR* (dB re 1μPa @ 1m)	165	176
Open Current Voltage, *OCV* (dB re 1V per 1μPa)	-187.5	-192
Insertion Loss, *IL* (*TVR* +*OCV*) (dB)	-22.5	-16
Source Level, *SL* (dB re 1μPa @ 1m) for 15 V supply	202	213
Wave Length, λ (mm) for sound speed of 1403 m/s	5.97	2.57
Maximum Range (m)	20	20
Minimum Lookout[a] (m)	0.5	0.4
Gain Setting	Variable (1 to 4)	

[a] The minimum lookout, is the minimum distance above the transducer below which targets cannot be detected

Table 2.2. SWIPS parameters used for the frazil ice experiments

Parameter	**Low freq**	**High freq**
Pulse length (μs)	68	17
Gain level	4	1
Ping frequency (Hz)	1	1
Sensor sampling frequency (Hz)	1	1
Sound speed (m/s)	1403	1403
Input voltage (V_{supply})	15	15

Table 2.3. Summary of frazil experiments results showing the Experiment number, the mass of sieved ice M_{ice} (g), the Coefficient of Variation, *COV*, between the three sieved samples, the calculated concentration, *C* (%), the measured supercooling, T_{sp} (°C), the rate of supercooling *dT/dt* (°C/min), and the measured depth average volume backscatter strength S_{vd} (dB) at the end of the experiment.

Exp#	M_{ice} (g) Average	$COV = \sigma/\mu$	*C*%	T_{sp} (°C)	t_{sp} (min)	*dT/dt* (°C/min)	S_{vd} (dB)	
							Low Freq	High Freq
20	17.47	0.06	0.044	-0.09	9	0.01	-53.91	-36.09
25	23.8	0.2	0.07	-0.11	10.83	0.01	-50.72	-32.59
28	21.23	0.08	0.06	-0.05	7.67	0.007	-51.89	-33.01
29	31.67	0.2	0.104	-0.07	6.83	0.01	-48.23	-29.47
30	22	0.16	0.063	-	-	-	-50.36	-
32	25.9	0.2	0.079	-0.05	5.73	0.009	-51.98	-33.02
33	18.17	0.11	0.046	-0.04	4.33	0.01	-52.00	-34.69
36	23.07	0.12	0.067	-0.11	10.83	0.01	-48.11	-34.11
41	11.33	0.18	0.018	-0.15	14.37	0.01	-58.20	-41.11
42	11.67	0.18	0.019	-0.12	11.55	0.01	-59.78	-42.76
43	12.33	0.19	0.022	-0.13	11.48	0.011	-56.97	-44.04
44	10	0.1	0.012	-0.13	12.72	0.01	-	-47.55
45	10.67	0.2	0.015	-0.12	10.57	0.011	-55.33	-49.12
46	12.01	0	0.02	-0.13	11.92	0.011	-55.73	-45.24
47	11.67	0.13	0.019	-0.15	13.92	0.011	-58.95	-43.96
48	12.67	0.12	0.023	-0.15	12.5	0.012	-58.24	-41.13
49	18.33	0.18	0.047	-0.16	15.83	0.01	-51.83	-33.24
50	19.33	0.06	0.051	-0.16	16.5	0.01	-53.19	-32.28
51	33.67	0.14	0.112	-0.13	12.28	0.011	-48.74	-29.09
52	23.67	0.05	0.07	-0.13	12.72	0.01	-51.67	-32.84
53	35.67	0.18	0.121	-0.11	12.97	0.008	-47.09	-27.99
54	21.33	0.18	0.06	-0.12	12.37	0.01	-52.17	-32.28
55	36.33	0.11	0.124	-0.13	13.62	0.01	-44.52	-26.63
56	32.33	0.07	0.107	-0.12	12.65	0.01	-48.86	-29.26

57	29.67	0.1	0.095	-0.13	12.65	0.01	-50.84	-31.79
58	29.33	0.1	0.094	-0.13	10.5	0.012	-	-29.25
59	34	0.16	0.114	-0.13	14.58	0.009	-47.64	-28.37
60	26	0.2	0.08	-0.14	15.28	0.009	-48.04	-29.83
61	13.67	0.08	0.027	-0.12	12.77	0.009	-56.36	-36.99
72	12	0.14	0.02	-0.09	9.43	0.009	-	-38.84
76	28.33	0.09	0.09	-0.13	20	0.007	-49.58	-28.36
79	30.33	0.14	0.098	-0.12	21	0.006	-49.27	-28.10
80	39	0.16	0.135	-0.15	13.92	0.011	-45.59	-28.57
96	12.83	0.02	0.024	-	-	-	-59.67	-

Figures

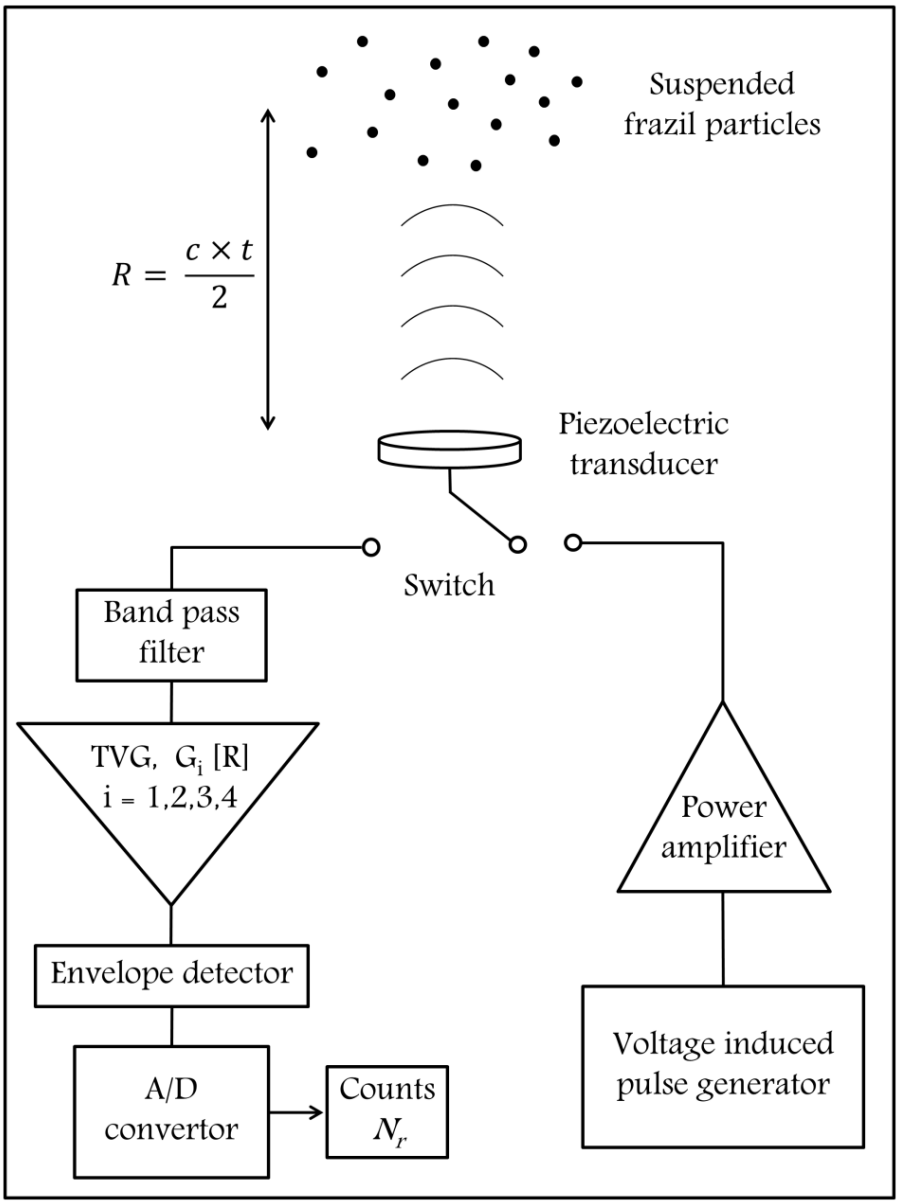

Fig. 2.1. Simplified schematic diagram showing the signal path through the SWIPS electronic (adapted from Lemon *et al.* 2008).

Fig. 2.2. (a) Front view of the frazil ice tank. (b) top view of the frazil ice tank setup showing the high and low frequency sonar units, the Plexiglas base plate, and cables inside the hollow PVC tubes; two of the side mounted propellers and the four bottom mounted propellers are also shown.

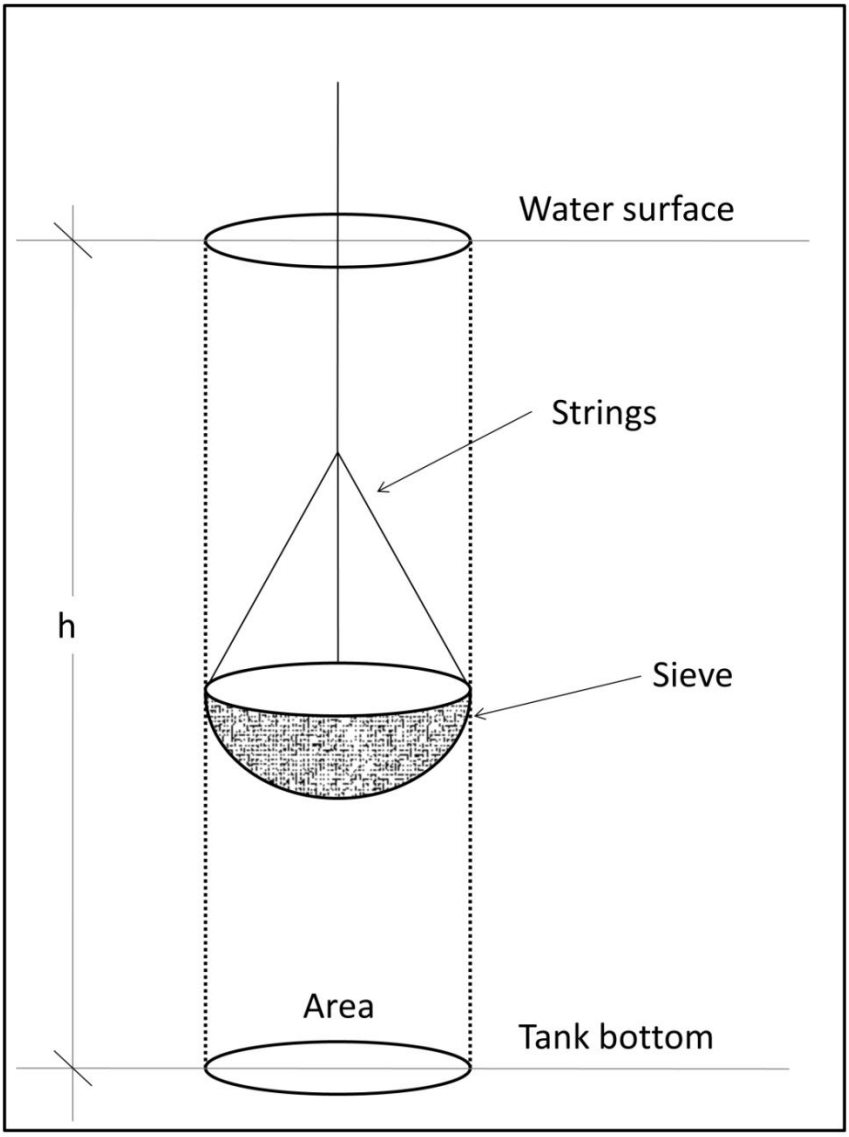

Fig. 2.3. A schematic diagram showing the sieving technique used for frazil ice concentration measurements.

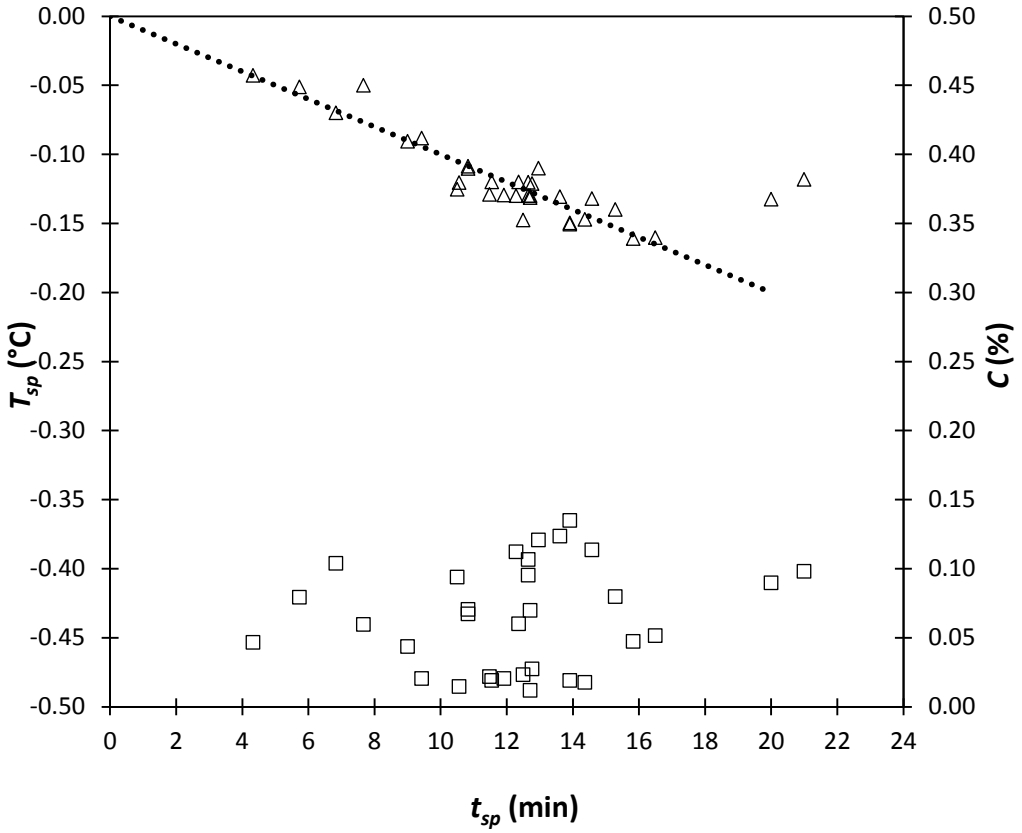

Fig. 2.4. Plot showing (Δ) the measured supercooling water temperatures T_{sp} (ºC) and (□) the corresponding sieve concentrations C (%) versus the duration of supercooling t_{sp} (min). The dotted line represents the average observed supercooling rate dT/dt of 0.01 (ºC/min).

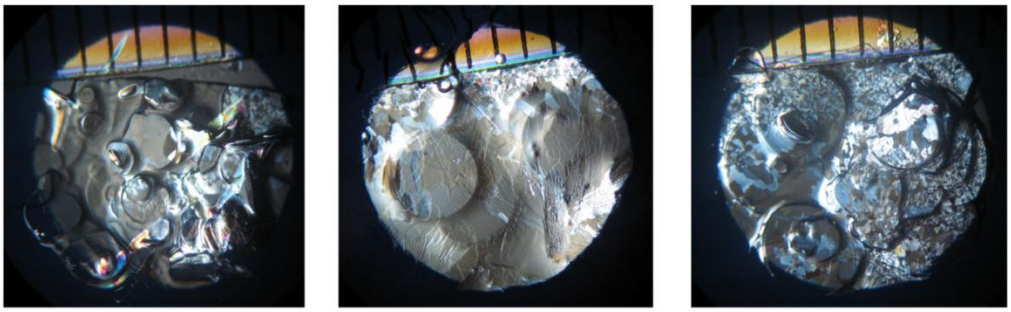

Fig. 2.5. Images of frazil particles under the microscope (scale on the top is in mm)

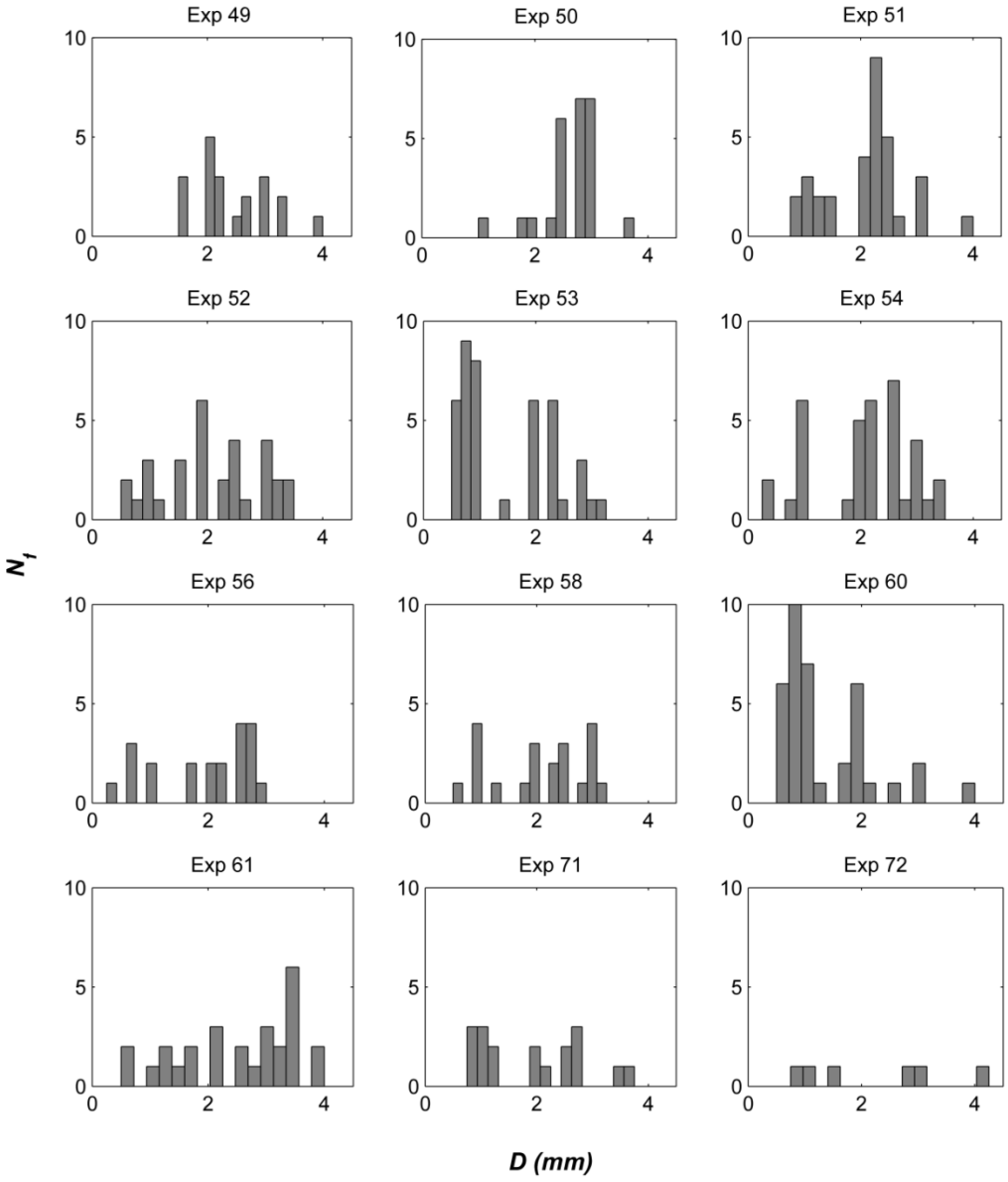

Fig. 2.6. Histograms of the number of frazil particles N_f versus particle diameter D (mm) for 12 frazil experiments.

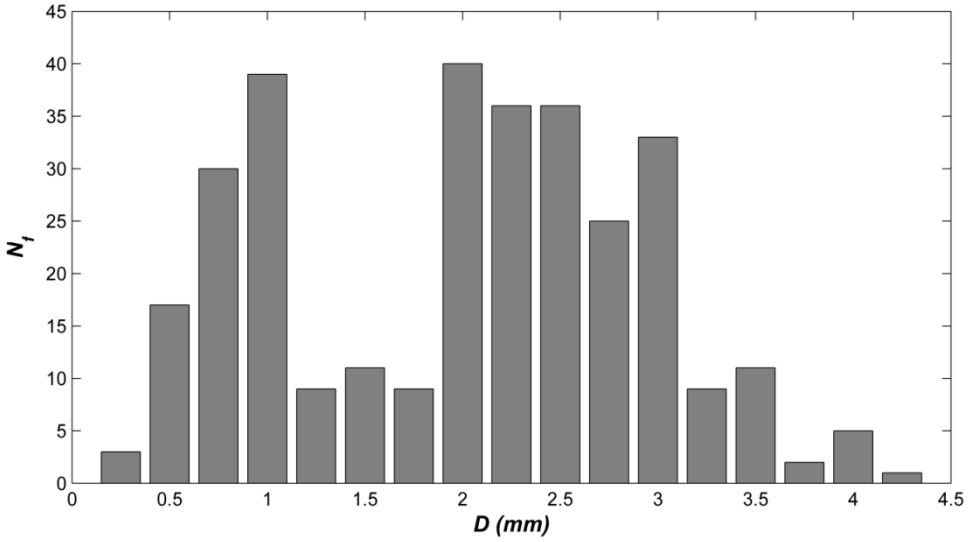

Fig. 2.7. Combined histogram from 12 frazil experiments showing the number of frazil particles N_f versus frazil ice particle diameter D (mm).

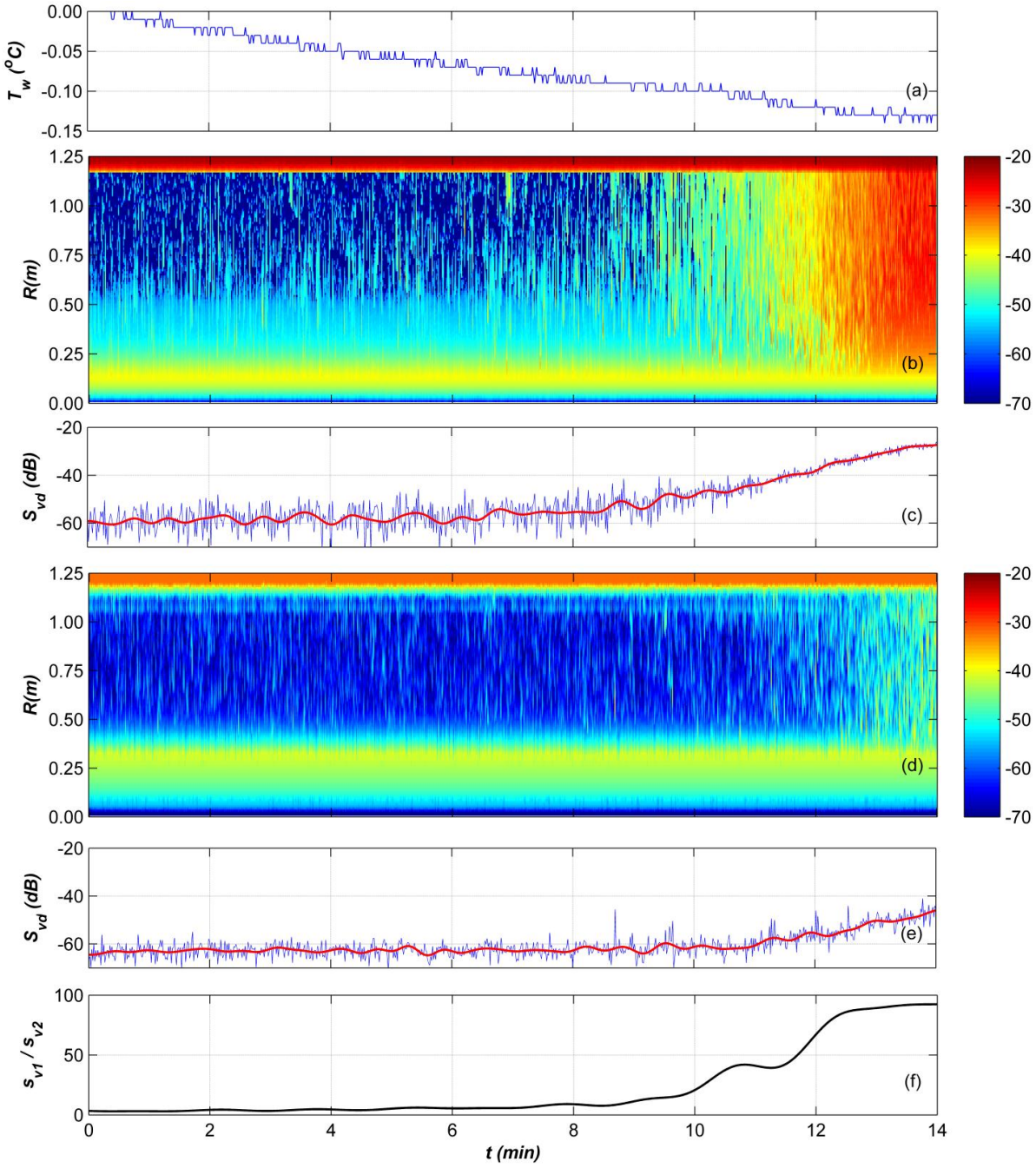

Fig. 2.8. Time series data from Exp 55 (C = 0.12 %): (a) water temperature T_w (ºC), (b) and (d) 2-D plot of S_v (dB color coded) data, range R (m) versus time t (min), (c) and (e) depth averaged volume backscattered strength S_{vd} (dB); for the high and low frequency sonars, respectively, (f) the ratio of the high to the low frequency backscatter coefficient (s_{v1}/s_{v2}). The blue thin line and the thick red line and in (c) and (e) are the instantaneous and the low pass filtered time series data, respectively.

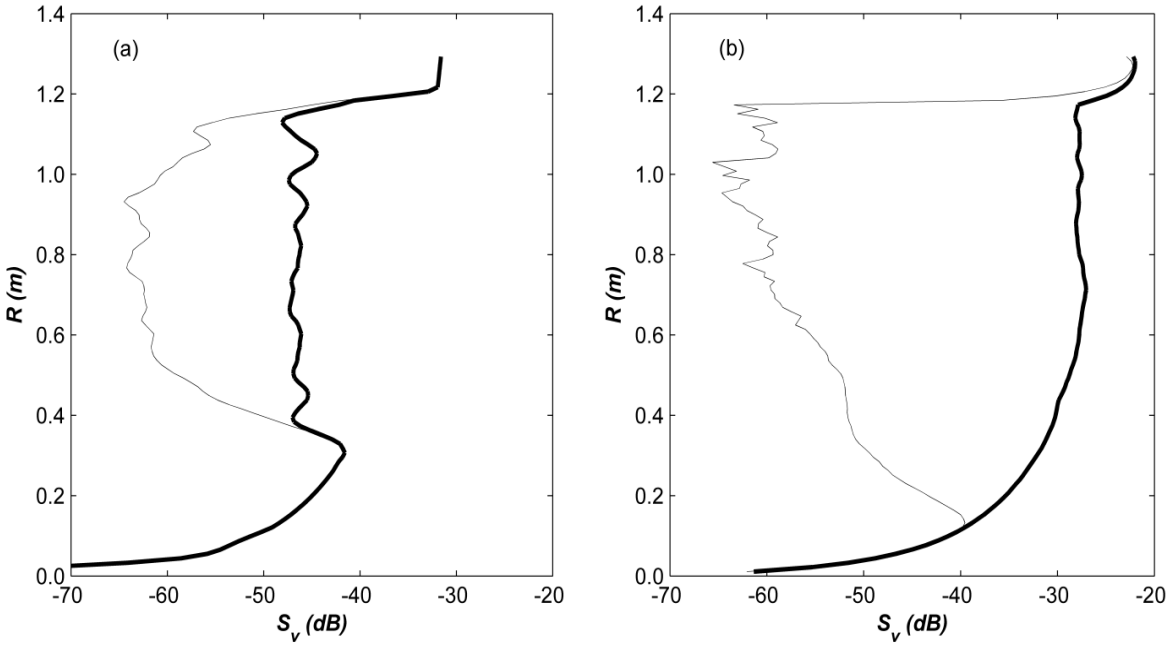

Fig. 2.9. Range, R (m) versus volume backscatter strength, S_v (dB) from Exp 55 (C = 0.12 %) averaged over 20 seconds of the experiment showing the background signal (thin line) and returns due to frazil ice (thick line) for (a) the low and (b) the high frequency sonars.

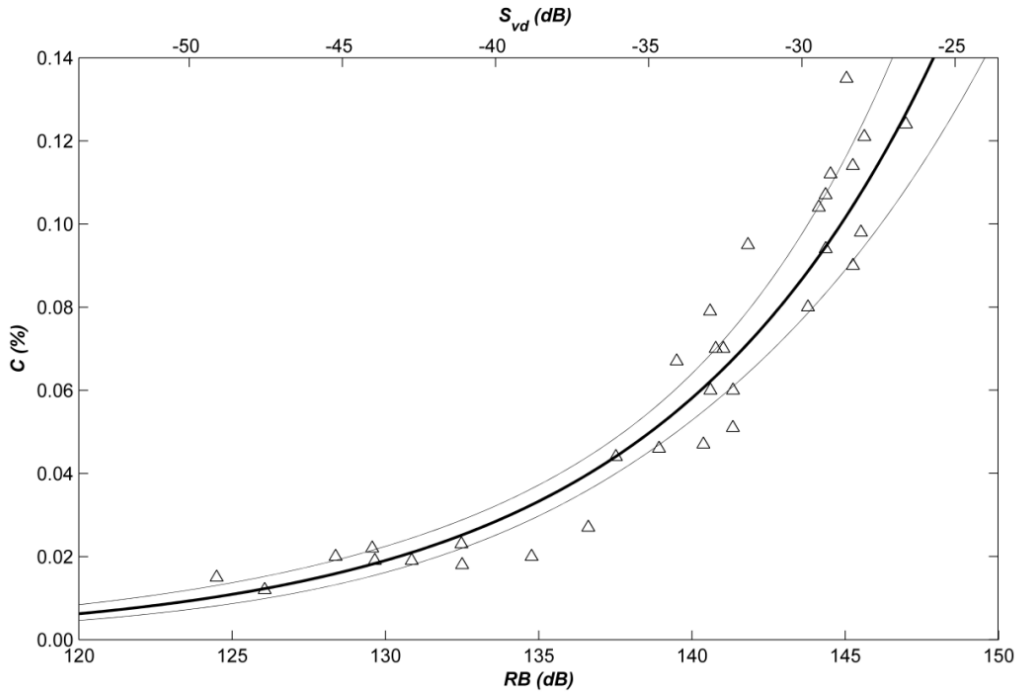

Fig. 2.10. Concentration *C* (%) versus the relative backscatter *RB* (dB – lower axis) and depth averaged volume backscatter strength S_{vd} (dB – upper axis). High frequency sonar experimental data points (Δ), regression Eq. (2.22) (thick line) and the 95% confidence limits of Eq.(2.22) (thin line).

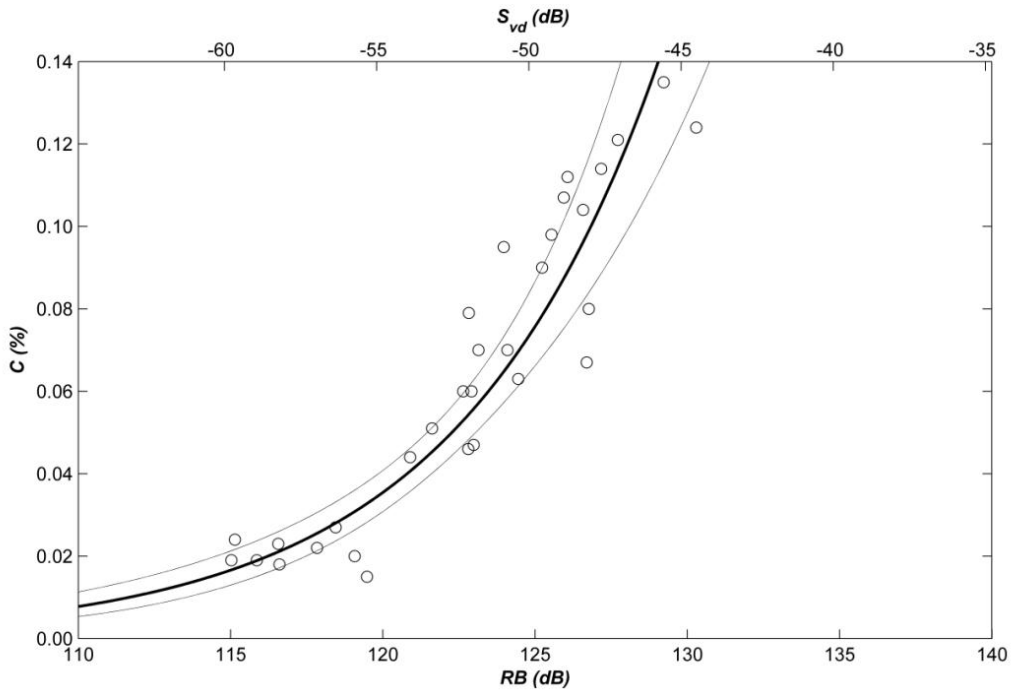

Fig. 2.11. Concentration C (%) versus the relative backscatter RB (dB – lower axis) and depth averaged volume backscatter strength S_{vd} (dB – upper axis). Low frequency sonar experimental data points (○), regression Eq. (2.23) (thick line) and the 95% confidence limits of Eq. (2.23) (thin line).

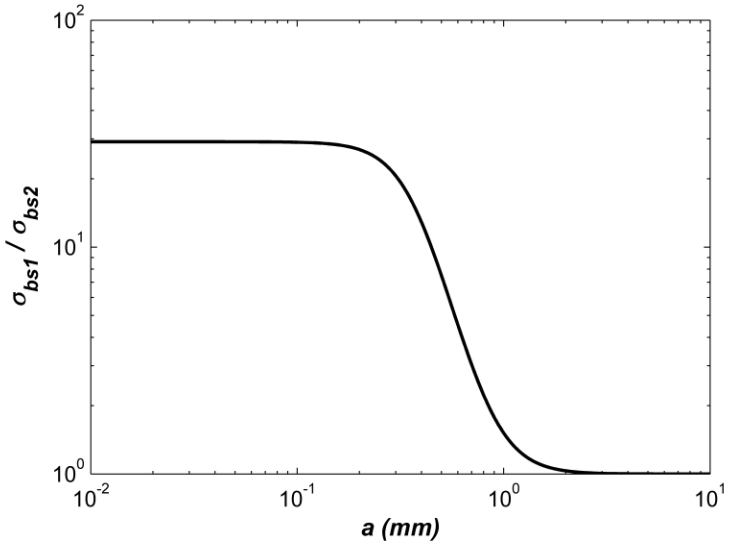

Fig. 2.12. The ratio of the high to the low frequency backscatter cross section (σ_{bs1} /σ_{bs2}) versus particle radius *a* (mm) computed using Johnson's (1977) model.

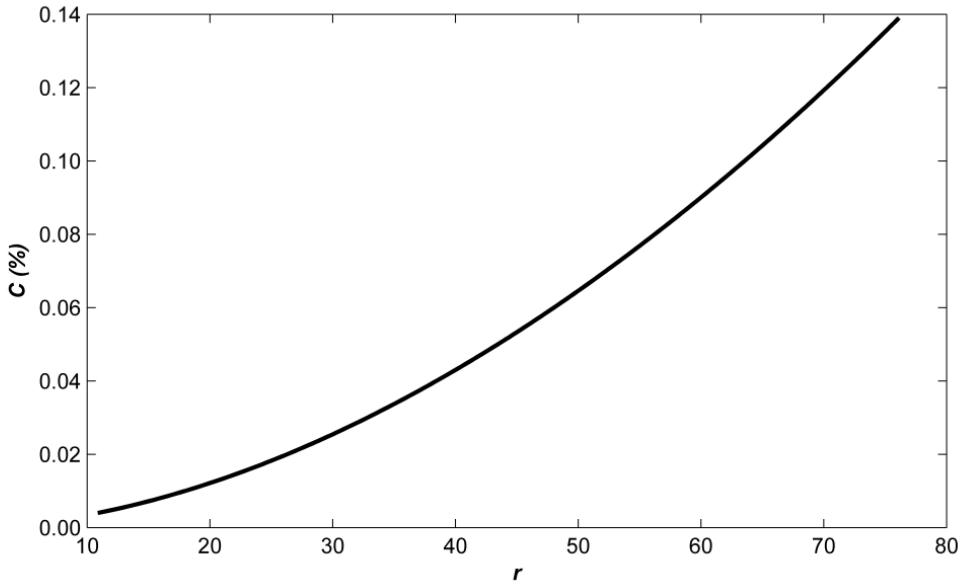

Fig. 2.13. Frazil concentration C (%), versus the ratio r of the high to the low backscatter coefficients (s_{v1} / s_{v2}) calculated using Eqs. (2.22) and (2.23), respectively.

References

Ainslie, M.A., McColm, J.G., 1998. A Simplified Formula for Viscous and Chemical Absorption in Sea Water. Journal of the Acoustical Society of America, 103(3), 1671-1672.

Anderson, V. C., 1950. Sound Scattering from a Fluid Sphere, J. Acoust. Soc. Am. 22, 426–431.

Beltaos, S., Dean, A.M., 1981. Field Investigations of a Hanging Ice Dam. Proceedings of the 6th IAHR Symposium, 1981, Quebec, Canada, 475-488.

Bowman, J. J., Senior, T. B. A. and Uslenghi, P. L. E., Eds., 1969. Electromagnetic and Acoustic Scattering by Simple Shapes. Amsterdam: North-Holland. 728pp.

Buermans, J., Fissel, D., Marko, J., Jasek, M., 2010. Progress in Shallow Water Ice Profiling Sonar (SWIPS) for River and Lake Ice Monitoring. Proceedings of 20th International Symposium on Ice, Lahti, Finland.14 p.

Clark, S., Doering, J.C., 2006. Laboratory Experiments on Frazil-Size Characteristics in a Counter Rotating Flume. Journal of Hydraulic Engineering, 132(1), 94-101.

Clay, C.S., Medwin, H., 1977. Acoustical Oceanography. Wiley-Interscience, New York. 544 pp.

Daly, S.F., Colbeck, S., 1986. Frazil Ice Measurements in CRREL's Flume Facility. Proc. Syrup. Ice 1986. Int. Assoc. Hydraul. Res., Iowa City, Iowa, pp. 427--438.

Daly, S.F., 1994. International Association for Hydraulic Research Working Group on Thermal Regimes: Report on Frazil Ice. U.S. Army Corps of Engineers Special Report 94-23. 43p.

Doering, J.C., Morris, M.P., 2003. A Digital Image Processing System to Characterize Frazil Ice. Canadian Journal of Civil Engineering, 30: 1–10.

Ettema, R., Karim, M.F., Kennedy, J.F., 1984. Laboratory Experiments on Frazil Ice Growth in Supercooled Water. Cold Regions Science and Technology, 10: 43-58.

Ettema, R., Chen, Z., and Doering, J., 2003. Making Frazil Ice in a Large Ice Tank. Proceedings of the 12th Workshop on the Hydraulics of Ice Covered Rivers, Committee on River Ice Processes and the Environment, Edmonton, Canada, 13 pp.

Gartner, J.W., 2002. Estimation of Suspended Solids Concentrations Based on Acoustic Backscatter Intensity: Theoretical Background. Turbidity and other sediment surrogates workshop.

Gartner, J.W., 2004. Estimating Suspended Solids Concentrations from Backscatter Intensity Measured by Acoustic Doppler Current Profiler in San Francisco Bay, California. Marine Geology 211, no. 3-4: 169-187.

Ghobrial, T.R., Loewen, M.R., Hicks, F., 2009. Frazil Ice Measurements Using the Shallow Water Ice Profiling Sonar. Proceedings of 15th Workshop on River Ice, St. John's, Newfoundland and Labrador, June 15 - 17, 2009, pp. 14-26.

Gosink, J.P., Osterkamp, T.E., 1983. Measurements and Analysis of Velocity Profiles and Frazil Ice Crystal Rise Velocities during Periods of Frazil-Ice Formation in Rivers. Annals of Glaciology 4, 79–84.

Jasek, M., Marko, J.R., Fissel, D., Clarke, M., Buermans, J., Paslawski, K., 2005. Instrument for Detecting Freeze-up, Mid-Winter and Break-up Processes in Rivers. Proceedings of 13th Workshop on Hydraulic of Ice-Covered Rivers, Hanover, NH. 34p.

Johnson, R. K., 1977. Sound scattering from a fluid sphere revisited, J. Acoust. Soc. Am., 6 (2), 375-377. (Erratum: Sound scattering from a fluid sphere revisited, J. Acoustic. Soc. Am., 63(2), 626, 1978.)

Kristensen A., Dalen J., 1986. Acoustic Estimation of Size Distribution and Abundance of Zooplankton, J. Acoust. Soc. Am., 80, 601‑611.

Leighton, T. G., 1994. The Acoustic Bubble. Academic Press, London, 613 pp.

Lemon, D.D., Billenness, D., Buermans, J., 2008. Comparison of Acoustic Measurements of Zooplankton Populations Using an Acoustic Water Column Profiler and an ADCP. OCEANS-IEEE Conference, SEP 15-18, Quebec, Canada, Vol. 1-4, Pages: 1404-1411.

Lever, J., Daly, S., Rand, J., Furey, D., 1992. A Frazil Ice Concentration Meter. Proceedings of the 11th IAHR Symposium, Banff, Canada, 1362-1376 .

Marko, J.R., Fissel, D.B., Jasek M., 2006. Recent Developments in Ice and Water Column Profiling Technology. Proceedings of the 18th IAHR International Symposium on Ice, Sapporo, Japan, 8pp.

Marko, J.R., Jasek, M., 2010a. Sonar Detection and Measurements of Ice in a Freezing River I: Methods and Data Characteristics. Cold Regions Science and Technology. 63, 121–134.

Marko, J.R., Jasek, M., 2010b. Sonar Detection and Measurement of Ice in a Freezing River II: Observations and Results on Frazil Ice. Cold Regions Science and Technology. 63, 135–153.

Marko, J.R., Jasek, M., 2010c. Frazil Monitoring by Multi-frequency Shallow Water Ice Profiling Sonar (SWIPS): Present Status. Proceedings of the 20th IAHR International Symposium on Ice, Lahti, Finland, June 14 to 18, 2010.

Morse, B., Richard, M., 2009. A Field Study of Suspended Frazil Ice Particles. Cold Regions Science and Technology, Volume: 55, pp 86–102.

Rayleigh, J., 1896. The Theory of Sound, Vol. 2 (Dover, New York, 1945).

Reichel, G., Nachtnebel, H.P., 1994. Suspended Sediment Monitoring in a Fluvial Environment: Advantages and Limitations Applying an Acoustic Doppler Current Profiler. J. Water Research 28 (4), 751–761.

Richard, M., Morse, B., 2008. Multiple frazil ice blockages at a water intake in the St. Lawrence River. Cold Regions Science and Technology, DOI: 10.1016/j.coldregions.2007.10.003.

Richard, M., Morse, B., Daly, S.F. and J. Emond, 2010. Quantifying suspended frazil ice using multi-frequency underwater acoustic devices. River Research and Applications, DOI: 10.1002/rra.1446.

Safari, A., Koray, E.A., 2008. Piezoelectric and Acoustic Materials for Transducer Applications, in: Tressler, J.F. (Eds.), Piezoelectric Transducer Designs for Sonar Applications. Springer, Berlin, pp. 217–239.

Schmidt, C.C., Glover, J.R., 1975. A Frazil Ice Concentration Measuring System Using a Laser Doppler Velocimeter. J. Hydraulic Research, 13(3): 299-314.

Thevenot, M.M., Kraus, N.C., 1993. Comparison of Acoustical and Optical Measurements of Suspended Material in the Chesapeake Estuary. J. Marine Environmental Engineering, 1: 65– 79.

Thevenot, M.M., Prickett, T.L., Kraus, N.C., 1992. Tylers Beach,Virginia, Dredged Material Plume Monitoring Project 27 September to 4 October 1991. Dredging Research Program Technical Report DRP-92-7, US Army Corps of Engineers, Washington, DC, 204 pp.

Thorne, P.D., Vincent, C.E., Harcastle, P.J., Rehman, S., Pearson, N., 1991. Measuring Suspended Sediment Concentrations Using Acoustic Backscatter Devices. Marine Geology, 98:7-16.

Tsang, G., 1985. An Instrument for Measuring Frazil Concentration. Cold Regions Science and Technology, Volume: 10, Issue: 3, Pages: 235-249

Urick, R.J., 1983. Principles of Underwater Sound. 3rd Edition. McGraw-Hill, Inc., 423 pp.

Yankielun, N., Gagnon, J., 1999. Laboratory Tests of a Time-Domain Reflectometry System for Frazil Ice Detection. Canadian Journal of Civil Engineering, 26: 168–176.

Ye, S.Q., Doering, J.C., Shen, H.T., 2004. A Laboratory Study of Frazil Evolution in a Counter Rotating Flume. Canadian Journal of Civil Engineering, 31(6), 899-914.

CHAPTER 3: Monitoring of River Surface Ice Using Sonars

3.1 Introduction

The freeze-up season in a river begins after the air temperature drops below 0°C, when the water becomes supercooled (i.e. cooled to slightly below 0°C) and frazil ice particles begin to form in the turbulent flow. When present in supercooled water, frazil particles are very adhesive (termed 'active' frazil) and flocculate to form frazil slush. Eventually these frazil flocs reach a sufficient size for buoyant effects to overcome the entraining effects of fluid turbulence and they float to the surface (Martin, 1981). As ice is less dense than water, a portion of the floating frazil slush is exposed above the water and soon freezes, creating 'pancake ice' (also known as 'pan ice' or 'frazil pans'), as illustrated in Fig. 3.1a. The edges of these pans become upturned due to collisions, as surface ice concentrations increase. It is common for the pans to tilt and take on water during these collisions causing them to thicken in the upward direction as this surface water freezes. Pans also thicken downward as further heat loss causes freezing of the pore water in the slush underlying the surface crust. In addition, pans frequently slide on top of one another during collisions, creating floating pan accumulations known as frazil rafts (Fig. 3.1a). When surface concentrations of frazil pans and rafts approach 100%, congestion occurs and 'bridging' becomes likely. Typically bridging can occur anywhere the surface ice discharge capacity is decreased, including at tight river bends, islands, bridges, natural constrictions, or at constrictions created by border ice, as illustrated in Fig. 3.1b.

Once bridging occurs, incoming pans lengthens the accumulation in the upstream direction. This may occur by juxtapositioning (pans configured edge to edge) or by hydraulic thickening caused by entrainment and/or under turning of surface ice (Dow Ambtman et al., 2011). In both cases, the leading edge of the ice accumulation propagates upstream, although the rate will be much higher in the

case of juxtapositioning. Both the downslope component of ice weight and the flow drag on the underside of the ice accumulation increase as the ice accumulation lengthens. If these driving forces exceed the internal strength of the ice accumulation, then the ice cover will collapse and an ice jam will form. After the frazil pans and rafts come to rest, the underlying frazil slush may also stop moving. However, if the mean water velocity and turbulence are strong enough, frazil slush may be dislodged and move along the underside of the stationary surface ice cover or become re-entrained in the flow. At present, little is known or has been observed about frazil transport under ice.

Continuous measurements of freeze-up processes, such as pan formation and ice cover consolidation, are needed both for model validation, and to advance our fundamental understanding of these processes (Shen, 2010). A number of studies have examined ice cover formation and progression (e.g. Michel, 1984; Andres et al., 2005; Beltaos and Andres, 2005) but these have been limited to observations of frazil pans sizes (especially pan/raft lengths) and shapes during freeze-up (e.g.: Calkins and Gooch, 1982; Osterkamp and Gosink, 1982; Osterkamp and Gosink, 1983). Frazil pans/rafts exceeding 2 m in diameter and 1 m in thickness were reported in these studies. Flume experiments and numerical models have been used to investigate different factors controlling pancake ice drafts and diameters in sea ice (e.g.: Shen et al., 2004; Knuth and Shen, 2006) but there have only been a limited number of studies that reported continuous measurements of surface ice concentration and pan drafts (not lengths) in rivers (e.g.: Morse et al., 2003; Richard and Morse, 2008; Jasek et al., 2011).

Recently, an upward looking sonar, the Shallow Water Ice Profiling Sonar (SWIPS) [ASL Environmental Sciences Inc., Canada] has been developed to measure ice draft in rivers. This device is designed to be installed on the river bed and to transmit acoustic pulses up through the water column. The acoustic signals are reflected by targets in the water column and the intensities of these reflected signals are used to differentiate between different targets types. Currently shallow water ice profiling sonars with two different acoustic transmitting frequencies are

available commercially: a low frequency unit (235 kHz) and a high frequency unit (546 kHz).

These sonar instruments have been deployed successfully in the Peace River, Alberta since 2004 and the field tests on the Peace River, reported by Jasek et al. (2005) and Marko and Jasek (2010a and b), have shown that these sonar instruments can detect floating frazil pans as well as suspended frazil particles. Richard and Morse (2008) used the deep water ice profiling sonar (IPS) to monitor surface ice conditions on the St Lawrence River, Quebec. Recent comparison of measured (using the sonar) versus modeled (using the CRISSP model) pan characteristics by Jasek et al. (2011) showed that using calibrated model parameters, the CRISSP model was in very good agreement with sonar measured pan thickness and surface ice concentrations and was able to detect the ice front passing over. A detailed description of the specifications and principle of operation of these ice profiling sonars was reported by Ghobrial et al. (2012).

The primary objective of this study was to develop a technique that uses the sonar data to provide continuous measurements of surface ice properties (i.e. surface ice concentration, pan drafts and pan lengths). To facilitate this, field data were gathered using two upward looking sonars, a current profiler, an environmental monitoring station and time lapse photography to monitor freeze-up processes on the North Saskatchewan River in Edmonton, AB, Canada from 15-Oct-2009 to 13-Jan-2010. The field data were used to estimate surface ice properties and the accuracy of these estimates were then assessed. Results from this freeze-up season are presented and linkages between meteorological (air and water temperatures) and hydraulic factors (water depth and velocity) affecting pan evolution for select events are examined. Preliminary results from this study, reported by Ghobrial et al. (2010), confirmed that the upward looking sonar is an effective instrument for studying frazil pans properties. Several suspended frazil ice events were recorded during this deployment, and the analysis of these events will be the topic of further investigations.

3.2 Site Description

The North Saskatchewan River, Canada, (length ~1300 km; mean discharge of 245 m^3/s) is a glacier-fed, regulated river that flows east from the Canadian Rockies (1,800 m above sea level) across Alberta (720 m above sea level at Edmonton), to central Saskatchewan (Kellerhals et al., 1972). The winter discharge is largely controlled by the outflows from the Bighorn and Brazeau dams in the upper part of the basin (Hicks, 1997). The river is a shallow meandering river of 1 to 3 meters in depth, and 100 to 200 meters in width. Upstream of Edmonton, the river has numerous islands and through Edmonton, the river has an average slope of 0.00035 (Gerard and Andres, 1982), and it is irregularly meandering (see Fig. 3.2) with many point bars and side channel bars.

The instrument deployment location was in northeast Edmonton, AB (Fig. 3.2) at EPCOR's Clover Bar Power Generating Station (53°35'15" N; 113°22'50" W). The river at this location is approximately 120 m wide and has an average depth of about 1.9 m at low flow. A detailed bathymetric survey was conducted to identify a sufficiently deep and level spot on the river bed for placement of the instrument platform. Fig. 3.3 shows a plan view of the study site, the water depths (at mean daily discharge of 130 m^3/s) in the deployment reach, and the locations of the instruments' platform. The thermal regime of the river at this location is influenced by discharges from the city's Gold Bar Waste Water Treatment Plant (*WWTP*) approximately 6 km upstream (Fig. 3.2) and locally from the power plant cooling water outfall located on the east bank ~50 m upstream of the platform location (Fig. 3.3). These warm water discharges caused the local water temperature to fluctuate by several degrees periodically during the freeze-up period. The thermal energy associated with these temperature fluctuations affected the freeze-up regime and the duration for which a complete ice cover was present at the site.

3.3 Instrumentation and Methods

3.3.1 In Stream Instrumentation

Both high (546 kHz) and low (235 kHz) frequency sonars were deployed at the study site during the 2009 freeze-up season. The IPS5Link [ASL Environmental Sciences Inc.] software was used to operate the sonar units and to acquire data using the settings listed in Table 3.1. The instruments were programmed to ping (emit a sound pulse) at a rate of 1 Hz and to sample data with the maximum sampling rate of 64 kHz which corresponds to a cell size of 0.011 m. A pulse length of 68 μs is recommended by the manufacturer for field deployments to ensure that enough energy is emitted in the acoustic pulse to overcome signal losses. However, it was found that a shorter pulse length of 34 μs was necessary for the high frequency unit to avoid signal saturation (Ghobrial et al., 2012). For the beam-width and transducer diameter of each sonar unit (Ghobrial et al., 2012), at a water depth of 2.0 m (average water depth observed at the site during the deployment), the sampling volume was averaged over a cylinder of 44.58 cm and 81.35 cm in diameter (in the horizontal direction) for the high and the low frequency units, respectively; and 1.1 cm in height (i.e. the cell size in the vertical). This implies that spatial variations less than those numbers in both the horizontal and the vertical directions will not be detected.

Both sonars were equipped with auxiliary sensors that measured absolute pressure above the transducer (range 0–206 kPa, accuracy ±0.2 kPa), water temperature (accuracy 0.1 °C, precision 0.01 °C), input voltage and tilt angle in two perpendicular directions (range ±20°, accuracy ±1.0°, precision 0.1°) (ASL Environmental Sciences Inc., 2007). A supplemental laboratory calibration was conducted to verify the accuracy of the temperature sensors of both sonar units (Maxwell, 2012). A high precision SBE 39 temperature sensor (accuracy ±0.002, resolution 0.0001) [Sea-bird Electronics] was used as the reference temperature sensor for the calibration. The calibration covered a range of temperatures from 5.00 °C to -0.09°C and it was found that the high and the low frequency temperature sensors were shifted by +0.084 °C and -0.461°C, respectively

(Maxwell, 2012). Results of this calibration were used to correct the water temperature data from both sonar units. The sonars were programmed to acquire sensor data every 10 seconds because there was not much variability in the sensor data within this time interval. The units were powered using 15V AC/DC converters. A 2 MHz AquaDopp ® (Acoustic Doppler Current Profiler, Nortek As., Norway) was used to measure velocity profiles during the deployment. It was operated using the AquaPro software [Nortek As., Norway], and setup to sample to a maximum range of 3 m with a cell size of 0.1 m, to acquire velocity data every second and to record an average velocity profile every 5 minutes.

The high and the low frequency sonars, the current profiler, as well as an underwater video camera and light (used to visually monitor the instruments), were mounted on a stainless steel platform (Fig. 3.4a) weighing just over 45 kg (100 lbs.). The platform consisted of a 0.9 m by 0.6 m base with a 20 cm high rail installed around the perimeter to prevent damage to the instruments should overturning occur during deployment or removal. The stainless steel was covered with plastic sheeting to prevent adhesion of suspended frazil.

On 15-Oct-09 the instrument platform was towed ~30 m from the east bank using a jet boat and placed on the river bed in ~1.9 m deep water (Fig. 3.3). The deployed platform was tilted 4.7° in the north-south direction and 0.1° in the east-west direction. Communications and power cables, approximately 100 m in length, were bundled together and laid out along the river's bed and bank, leading up to a small heated trailer on the top of the bank (Fig. 3.3) containing three rugged laptop computers. Each laptop was connected to one of the three acoustic instruments (i.e. the high and the low frequency sonars and the current profiler) making it possible to view the output data in real time and thus to ensure that the instruments were working properly for the entire duration of the deployment.

3.3.2 Supplemental Instrumentation

A monitoring station was installed on the river bank on 15-Oct-09 to collect air and water temperature data and photographs of surface ice conditions at the study site using a remotely accessible camera [Model CC640, Campbell Scientific] (Fig. 3.4b). Air temperature measurements were collected using a temperature sensor [Model 107, Campbell Scientific] mounted ~2 m above the ground. The temperature probe was housed in a radiation shield [Model 31303-5A, Campbell Scientific] to prevent solar radiation from affecting the air temperature measurements. In addition, a submerged water temperature sensor [Model 107B soil and water temperature probe, Campbell Scientific] was placed on the river bed ~10 m from the bank (see Fig. 3.3). The air and water temperature sensors' data were recorded using a data logger [Model CR1000, Campbell Scientific] mounted inside the protective camera enclosure.

Data and images from this monitoring station were sent over a wireless cell phone network to a University of Alberta web server every 30 minutes throughout the deployment period. Digital images from this webcam were used to visually monitor and validate the ice conditions recorded by the sonar instruments. Additional meteorological data (e.g. atmospheric pressure, snow depth, and relative humidity), measured hourly, were downloaded from the Environment Canada website for the Edmonton city center airport weather station (53°34'19" N; 113°31'10" W and station ID # 3012202) located ~10 km west of the deployment site (Fig. 3.2). The observation period ended on 13-Jan-10, when the monitoring station and the instrument platform were removed from the deployment site.

3.4 Data Processing

A MATLAB [Mathworks Inc.] program was written to process and plot all the field data from the monitoring station, the current profiler, and both sonars. The current profiler data was first processed using the SURGE [Nortek AS Inc.]

software to extract time series of the velocity profiles (m/s). The MATLAB code was then used to calculate the depth average (mean) velocity (m/s), and to extract the surface velocity (m/s) for each of these velocity profiles.

The IPS5Extract [ASL Environmental Sciences Inc.] software, was used to extract the auxiliary sensor data as well as profiles of the raw digital sonar data (one profile for each acoustic ping). These raw sonar data consist of digital counts ranging from 0 to 65535 (for the 16-bit digital board) that vary according to the strength of the backscattered signal. In order to estimate the corrected water depth above the transducer, the local atmospheric pressure was subtracted from the absolute pressure measurements as follows,

$$h = \frac{P_{abs} - P_{atm}}{\rho g} - \Delta D \qquad (3.1)$$

where, h is the water depth (m), P_{abs} is the absolute pressure above the transducer (Pa), P_{atm} is the atmospheric pressure (Pa), ρ is the fresh water density (1000 kg/m^3), g is the gravitational acceleration (9.81 m/s), and ΔD is the vertical distance separating the acoustic transducer and the hydrostatic pressure sensor inside the instrument's steel case (Buermans et al., 2010). ΔD was provided by the manufacturer and was equal to 13 cm for both the high and low frequency sonars.

Fig. 3.5 presents a 2 min time interval of raw sonar profiles (color coded) sampled every 1 Hz on a two dimensional plot. In these plots the range R (m) above the sonar transducer is the ordinate and time t (min) is the abscissa. Frazil pans or rafts can be distinguished visually in these plots as the high strength signals that spike downwards from the water surface. It is almost impossible to distinguish from the signal whether those spikes are from an individual pan or from a raft. Therefore, the term "*pan/raft*" will be used in the subsequent text to designate the properties of surface pans and/or rafts.

An algorithm was developed in MATLAB® to automate the calculation of pan/raft drafts and lengths, and surface ice concentrations from the raw sonar data. For the algorithm to identify the presence of a pan/raft in each profile, first the bottom of the pan/raft must be detected. For this purpose, a target detection algorithm was written that applies a *threshold* count (ranging from 0 to 65535) to the raw sonar data and then checks if this threshold is exceeded for a specified number of successive cells (bins) in the vertical direction. The number of bins in which the threshold must be exceeded before a target (i.e. pan bottom) is detected, is referred to as the *persistence* level. The algorithm processes each profile of raw sonar data, starting at a range of 0.5 m from the instrument (i.e. at the minimum lookout distance). When both the threshold and the persistence level criteria are satisfied, the range of the lowest bin in which the threshold was exceeded is identified and recorded as the bottom of a pan/raft. When no pan/raft is present in the water column, the algorithm typically detects the water surface. If the algorithm does not detect a pan/raft or the water surface in a given profile, it linearly interpolates using the target ranges detected in the two adjacent profiles.

Different thresholds, ranging from 45,000 to 65,000 counts, and different persistence levels, ranging from 4 to 8 bins, were tested. It was found that a threshold of 60,000 counts and a persistence of 6 bins were optimum values because this combination produced the least number of false targets for both the high and the low frequency units. That is, these limits were high enough to ensure that returns from suspended frazil and debris were not incorrectly identified as the bottom of pans/rafts, but were not so high that the porous lower edges of slushy pans/rafts went undetected. This technique was tested using two extreme cases for which the maximum errors were expected to occur, specifically, when there was a high concentration of suspended frazil or when the concentration of surface pans/rafts was high. In Fig. 3.5, the detected bottom of pans/rafts using this algorithm (black line) is superimposed on the 2D plots of raw counts. The *persistence* and *threshold* values were calibrated by manually examining the detected targets and checking if they correctly followed the bottom of the

pans/rafts. Both Fig. 3.5a (high suspended frazil concentration) and Fig. 5b (high pan concentration), illustrate that the algorithm was able to accurately detect the lower edge of pans/rafts even under these challenging conditions. The number of false targets (indicated by red ovals in Fig. 3.5) detected in a 24 hour period of extreme conditions (86400 profiles) ranged from 10 to 20, which corresponds to an accuracy of ~ 99.98%. It is important to note that the *threshold* and *persistence* level are considered site specific and are also a function of the gain setting of the sonar used during the deployment. Therefore, the optimal *threshold* and *persistence* level would likely need to be determined in a similar manner for each deployment and site.

The algorithm then calculates the pans/rafts drafts, t_p (m) by subtracting the water depths (shown as a white dotted line in Fig. 3.5), calculated using Eq. 3.1, from the ranges of the detected targets (i.e. pan bottoms). When no pans/rafts were present at the surface, this difference varied from 0 to 4.4 cm; therefore, the algorithm assumes any computed drafts less than 5.0 cm to be zero. In order to calculate pan/raft lengths, l_p (m), the algorithm uses a logical function to convert the time series of pan/raft drafts into a binary vector with false (0) indicating no pan/raft detected and true (1) indicating a pan/raft is detected. For example, if a pan was detected for four seconds above the sonar it would appear as four consecutive ones with zeros on either side in the binary vector. The algorithm uses the binary vector to compute the duration each individual detected pan/raft is present above the sonar. Pan/raft lengths, l_p (m) are then estimated by multiplying the duration by the corresponding near-surface (within 10 cm from the surface; the minimum bin size for the ADCP) water velocity (averaged over 5 minutes) which is assumed to be the ice velocity. Generally, as long as the surface ice is not impeded by physical constraints (e.g.: bridging or ice cover formation) the surface ice must be moving at the same velocity as the surface water because of the no slip boundary condition. For surface ice concentrations less than ~70%, pans/rafts are expected to have no effect on the surface velocity (Morin et al., 2000; Morse et al., 2003). However, at higher surface concentrations (> 70%), congestion and

bank resistance would be expected to combine to impede pan movement causing the surface ice velocity and consequently the surface water velocity to be reduced. Surface ice concentrations, C_s (%) were calculated every 30 minutes by summing the number of profiles with non-zero drafts and dividing by 1800 (i.e. the total number of profiles produced in 30 minutes).

Fig. 3.6 shows a comparison between histograms of pans/rafts drafts, t_p (m), lengths, l_p (m) and the surface concentrations, C_s (%) estimated from the low and the high frequency sonar data. Note that this data set was produced using the same threshold of 60,000 and persistence level of 6 bins for both units. It is evident from Fig. 3.6 that data computed from both units are in reasonable agreement. Statistical tests on the means (*t*-test) and variances (*Levene*-test) of the distributions of t_p, l_p, and C_s, showed that surface ice properties computed from the high and low frequency sonar data are statistically similar at the 95% confidence limit. Therefore, only ice characteristics computed from the high frequency sonar will be plotted and discussed in the subsequent sections, because the high frequency data set was more complete and the instrument experienced fewer problems during the deployment.

3.5 Data Validation

A number of different river ice phenomena were easily distinguished by visual inspection of the sonar data. For example, the presence of open water, surface pans/rafts, or a solid ice cover was readily apparent in the time series plots of raw digital sonar data. These visual inspections were verified using the webcam images obtained. The surface ice conditions determined by visual inspection of the sonar data were always in agreement with the conditions observed in the corresponding webcam images.

To assess the validity of the computed pan/raft lengths, l_p (m) obtained from the sonar data, pan/raft lengths were compared with pan/raft lengths scaled from the webcam images. The images were read in the Matlab Image Processing Toolbox,

and pans/rafts were digitally measured parallel to the flow direction, to be consistent with the lengths measured by the sonar. Fig. 3.7 shows a sample webcam image used for pan/raft lengths scaling. The sampling size was much smaller in the case of the webcam images compared to the sonar data because, at most, 4 to 5 pans could be scaled from each image and images were only taken every 30 min (compared to the 1Hz sampling frequency of the sonar). Also, the number of available images was limited by the fact that only daytime images, with no fog or heavy snow blocking the view of the camera, could be used. In addition, only length measurements of pans/rafts passing within ~4 m of the bank in the webcam images were used to reduce the errors associated with image distortion (the area below the dash line in Fig. 3.7). These restrictions limited the number of pans/rafts measured from the images to ~50 per day (compared to the several hundred pans/rafts measured with the sonars). Therefore, the validation of pan/rafts lengths was done by comparing the daily average lengths from the sonar and the images, over 7 hour periods of daylight (from 09:00 to 16:00), for 4 consecutive days from 12-Nov09 to 15-Nov-09. Over this time period, the mean pans/rafts lengths measured by the sonars ranged from 2.05 to 2.25 m, while the pan/raft lengths estimated from the images ranged from 1.7 to 1.9 m. Although pan/raft lengths measured by the sonar were on average 15 % larger than those lengths measured from the images, but they were comparable in size. It might be that pans/rafts closer to the bank were actually physically smaller, or this difference might simply reflect the fact that the image sample size is approximately one order of magnitude smaller than the sonar sampling size.

In order to determine how accurately the sonars instruments are able to detect the bottom of floating pans, a set of laboratory experiments was conducted in the frazil tank described in Ghobrial et al. (2012). The experiments consisted of generating frazil ice in a stirred tank of supercooled water until the frazil particles started to flocculate. At this point the mechanical stirring was stopped to allow the frazil particles and flocs to rise to the surface where they formed a stable slush layer. A point gauge was then used to manually measure the location of the

bottom of the slush and this measurement was compared to bottom of the slush layer observed in the sonar data once the signal was above the threshold of 60,000 counts. The sonar measurements were found to be accurate to ± 1.1cm, which is the cell size of the instrument.

Direct measurements of pan/raft drafts were also conducted at the field deployment site on 26-Nov-09 and compared to the drafts estimated from the sonar data. A Trimaran equipped with an underwater video camera and a rod with a vertical scale, was used for these measurements (Fig. 3.8a). The vertical rod was mounted so that ~ 50cm of the scale was in the field of view of the camera. The Trimaran was pushed out into the flow using a 4 m long pole and positioned so that it was adjacent to a floating pan or raft (Fig. 3.8b). The Trimaran was held in position for few seconds adjacent to the pan/raft to allow sufficient time to record video images of the pan/raft bottom. A total of 18 pans/rafts were examined in this way and drafts were extracted from the resulting video by comparing the location of the pan bottoms with the vertical scale on the rod. Statistical parameters of drafts extracted from the video recording and drafts computed from the sonar data during the same time period are compared in Table 3.2. Drafts computed from the sonar data and those observed in the video recording were reasonably consistent, especially given the small sample size of the underwater video data set and the fact that drafts were measured much closer to the bank in the case of the underwater video.

3.6 Results and Discussion

3.6.1 Synopsis of Freeze-up Season

The monitoring program began on 15-Oct-09 and ended on 13-Jan-10. A summary of the hydro-meteorological conditions observed during this time period is presented in Fig. 3.9 including time series plots of the air temperature, T_a (°C), water temperature, T_w (°C), water depth, h (m), mean current velocity, u (m/s), and snowfall depth, d_s (cm) from 3-Nov-09 to 12-Jan-10. The water depth and the mean velocity time series were always in phase with each other and were both

dominated by the 24 hour hydro-peaking cycle on this river controlled by the Bighorn and Brazeau dams upstream (Fig. 3.9c and d). For a typical daily hydro-peaking cycle, h and u peaks ~18:00 with average values of 2.0 m and 0.5 m/s, respectively; and the troughs occurs ~06:00 with average values for h and u of 1.8 m and 0.3 m/s, respectively. In order to visualize trends in the time series and to decrease the noise in the data, a 30 min moving average was applied to the time series of C_s, t_p, and l_p. Time series of C_s, t_p, l_p and t_p / l_p are presented in Fig. 3.10 for the same time period.

Water temperatures decreased gradually starting on 3-Nov-09 and the first supercooling was observed on 12-Nov-09. Frazil pans were first observed at the site on 9-Nov-09 and surface ice concentrations increased from 0% to ~50% on 12-Nov-09 (Fig. 3.10a). From 13-Nov-09 until 2-Dec-09, the surface ice concentrations ranged from 30% to 60% (Fig. 3.10a), and the water temperature fluctuated between -0.05 and 0.5˚C (Fig. 3.9b). In the first week of December, air temperatures dropped below -20˚C and were between -20 and -30˚C for the next two weeks (Fig. 3.9a). Cold air temperatures, combined with heavy snowfall events (Fig. 3.9e), resulted in a significant increase in surface ice concentrations; approaching 80 to 90% by 4-Dec-2009 (Fig. 3.10a). During this time period, ice rafts began to accumulate along the banks and bridging occurred at a number of locations along the river. Fig. 3.9c shows the stage-up in water depth on 5-Dec-09 due to backwater effects caused by ice cover formation downstream of the study site.

The ice front progressed upstream past the study site on 6-Dec-09 and a solid ice cover was present at the site from 8-Dec-09 to 16-Dec-09. Warm water outflows from the Gold Bar *WWTP* initiated an open water lead which progressed downstream to the study site on 17-Dec-09, encompassing about one-third of the river width at the study site. Colder air temperatures from 20 to 25-Dec-09, and again from 29-Dec-09 to 1-Jan-10, resulted in the development of new frazil pans in this open lead. Despites the cold air temperatures the open water lead expanded to span ~50% to 60% of the channel width at the study site by 5-Jan-10 and the

width of the open lead remained constant at the site through to 13-Jan-10, the day the instruments were retrieved.

For the purpose of analyzing the surface ice characteristics, the freeze-up season was divided into three consecutive time periods based on the major surface ice phenomena that were observed during the monitoring period, specifically: frazil pans, ice cover and open lead. These three time periods are labeled in Figs. 3.9 and 3.10. The frazil pan period was further sub-divided into three consecutive phases. Phase I: the time period between when surface ice first appeared at the site and when the surface ice concentration reached ~50%; Phase II: the time period when the surface ice concentrations were relatively consistent and averaging ~ 50%; and Phase III: the period leading up to the solid ice cover stage, during which the surface ice concentrations were highly variable.

3.6.2 Frazil Pans

3.6.2.1 Phase I:

Phase I began on 9-Nov-09 when frazil pans first appeared at the site and ended on 13-Nov-09 when the surface ice concentration reached approximately 50% (Fig. 3.10a). The air temperature during this time period varied between +5 to +10°C in the morning, and between -5 to -10°C at night (Fig. 3.9a). Starting on 8-Nov-09, the water temperature decreased at a rate of ~0.5°C/day and the first supercooling occurred at the measurement site on 12-Nov-09 (Fig. 3.9b). The water depth and the mean velocity followed the 24 hrs. hydro-peaking cycle and ranged from 1.8 to 2.0 m and from 0.3 m/s to 0.5 m/s, respectively (see Fig. 3.9c and d).

Fig. 3.11 presents a series of daily webcam images taken from 8-Nov-09 until 15-Nov-09 showing the evolution of surface ice conditions at the deployment site. On 9 and 10-Nov-09, pans/rafts were seen in the webcam images (Fig. 3.11) and detected by the sonar as two sharp spikes in surface concentration (Fig. 3.10a), despite the fact that the water temperature did not reach supercooling yet at the

site (Fig. 3.9b), and the average measured air temperature was above zero on both days (Fig. 3.9a). These two spikes had very similar characteristics: they both lasted for ~ 4 hours and occurred on the same time of the day (from 10:00 to 14:00) with a peak value of C_s ~30%. Air temperatures measured upstream of the city of Edmonton (Edmonton International Airport, station ID#3012205, ~20 km upstream of the deployment site) reached approximately -10°C overnight on 9 and 10-Nov-09 (Environment Canada, 2011). This indicates that upstream of the city, the water might have been supercooled and frazil ice generated overnight, forming bigger flocs that were then conveyed to the deployment site in the next morning. Frazil generation probably stopped during the day when the air temperature was above 0°C. These pans/rafts consisted mainly of partially submerged frazil slush that had not yet formed floating crusts as shown in the 10-Nov-09 image in Fig. 3.11. Also, they were still very thin with drafts less than 0.1 m, and lengths less than 1.0 m (Fig. 3.10b and c); which indicates that they were melting due to warmer air and water temperature.

On 11-Nov-09 from 07:00 to 15:00, C_s increased from 0 to ~50% (See Fig. 3.10a). Figs. 3.10b and c show that from 11-Nov-09 to 13-Nov-09, pan\raft drafts and lengths increased gradually from ~0.08 to ~0.30 m and from 0.5 to 3.0 m, respectively. Although this increase in pan/raft dimensions was significant (~80% increase), the average ratio between the two, t_p / l_p, remained approximately constant at ~0.1. This suggests that frazil pans/rafts tend to keep a constant dimensional ratio during its evolution in size.

3.6.2.2 Phase II:

This phase represents a relatively consistent period during which frazil pans/rafts, of surface concentration between 30 and 60 %, were continuously seen passing by the site and detected with the sonar (see Fig. 3.10a). Images of typical frazil pans/rafts observed during this phase taken on 14 and 15-Nov-09 are shown in Fig. 3.11. Phase II lasted for 19 days, from 13-Nov-09 until 2-Dec-09 (see Figs. 3.9 and 3.10), during which the air temperature, T_a, fluctuated between -10 and +

10 °C (Fig. 3.9a). The water was supercooled ~70% of the time, although there were two brief periods of slightly warmer water temperatures, reaching up to +0.6˚C (see Fig. 3.9b). These brief periods of locally slightly warmer water (max +0.6˚C) probably had a negligible effect on surface ice characteristics detected at the site. Figs. 3.10b and 3.10c show that, generally, t_p and l_p varied between 0.1 and 0.4 m, and 1.0 and 3.0m, respectively, during this phase. From 17 to 22-Nov-09, the average t_p decreased to ~ 0.15 m due to the continuous warmer air and water temperatures during this time period (see Figs. 3.10b and Fig. 3.9a & b). This decrease in t_p caused the daily average t_p / l_p to drop below 0.1 from 17 to 22-Nov-09; it then increased to ~0.15 until the end of Phase II.

A daily periodic variation of approximately ± 0.07 m in t_p and ±0.50 m in l_p, is evident in Figs. 3.10b and 3.10c. Typically, t_p and l_p increased in the morning (from 9:00 to 12:00) and decreased at night (from 18:00 to 21:00). Comparing Fig. 3.9a with Figs. 3.10b and 3.10c, it was observed that t_p and l_p increased with decreasing air temperature, T_a. This relation is expected because lower air temperatures early in the day is more likely to cause supercooling of the water, and respectively the generation of more frazil ice that contributed in thickening and lengthening floating pans/ rafts. Also, another possible explanation for why drafts were larger in the morning and became thinner and smaller in the evening, is the effect of the warm water discharge from the waste water treatment plant (*WWTP*). A typical winter daily discharge from the *WWTP* has a temperature between 12 and 16 °C and would peak in the evening (from 15:00 to 18:00) with a maximum discharge of ~3.5 m^3/s; and reach its minimum discharge of ~1.2 m^3/s in the morning (from 6:00 to 9:00). For an average stream velocity of ~0.5 m/s, the warm water effluent would need ~3hrs to reach the deployment site; which explains the 3 hours shift in phase between the time the minimum warm water discharge occurred and the time when the maximum pans/rafts sizes were observed at the site.

3.6.2.3 Phase III:

During Phase III, varying ice processes and surface ice concentrations were observed at the site, preceding the formation of the ice cover. This phase lasted for 5 days from 2-Dec-09 to 6-Dec-09, during which air temperatures were consistently below 0˚C and the water was supercooled more than 80% of the time (see Figs. 3.9a and 3.9b). From 2 to 3-Dec-09, t_p increased gradually from ~0.3 to ~0.6 m and l_p increased from ~2.0m to ~20.0m (Figs. 3.10b and 3.10c). As a result the average t_p/l_p dropped to 0.05 (Fig. 3.10d). Fig. 3.12 presents daily webcam images from 1-Dec-09 until 8-Dec-09. A 2-D plot of the sonar raw data and the corresponding surface ice concentration are presented in Fig 3.13 for the same time period, showing the transition from the frazil pans/rafts phase to a solid ice cover. From 1 to 3-Dec-09, several suspended frazil events were detected by the sonars, which indicates that most likely there was more frazil ice generated upstream that contributed to the increase of C_s, t_p, and l_p during this time period (Fig. 3.13a). Surface ice concentrations increased significantly; approaching 80 to 90% by 3-Dec-2009 (see Figs. 3.10a and 3.13b) and ice rafts began to accumulate along the banks (Fig. 3.12).

Velocity profiles obtained on 2 and 3-Dec-09, and time-averaged from 00:00 to 03:00 are plotted in Fig. 3.14. The near-surface (within 0.1 m) water velocities; indicative of the surface ice velocities; decreased by ~20% (Fig. 3.14) while surface ice concentrations increased from ~50% to ~90% from 2-Dec-09 to 3-Dec-09. This behavior is expected at higher surface concentrations (C_s >70%) because pans/rafts tend to decelerate at high concentrations due to congestion and interactions with the shorefast ice. A scatter plot of the non-dimensional near-surface water velocities (u_s/u) sampled over the entire pan/raft period (phases: I, II, and III) versus the corresponding surface concentration, C_s (%), is plotted in Fig. 3.15. It is evident in Fig. 3.15 that the average measured u_s/u is almost constant up to $C_s \approx 75\%$, then the ratio start to decrease at higher C_s. The data in Fig. 3.15 have been compared to the following exponential equation,

$$u_s = \frac{u}{\varepsilon + e^{\eta\left(\frac{C_s - C_{so}}{100}\right)}} \qquad (3.2)$$

where, u_s is the near-surface velocity (m/s), u is the depth average velocity (m/s), ε and η are constants that control the y-intercept and the shape of the curve, respectively, C_{so} (%) is the threshold of surface concentration at which the surface velocity starts to decrease, and C_s (%) is the surface ice concentration. In Fig. 3.15, Eq. (3.2) was plotted using η = 20 and for the lower, average and higher envelopes, ε = 1.2, 1.0, and 0.8; and C_{so} = 80, 90, and 100%, respectively.

A fixed-wing aircraft flight along the river from Fort Saskatchewan (~30 km downstream of the deployment site) to Devon (~40 km upstream) was conducted on 3-Dec-09 to document surface ice conditions. In Fig. 3.16 an image taken during this observational flight shows that the surface ice concentration was approximately 70 to 90 % over the instruments at 12:00, which is consistent with the ~85% surface concentration estimated from the sonar data at the same time (Fig. 3.10a). Fig. 3.16 also shows that there was a constriction in the active flow channel approximately 1.0 km upstream of the deployment site, where shorefast ice (primarily lodged rafts and pans) had reduced the open water width by approximately two-thirds. As Fig. 3.16 shows, ice congestion in this constriction caused surface ice concentrations to approach 100% locally. At this ice exited the constriction, it gradually re-split into large rafts, completing the process just downstream of the instrument deployment site. These large rafts were still several hundred meters long in the vicinity of the sonar instruments (Fig. 3.16). In contrast, the maximum pan lengths measured by the sonar instruments were only ~20 m during this time period (Fig. 3.10c). Jasek and Marko (2008) noted a similar discrepancy when comparing sonar data and photographic observations on the Peace River. They suggested that the difference might be due to the fact that the frazil slush profile on the underside of these newly formed large rafts might still reflect the variability between the individual pans and rafts that comprise

them, something the sonars could detect, but not distinguishable from photos of the ice surface.

As shown in Fig. 3.17, between 15:00 and 17:00 on 3- Dec-09 the water depth, ice surface concentration and pans/rafts drafts suddenly decreased then increased again. Water depths dropped ~0.10 m then increased by ~0.20 m. At the same time, surface ice concentrations dropped from ~80% to 20% then increased to ~90%. Measured pan/raft drafts jumped from ~0.5 m to ~0.8 m as the depth and ice surface concentration began to increase. It is believed that these fluctuations occurred as a result of a brief period of increased ice congestion at the constriction just upstream of the instruments site (see Fig. 3.16). Although these data indicate that complete bridging did not occur, it is likely that an ice accumulation began to develop in the constriction, backing up water and ice temporarily before releasing downstream.

Starting on 4-Dec-09, the surface ice concentration decreased until it reached ~0% by the end of the day (Figs. 3.10a and 3.13b). This decrease in surface ice concentration was associated with a decrease in water depth from 2.0 m to 1.7 m (Fig 3.13a) indicating that bridging event was likely occurring in the constriction upstream of the instrument site. Also on 4-Dec-09, a heavy snowfall event (d_s > 15cm) occurred (Fig. 3.9e) and, as a result, evidence of floating snow slush was seen in the corresponding webcam image (Fig. 3.12). From 18:00 on 4-Dec-09 to 03:00 on 5-Dec-09, entrained snow slush from this snow fall event, was detected by the sonar as shown in Fig. 3.13a. Snow slush is fine-grained compared to frazil slush (Osterkamp and Gosink, 1983). Therefore, its weaker signal was below the pre-set *threshold* for pan detection, and was not detected as a pan target that would affect the surface ice concentration.

From 03:00 to 12:00 on 5-Dec-09, the water depth increased by 0.5 m reaching a depth of 2.4m (Fig. 3.9c). Over this same period, the depth averaged velocity decreased from 0.4 m/s to 0.2 m/s (Fig. 3.9d). As Fig. 3.13a illustrates, this depth increase was not simply due to due to hydro-peaking, and this, combined with the

observed velocity decrease, suggests that it was due to backwater effects, likely caused by bridging and subsequent ice cover formation downstream of the site.

3.6.3 Ice Cover

By, 6-Dec-09 an ice front had progressed upstream to the study site (e.g. see Fig. 3.12) and the river was mostly ice covered except for a small opening just over the instrument platform. Over the ensuing two days, this opening eventually froze over. As seen by the sonar returns at the surface (Fig. 3.13a) that the ice cover started to thicken above the transducer at about 16:00 on 7-Dec-09, but the surface ice concentration did not reach 100% until 06:00 on 8-Dec-09 (Fig. 3.13b). This discrepancy is due to the fact that, before 06:00 on 8-Dec-09, the ice draft (water surface minus bottom of ice) was below the minimum threshold of 5 cm that the processing algorithm can detect. An ice cover was formed at the site from 8 to 16-Dec-09. At 00:00 on 11-Dec-09 the estimated surface concentration dropped to 0% and at 00:00 on 13-Dec-09 it increased abruptly to 100% (see Fig. 3.10a). This temporary drop was caused by the formation of a small hole in the ice cover directly over the sonar location during these two days. The sonar detected ice cover thicknesses were less than 0.1m (Fig. 3.10b) during the time a cover was locally formed over the transducer.

3.6.4 Open Lead

Warmer air temperatures combined with warm water from the *WWTP* (Fig. 3.10a and b) initiated an open lead that started at the *WWTP* (~ 6 km upstream) and progressed downstream past the study site on 17-Dec-09. Fig. 3.18 shows a typical webcam image taken on 21-Dec-09, during the open lead period that persisted at the study site at least until the end of the deployment on 13-Jan-10. During this time period, the average daily air temperatures were typically below -10°C (Fig. 3.9a) and the water temperature followed a diurnal cycle which included several supercooling events (Fig. 3.9b).

From 21-Dec-09 to 4-Jan-09, the instruments documented daily average water depths and flow velocities ~15% higher the average values observed during the open water and frazil pan phases (Figs. 3.9c and 3.9d). This implies an increase in the river discharge; however, published discharge data from the Water Survey of Canada (WSC) gauge at Edmonton (ID# 05DF001, 12 km upstream) actually show that the river discharge was ~50% lower during the open lead period compared to the open water period (~60 m^3/s vs. ~130 m^3/s). Since there are no substantive lateral inflows between the gauge and the study site, the most likely explanation is that the flow was concentrated in the open lead because of its greater hydraulic efficiency, causing the water level and velocity to rise locally. By 5-Jan-10, the water depth and velocity had again decreased by ~10% compared to the values measured during the previous 2 weeks (Fig. 3.9c and 3.9d). This decrease was probably due to the expansion of the open lead portion to ~ 50% of the river width, compared to ~33% of the river width for the period from 21-Dec-09 to 4-Jan-10.

Fig. 3.19 presents the water temperature, T_w (°C) and the surface ice concentration, C_s (%) measured at the site during the open lead period. From 20-Dec-09 to 6-Jan-10, slushy frazil pans, which had not yet developed surface crusts (see Fig. 3.18), were observed passing the instrument site during the daylight hours, causing approximately eleven spikes in C_s ranging up to 20% to 50% in magnitude and on average 9 hours in duration (from 09:00 to 18:00) (see Fig. 3.19). In each case, the peak surface ice concentration coincided with the minimum water temperature recorded that day, and these peaks were significant (i.e. C_s > 10%) only when water temperatures were below ~ 0.1 °C. These slushy pans were probably freshly formed by suspended frazil that was generated by supercooling in the open lead during the morning hours when the discharge of warm water from the *WWTP* was minimum (from 06:00 to 09:00), and were conveyed to the site between 09:00 and 18:00. Once the warm water discharge from the *WWTP* started to peak in the evening hours (from 15:00 to 18:00) the slushy pans melted rapidly causing the surface ice concentrations at the site to

drop back to 0% after ~18:00. These slushy pans were very similar in shape and dimensions ($t_p/l_p \approx 0.1$) to the slushy pans observed during phase I on 9 and 10-Dec-09 (Fig. 3.11), averaging ~0.1 m thick and ~1.0 m long (Fig. 3.10b and 3.10c). Colder air temperatures (T_a < -30°C) from 29-Dec-09 to 1-Jan-10 (Fig. 3.9a), caused the surface ice concentrations to be above 0% continuously from 30-Dec-09 to 2-Jan-10 (Fig. 3.19).

3.7 Summary and Conclusions

Freeze-up processes were monitored on the North Saskatchewan River in Edmonton, AB, Canada during the 2009/2010 freeze-up season. Upward looking sonars, a water current profiler and an onshore monitoring station were deployed at the study reach. The deployment location was downstream of the city waste water treatment plant which periodically discharged warm water, affecting ice processes and characteristics at the site. A MATLAB® code was written to process the raw sonar and current profiler data in order to extract the surface ice concentration, pan drafts and lengths. Statistical tests of the similarity of the results from the high (546 kHz) and low frequency sonar (235 kHz) units showed that either instrument is suitable for the purpose of surface ice measurements. The ice measurements computed from the sonar data were validated with laboratory tests, webcam images and in-situ measurements demonstrating that this technique provides reliable measurements of local surface ice characteristics.

For analysis purposes, the freeze-up season was divided into three distinct time periods: frazil pans, ice cover, and open lead. The frazil pans period was further sub-divided into three phases: Phase I was defined as the ice initiation phase, phase II as the consistent surface ice concentration phase, and phase III as the transition between the pan phase and the formation of the continuous ice cover. Similar phases of frazil pan evolution were also observed on the Peace River data during 2006 and 2010 freeze-up (Jasek and Marko, 2007; Jasek et al., 2011).

At the deployment site, pan characteristics observed early during Phase I and during the open lead periods, were very similar. Pan/raft drafts and lengths were ~ 0.1 m and 1.0m, respectively. During Phase II (consistent surface ice concentrations), pan drafts generally ranged between 0.1 to 0.4 m and pan lengths between 1.0 and 3.0 m, with the ratio of draft to length ranging between 0.1 and 0.2. An exponential expression was proposed to model the field measurements of the non-dimensional near-surface velocity to its corresponding surface concentration during the frazil pans/rafts period. However, the parameters of this equation are site specific and need to be validated for each deployment. It was observed that the hydraulics of the open lead segment (water depth and velocity) was directly related to the percentage of the open portion of the channel width.

The proposed algorithm provided quantitative (as opposed to qualitative) measurements of the surface ice characteristics using upward looking sonars. Field data processed using this algorithm are very precise and can be used for the validation of numerical models and to adjust models parameters for better predictions of the surface ice conditions (e.g. Jasek et al., 2011). The upward looking sonar proved to be a robust tool for continuous measurements of the surface ice properties but only limited in space to the instrument location.

Tables

Table 3.1 Sonar parameters used for field deployment.

Parameter	Low freq	High freq
Pulse length (μs)	68	34
Gain	1	1
Ping frequency (Hz)	1	1
Sensor frequency (Hz)	0.1	0.1
Sound speed (m/s)	1403	1403

Table 3.2 Comparison of pan/raft drafts t_p (m) measured with the underwater video and with the sonar on 26-Nov-09.

Parameter	Sonar	Underwater video
Min	0.05	0.18
Max	0.63	0.45
Mean	0.26	0.32
Std dev	0.07	0.08

Figures

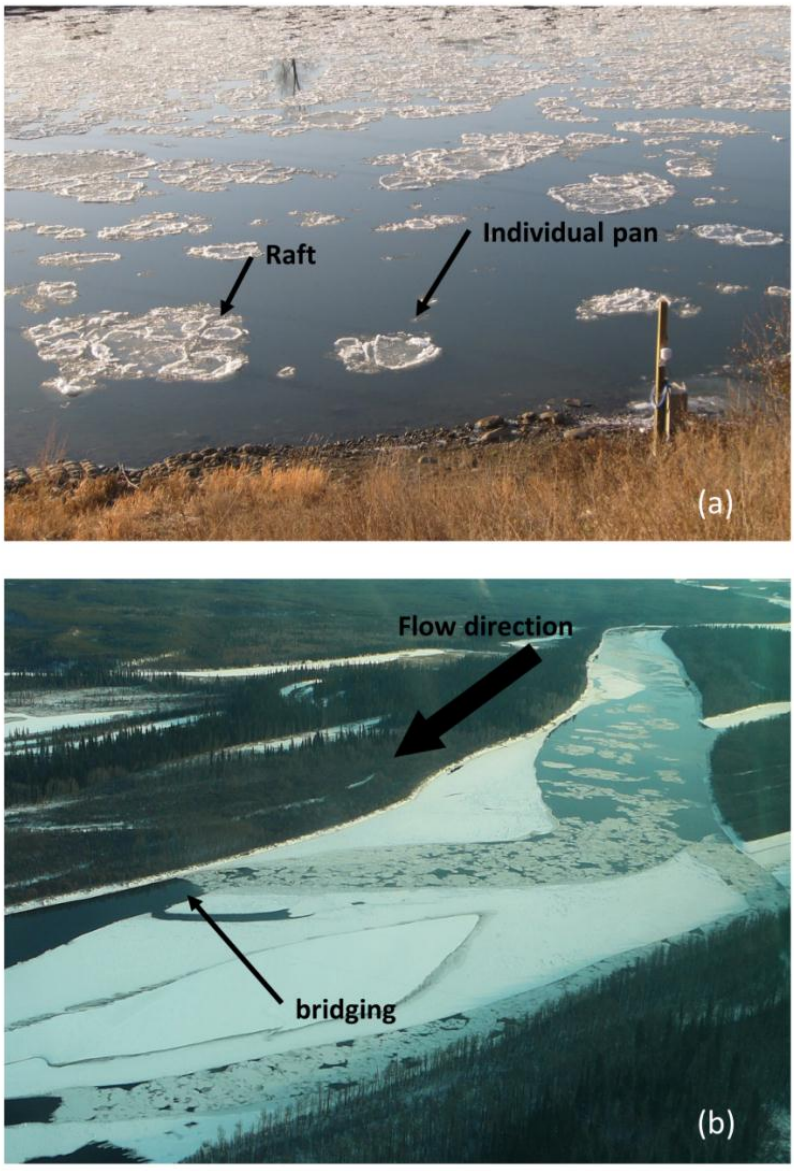

Fig. 3.1. Initial stages of ice cover formation on large rivers: (a) pancake ice, also known as "pan ice" or "frazil pans", and frazil rafts (picture taken on the North Saskatchewan River in Edmonton), (b) bridging (picture taken on the Athabasca River, downstream of Fort McMurray).

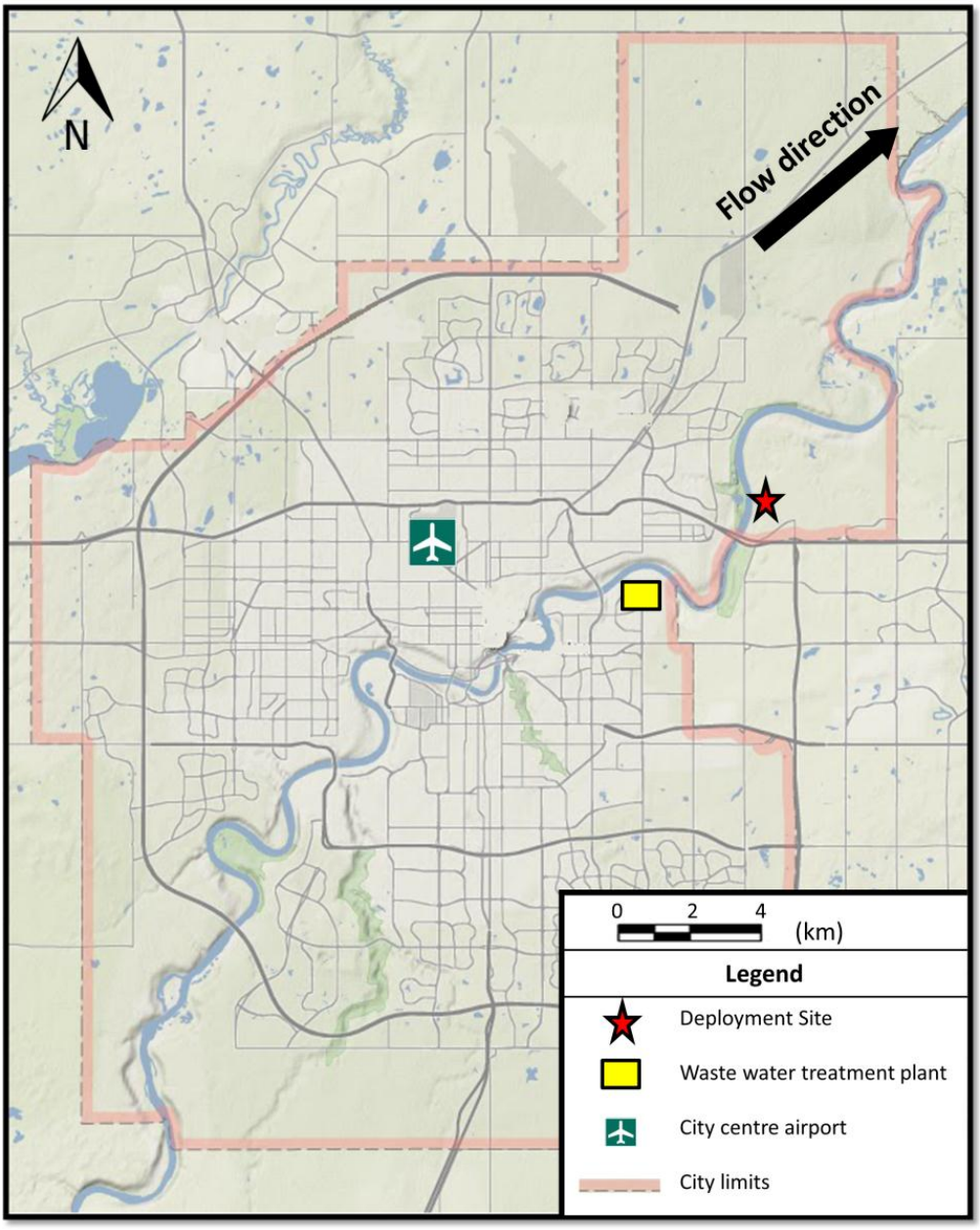

Fig. 3.2. Satellite Google ® Map of the North Saskatchewan River in the vicinity of Edmonton showing: the deployment site, the city centre airport, and the city Gold Bar waste water treatment plant.

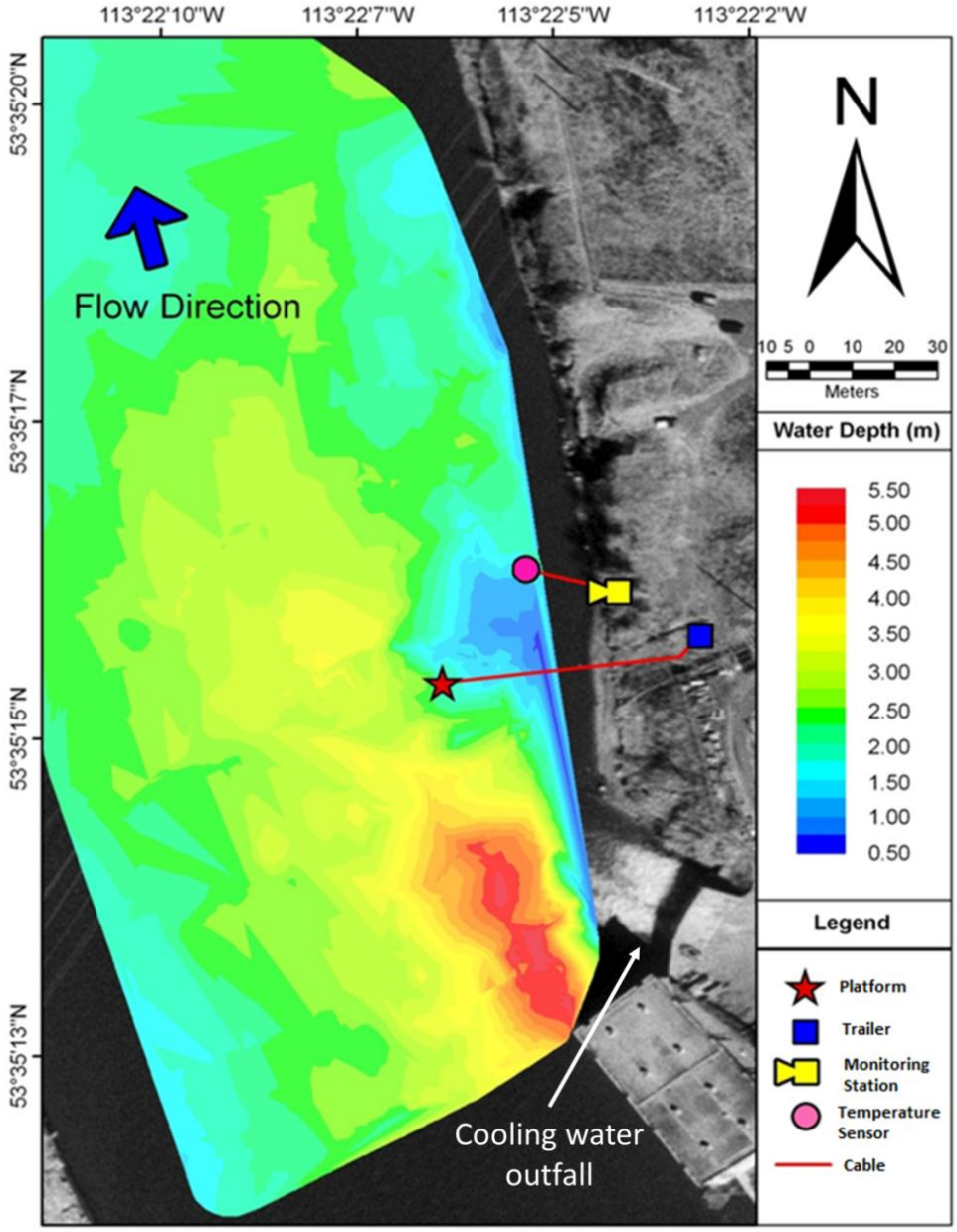

Fig. 3.3. An aerial photograph of the deployment site with the bathymetric survey in 0.5 m increments plotted in color showing the locations of the instrument platform, temperature sensor, monitoring station (Webcam) and trailer. The power station's cooling water outfall and the river-water pump house are also shown.

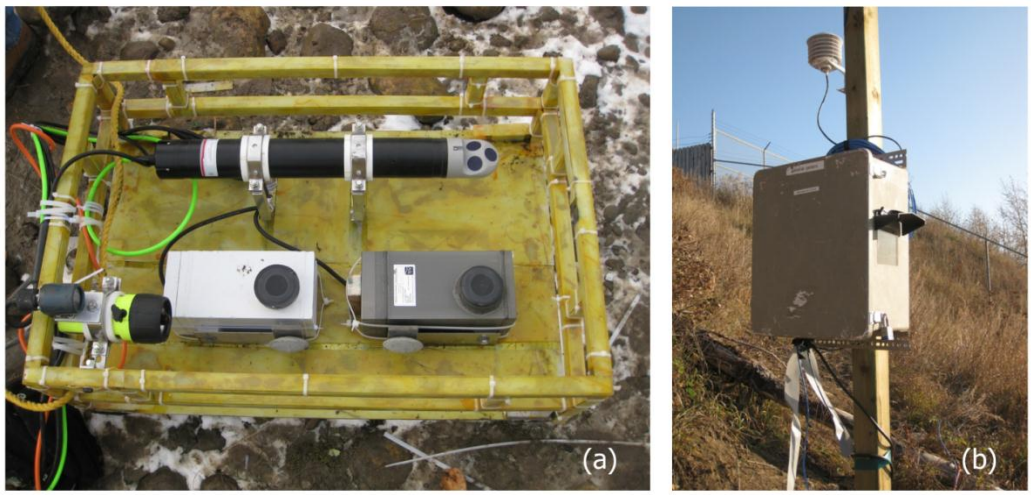

Fig. 3.4. (a) picture of the deployment platform used to hold the in-stream instruments showing both the high and the low frequency sonar units, the water current profiler, and the underwater video camera and light. (b) A picture of the monitoring station pointing at the water surface and equipped with a webcam and a wireless antenna for sending images and water and air temperatures wirelessly to the University of Alberta website.

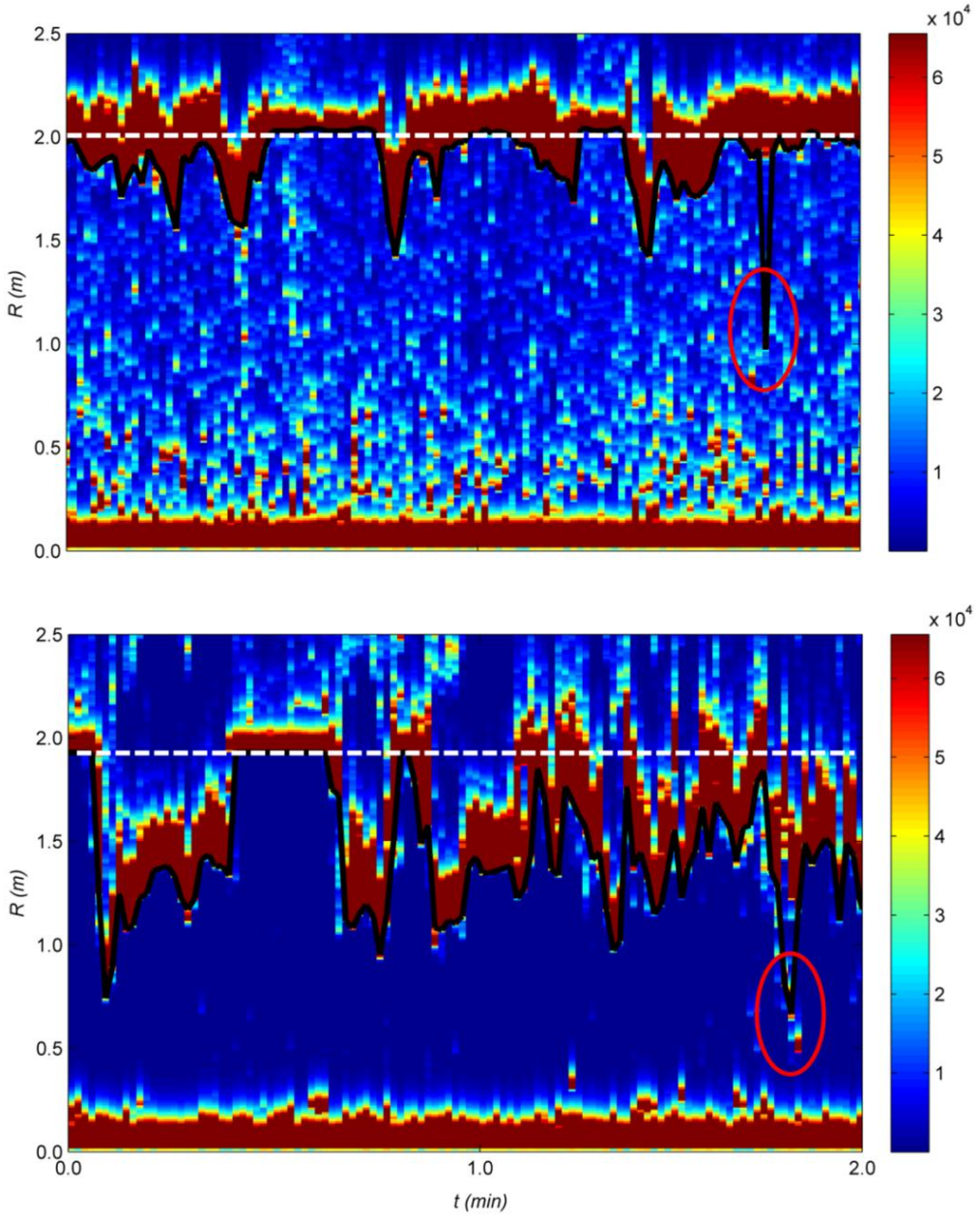

Fig. 3.5. Plot showing the detected bottom of the pans (black solid line) on a 2-D plot of raw counts (color coded) for a 2 min time interval showing range *R* (m) versus time *t* (min) at two extreme conditions: (a) high suspended frazil concentration on 1-Jan-10, and at (b) high pan concentration on 3-Dec-09. The white dotted line and the red ovals in (a) and (b) indicate the water surface and false targets, respectively.

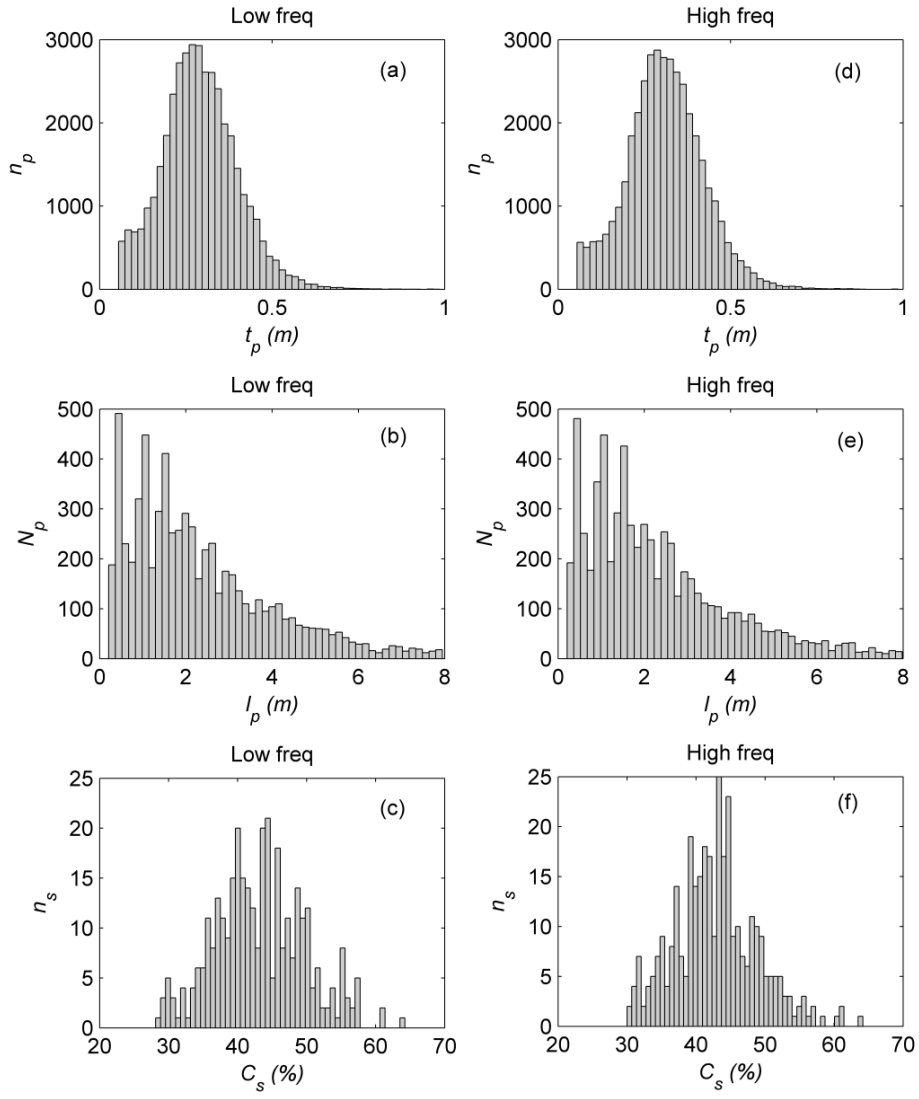

Fig. 3.6. Histograms of calculated pans drafts t_p (m) versus the number of sonar pings with pans n_p , pan lengths l_p(m) versus number of individual pans N_p (both sampled every 1 Hz for a 24 hour period on 14-Nov-09), and surface concentration C_s (%) versus number of samples n_s , (sampled every 30 minute for seven days' time period from 14-Nov-09 to 20-Nov-09) from the low frequency unit in (a), (b), and (c) and from the high frequency unit in (d), (e), and (f).

Fig. 3.7. A sample webcam image taken with the monitoring station on 13-Nov-09 at 14:00 for the river ice condition showing an example of a raft length scaled from the image. Only pans/rafts below the dash line were used for these measurements. The blue star indicates the approximate location of the instrument's platform.

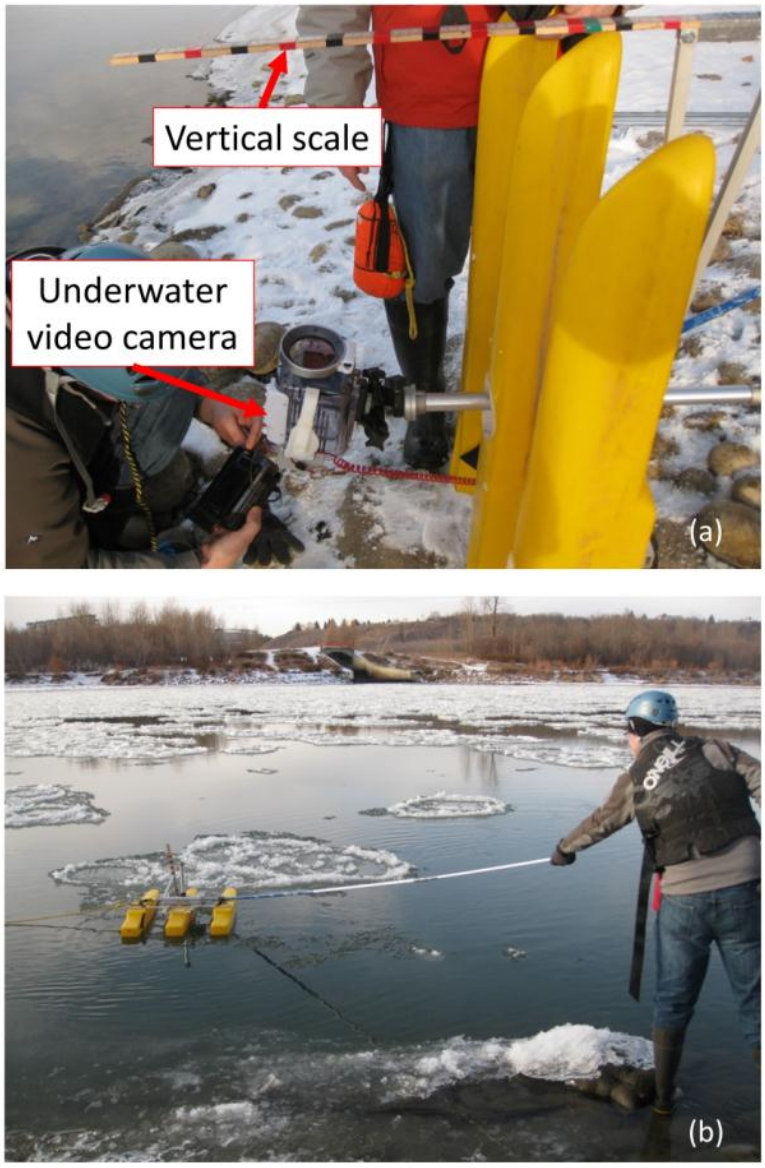

Fig. 3.8. The underwater camera setup on the Trimaran on 26-Nov-09 for measuring pans drafts; (a) the underwater camera pointing at the scaled ruler, and (b) while pushing the Trimaran towards a passing frazil raft.

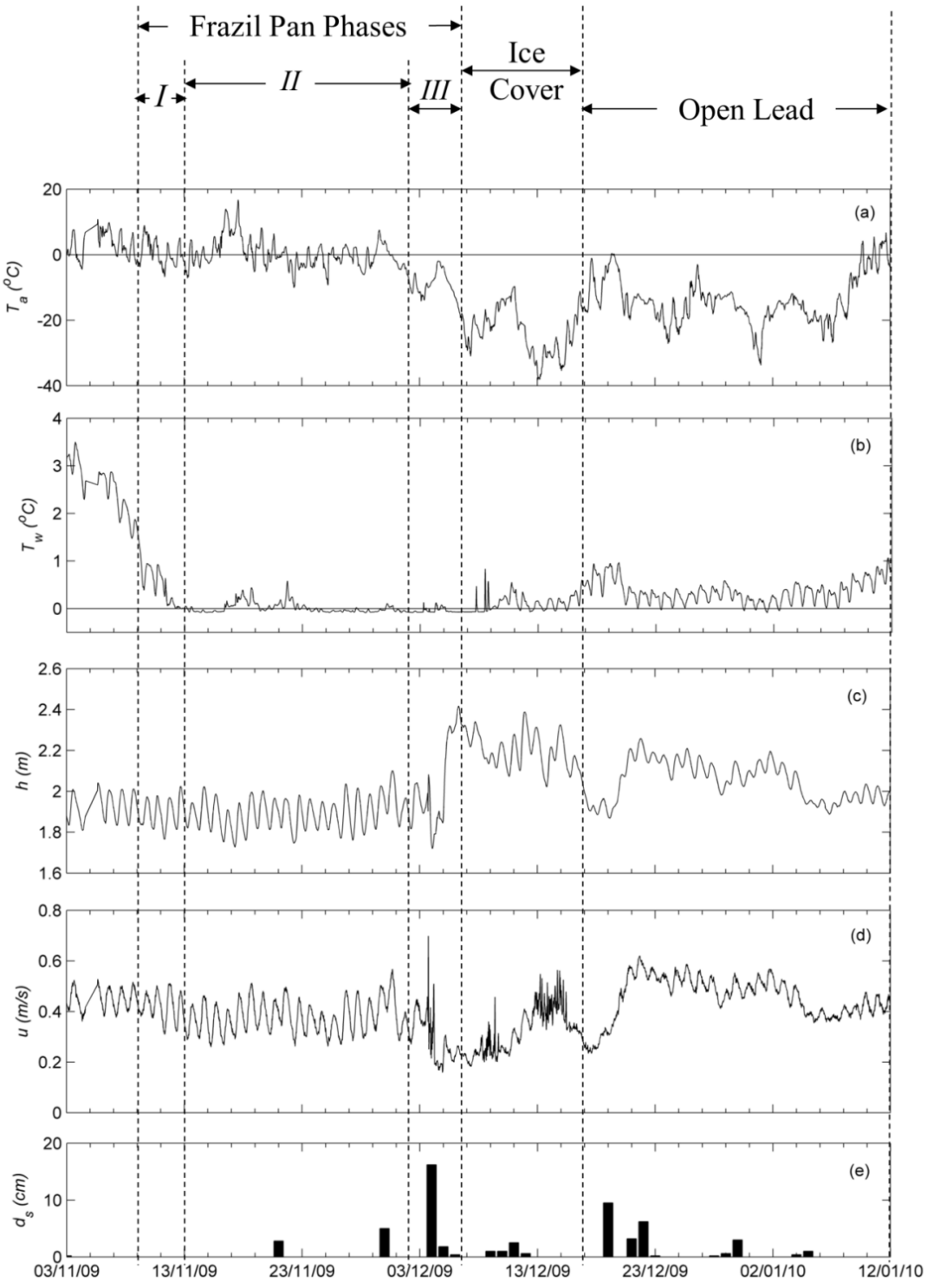

Fig. 3.9. An overview of the hydro-meteorological conditions measured at the deployment site during the freeze-up season from 3-Nov-09 to 12-Jan-10 showing a time series of: (a) air temperature, T_a (ºC), (b) water temperature, T_w (ºC), at the instrument platform, (c) water depth, h (m), mean current velocity, u (m/s), and the snow depth, d_s (cm). Also the different ice periods are labeled.

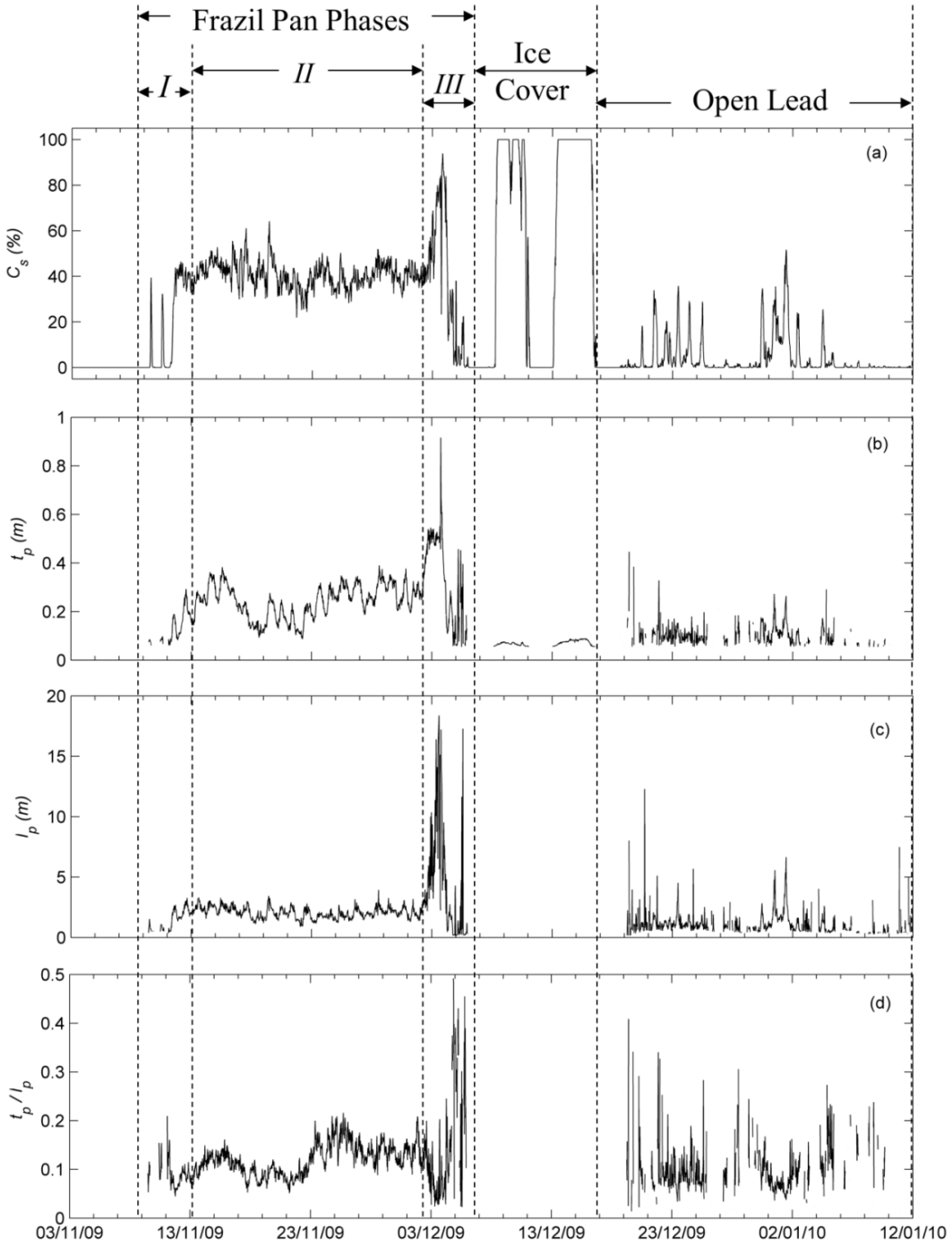

Fig. 3.10. Time series of (a) surface ice concentration, C_s (%), (b) pan drafts, t_p (m), (c) pan/raft lengths, l_p (m), and (d) the ratio of pan drafts over pan length, t_p/l_p measured at the deployment site from 03-Nov-09 to 12-Jan-10 and labeled with the different ice periods.

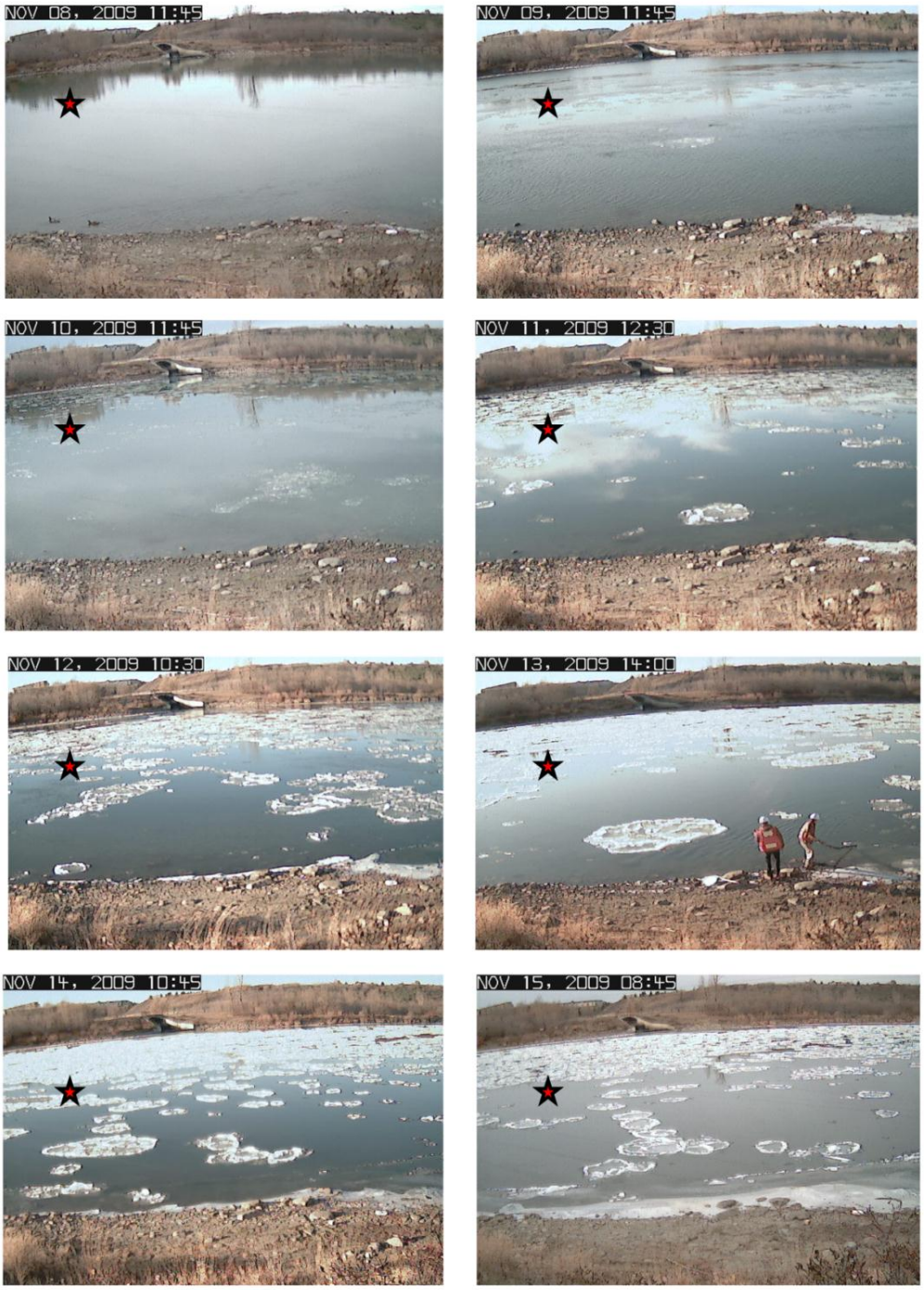

Fig. 3.11. Series of daily webcam images taken for the surface ice conditions at the deployment site from the monitoring station located on the east bank during the pan initiation period from 8-Nov-09 to 15-Nov-09. The blue star in the images shows an approximate location of the instruments' platform on the river bed.

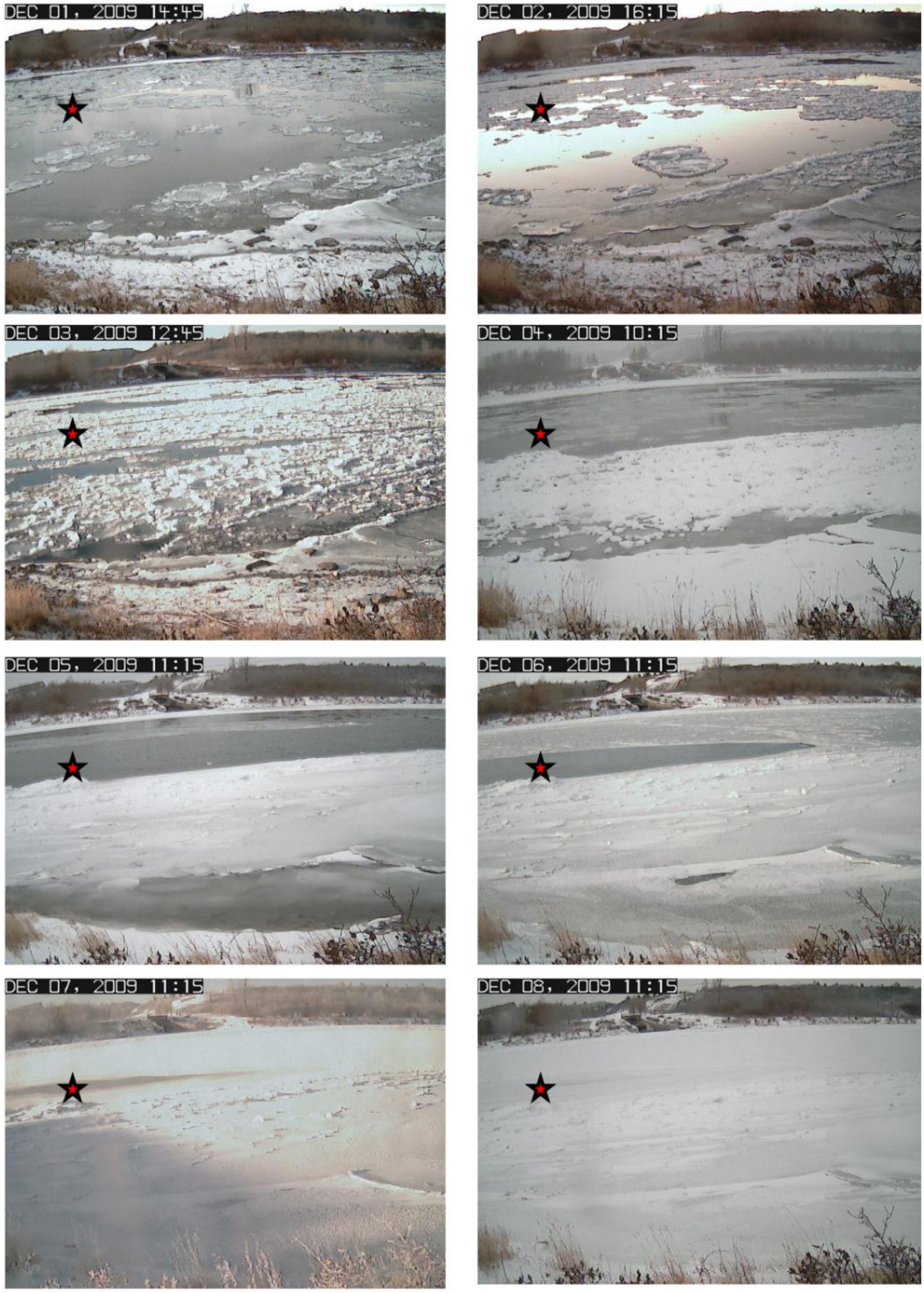

Fig. 3.12. Series of daily webcam images taken for the surface ice conditions at the deployment site from the monitoring station located on the east bank during the transition from pan period to the ice cover period from 1-Dec-09 to 8-Dec-09. The blue star in the images shows an approximate location of the instruments' platform on the river bed.

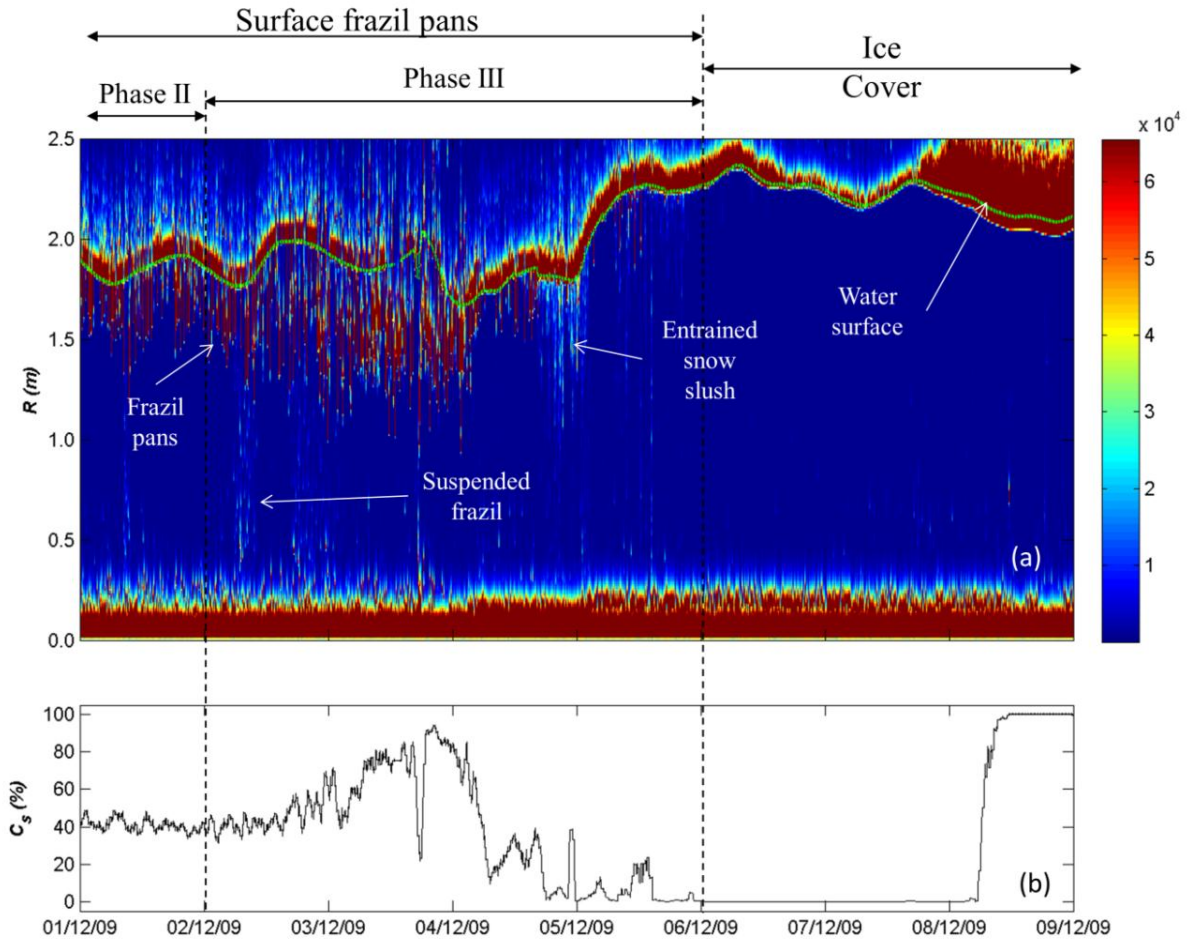

Fig. 3.13. Plot of the transition phase between the surface pan and the ice cover periods from 1-Dec-09 to 8-Dec-09 showing: (a) 2-D plot (range above transducer R (m) on y-axis, and time on x-axis) of profiles of the sonar raw count (color coded) and (b) the corresponding calculated surface ice concentration, C_s (%) labeled with the different ice phases.

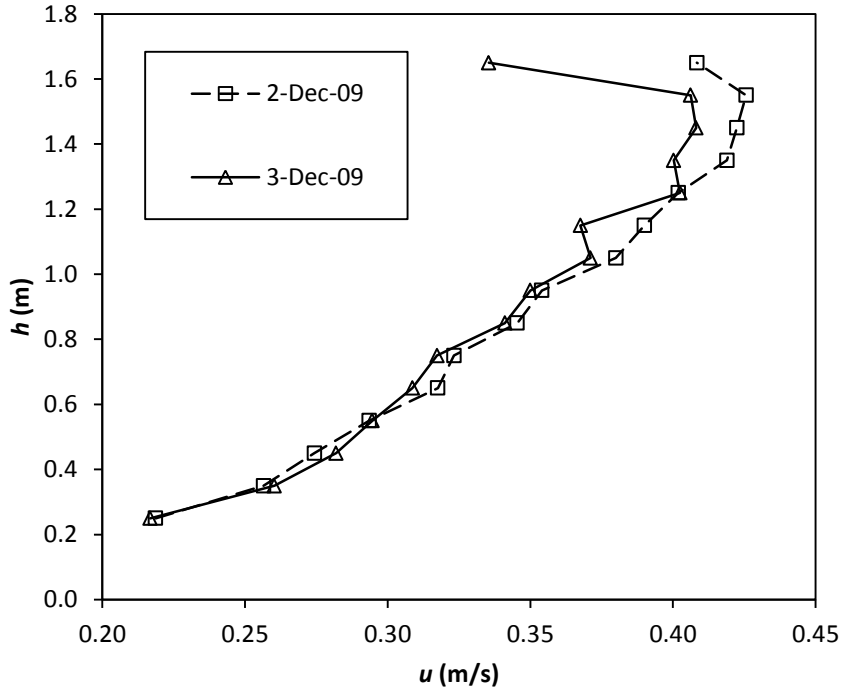

Fig. 3.14. Three-hours' time average velocity profiles from 00:00 to 03:00 on 2 and 3-Dec-09 showing velocity, *u* (m/s) versus water depth, *h* (m).

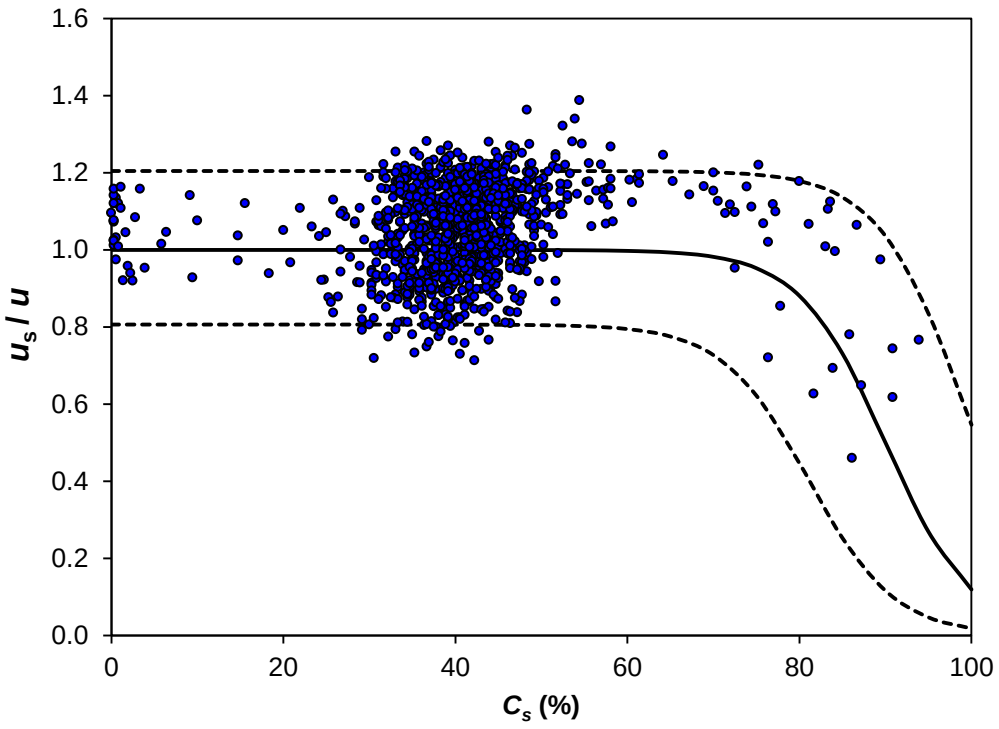

Fig. 3.15. A scatter plot of the non-dimensional ice velocity (u_i / u) versus the corresponding surface concentration, C_s (%). The two dotted lines represent an envelope for the data using Eq. (3.2).

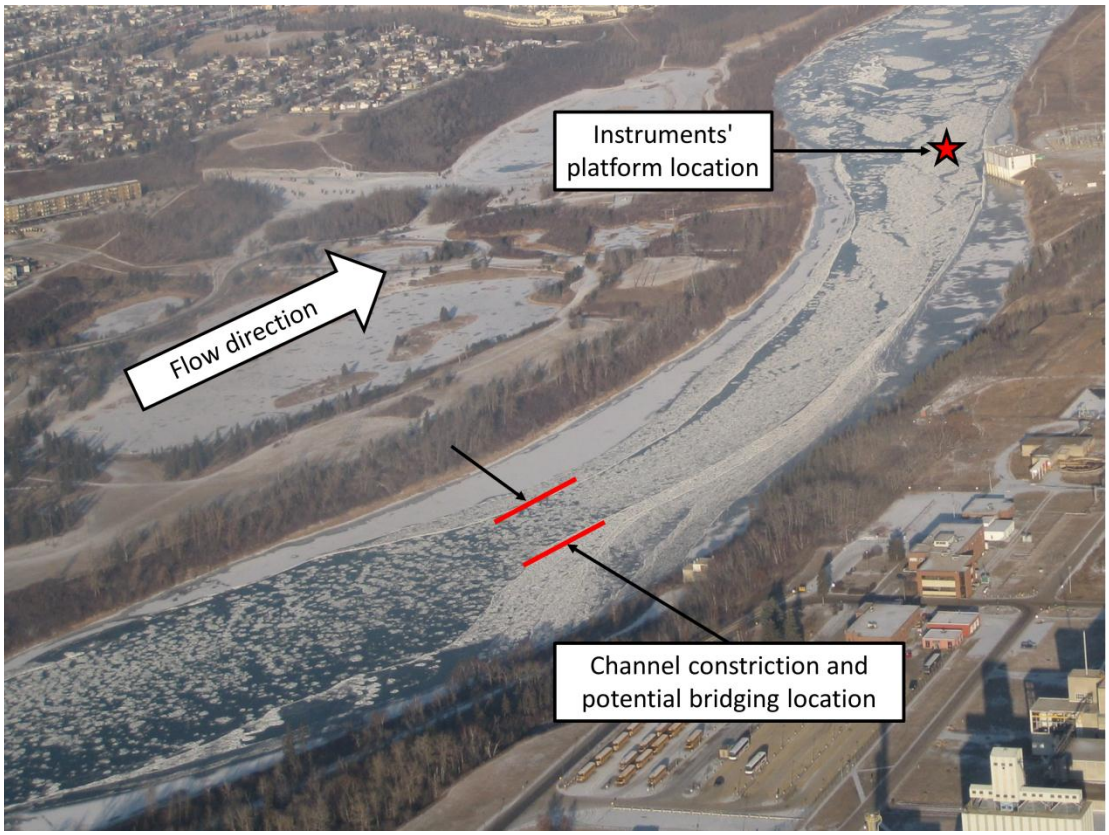

Fig. 3.16. Aerial photograph of the river ice conditions taken at 12:00 on 3-Dec-09 showing: the flow direction, the location of the instrument platform, and the channel constriction upstream of the deployment site.

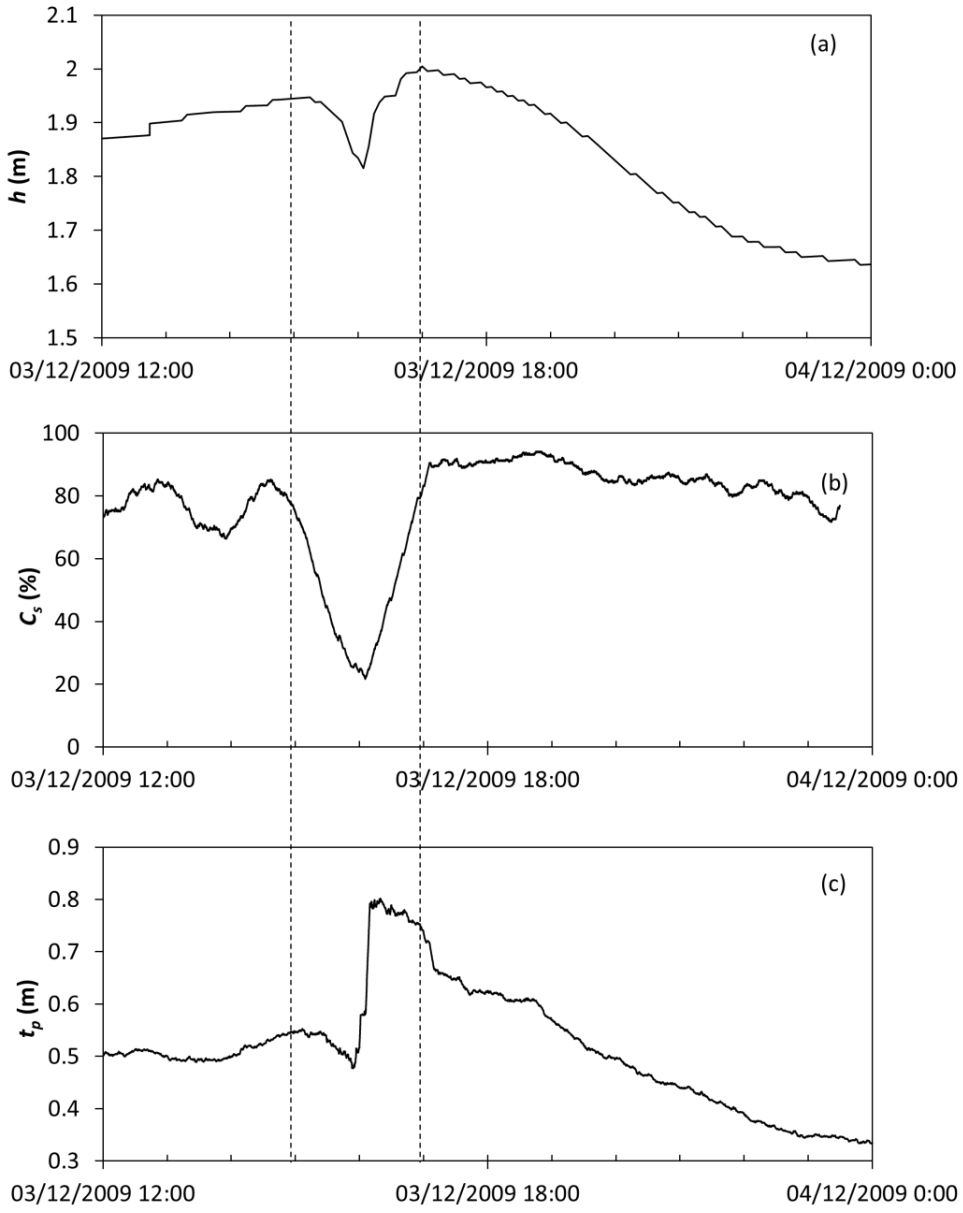

Fig. 3.17. Time series of: (a) water depth, h (m), (b) surface concentration, C_s (%), and pan draft, t_p (m), measured at the deployment site from 12:00 on 3-Dec-09 until 00:00 on 4-Dec-09. The two dotted lines highlight the effect the constriction upstream had on the measurements at the site.

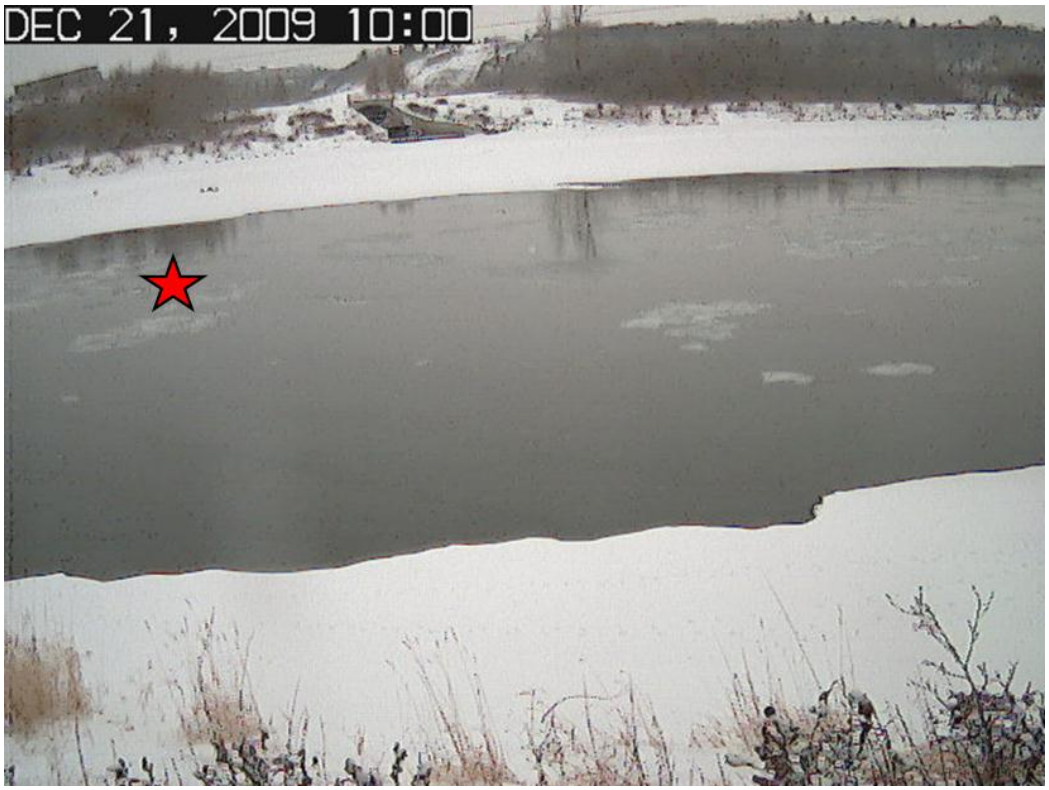

Fig. 3.18. A typical webcam image of the river surface ice conditions during the open lead period showing freshly formed submerged frazil pans. The red star shows the approximate location of the instruments platform.

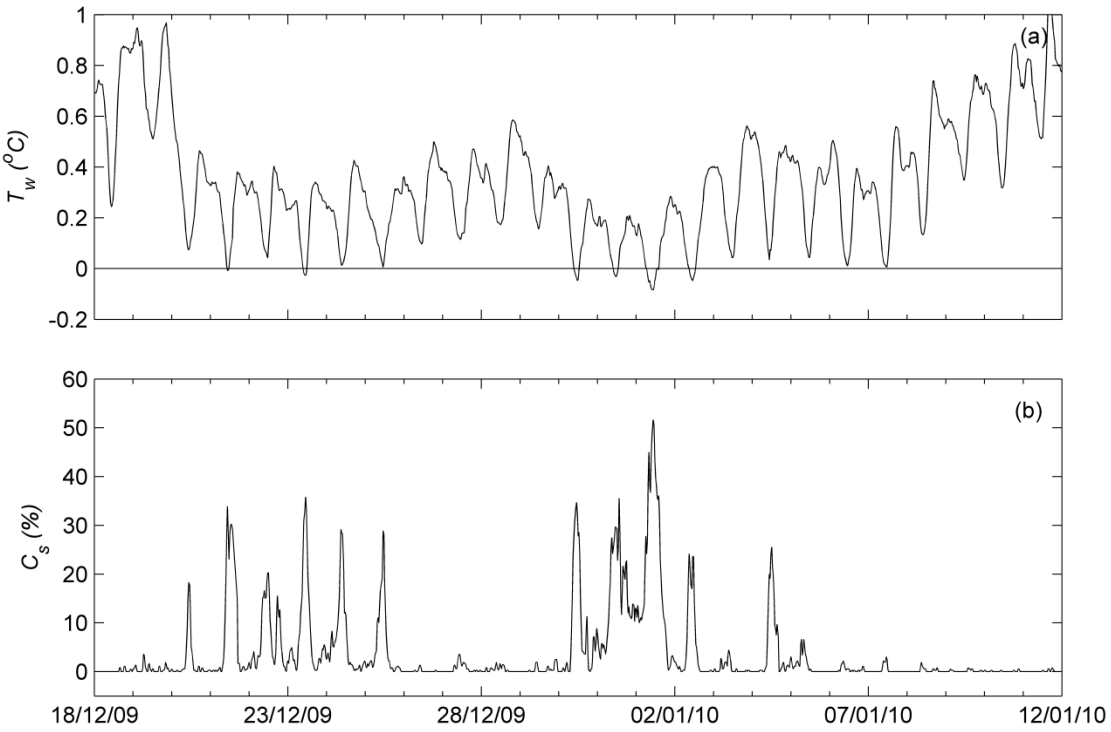

Fig. 3.19. Time series of (a) the water temperature, T_w (°C), and (b) the surface concentration, C_s (%), measured at the deployment site during the open lead period from 18-Dec-09 until 12-Jan-10.

References

Andres, D., Jasek, M., Fonstad, G., 2005. Field and Theoretical Study of the Toe Region of a Consolidated Ice Cover. . Proc. 13th Workshop on River Ice CGU-HS CRIPE, Hanover, NH.

ASL Environmental Sciences Inc., 2007. SWIPS Operators Manual. Document No. GT-100-USL53-04-R01 issued on 31-Oct-2007.

Beltaos, S., Andres, D., 2005. Hydrodynamic characteristics of waves released by ice cover consolidation and effects on ice cover stability of Peace River below Dunvegan. Proc. 13th Workshop on River Ice CGU-HS CRIPE, Hanover, NH.

Buermans, J., Fissel, D., Marko, J., Jasek, M., 2010. Progress in Shallow Water Ice Profiling Sonar (SWIPS) for River and Lake Ice Monitoring. Proceedings of 20th International Symposium on Ice, Lahti, Finland.14 p.

Calkins, D.J. and Gooch, G., 1982. Ottauquechee River - Analysis of freeze-up processes. Proceedings from the 2nd CRIPE Workshop, Edmonton, Alberta, 2-37.

Dow Ambtman, K., P. Steffler and F. Hicks, 2011. Analysis of the Stability of Floating Ice Blocks", ASCE Journal of Hydraulic Engineering, 137(4): 412-422.

Environment Canada, 2011. Climate Data and Water Survey of Canada Data - North Saskatchewan River at Edmonton (05DF001). Edmonton, AB. Website: http://www.wsc.ec.gc.ca.

Gerard, R. and Andres, D., 1982. Hydraulic roughness of freeze-up ice accumulations: North Saskatchewan River through Edmonton. Proceedings from the 2nd CRIPE Workshop, Edmonton, Alberta, 62-87.

Ghobrial, T.R., Loewen, M.R., Hicks, F.E., and Maxwell, J., 2010. Monitoring Frazil Ice Evolution during Freeze-up using the Shallow Water Ice Profiling Sonar. Proceedings of the 20th IAHR International Symposium on Ice, Lahti, Finland, June 14 to 18. 12p.

Ghobrial, T.R., Loewen, M.R., and Hicks, F.E., 2012. Laboratory calibration of upward looking sonars for measuring suspended frazil ice concentration. Cold Reg. Sci. Technol. (70): 19-31.

Hicks, F.E., 1997. An Analysis of Historical Freeze-up Data on the North Saskatchewan River below the Bighorn Dam. for TransAlta Utilities Corporation, Calgary.

Jasek, M., J.R. Marko, Fissel, D., Clarke, M., Buermans, J., Paslawski, K., 2005. Instrument for detecting freeze-up, mid-winter and break-up processes in rivers. In Proceedings of 13th Workshop on Hydraulic of Ice-Covered Rivers, Hanover, NH. 34p.

Jasek, M., and Marko, J.R., 2007. Instrument for Detecting Suspended and Surface Ice Runs in Rivers. 14th Workshop on the Hydraulics of Ice Covered Rivers, Quebec City, Canada. 30p.

Jasek, M., and Marko, J.R., 2008. Acoustic Detection and Study of Frazil Ice in a Freezing River during the 2007-2008 Winter. 19th IAHR International Symposium on Ice, Vancouver, British Columbia, Canada. 31p.

Jasek, M., Ghobrial, T.R., Loewen, M.R., Hicks, F.E., 2011. Comparison of CRISSP modeled and SWIPS measured ice concentrations on the Peace River. In Proceedings of 16th Workshop on River Ice Winnipeg, Manitoba, pp 249-273.

Kellerhals, R., Neil, C. and Bray, D., 1972. Hydraulic and Geomorphic Characteristics of Rivers in Alberta. Research Council of Alberta. Edmonton, AB, 56p .

Knuth, M.A., Shen, H.H., 2006. A computational model for the evolution of composite pancake ice. Proceedings of the 18th IAHR Symposium on River Ice, Sapporo, Japan.

Marko, J.R., Jasek, M., 2010a. Sonar detection and measurements of ice in a freezing river I: methods and data characteristics. Cold Regions Science and Technology 63, 121–134.

Marko, J.R., Jasek, M., 2010b. Sonar detection and measurement of ice in a freezing river II: observations and results on frazil ice. Cold Regions Science and Technology 63, 135–153.

Martin, S., 1981. Frazil Ice in Rivers and Oceans. Ann. Rev. Fluid Mechanics, 13:379-97.

Maxwell, J., 2012. Characterization of the Winter Regime of an Urban River. Masters of Science Thesis in Water Resources Engineering. Department of Civil and Environmental Engineering, University of Alberta, spring 2012.

Michel, B., 1984. Comparison of field data with theories on ice cover progression in large rivers. Canadian Journal of Civil Engineering, 11(4), pp. 798-814.

Morin, I., Townsend, R.D., and Morse, B. 2000. Design relations for predicting surface-ice clearing capacity of open channels. Canadian Journal of Civil Engineering, 27(6): 1230–1239.

Morse, B., Hessami, M., Bourel, C., 2003. Characteristics of ice in the St. Lawrence River. Canadian journal of Civil Engineering 30, 766–774.

Osterkamp, T. and Gosink, J. 1982. Selected Aspects of Frazil Ice Formation and Ice Cover Development in Turbulent Streams. Proc. Of 2nd Workshop on Hydraulics of River Ice, Edmonton, Alberta, Canada, June 1 and 2, 1982, pp131-147.

Osterkamp, T. and Gosink, J. 1983. Frazil Ice Formation and Ice Cover Development in Interior Alaska Streams. Journal of Cold Regions Science and Technology, v 8 p 43-56.

Richard, M. and B. Morse, 2008. Surface ice observations on the St. Lawrence River. Proceedings of the 19th IAHR International Symposium on Ice, Vancouver, Canada.

Shen, H. H., S. F. Ackley, and Y. Yuan, 2004. Limiting diameter of pancake ice. J. Geophys. Res., 109, C12035, doi: 10.1029/2003JC002123.

Shen, H. T., 2010. Mathematical modeling of river ice processes. Cold Regions Science and Technology: 62, 3‑13.

CHAPTER 4: Characterizing Suspended Frazil Ice in Rivers Using Sonars

4.1 Introduction

The first stage of ice cover formation in northern rivers is frazil ice generation. When the air temperature drops below 0°C for a significant amount of time, the water body loses heat to the atmosphere until the water becomes supercooled (i.e. cooled to slightly below 0°C). Once seed particles of ice (e.g. snow particles or frozen water droplets) are introduced into turbulent supercooled flow, large quantities of frazil ice particles are created very quickly (Daly, 2008). When present in supercooled water, frazil particles are very adhesive (active frazil); they stick to virtually any surface and to each other, forming large flocs that eventually float to the surface due to buoyancy. Typically, frazil particles are disk shaped and range in diameter from a fraction of a millimeter up to several millimeters and from 1 to 100 μm in thickness (Martin, 1981).

Frazil ice particles often cause severe problems at hydraulic structures during freeze-up in rivers. Thick slush layers may form and interfere with navigation, or block water intakes used for drinking water, manufacturing, and oil refining by accumulating over the intakes screens (Clark and Doering, 2006). Several reviews of frazil ice characteristics and mechanisms of formation are available in the literature (e.g. Martin, 1981; Tsang, 1982; Daly, 1994 and 2008). However, development of effective solutions to mitigate frazil ice problems has proven difficult because of a lack of accurate frazil ice concentration and particle sizes measurements in rivers (Daly, 1994).

Frazil ice particles' sizes and concentrations have been reported in several laboratory studies because the experimental conditions (e.g. air temperature, level of turbulence) are controlled and frazil particles are directly accessible for

measurements. Daly and Colbeck (1986) measured concentrations between 10^5 and 10^6 particles/m^3 in a refrigerated flume using a high resolution underwater camera. They reported frazil disks diameters between 0.04 and 0.50 mm having diameter to thickness ratios between 6.37 and 9.61. They also found that the particles' sizes could be fitted with a log-normal distribution with a mean diameter of ~ 0.20 mm. Ettema et al. (2003) measured volumetric frazil concentrations between 0.065% and 0.609%, collected over a conical intake placed at the center of a refrigerated flume. Ye et al. (2004) measured frazil concentration between 0.10% and 0.17% in a counter-rotating flume using a Digital Image Process System. Clark and Doering (2006) studied the characteristics of frazil particles while in suspension in the same counter-rotating flume using a Digital Image Process System, and measured particle diameters between 0.04 and 5.00 mm. They also found that the particle sizes could be fitted with a log-normal distribution, but the mean diameter was1.31 mm in their case. In addition they found that, for particle diameters between 3.0 and 3.5 mm, the diameter to thickness ratio ranged from 12.90 to 16.33. Ghobrial et al. (2012a) measured sieved mass concentrations between 0.012% and 0.135 % in a mechanically stirred frazil tank. The sieved frazil particles were disk shaped, varying in diameter between 0.25 and 4.25 mm when observed under a microscope with 10X magnification. McFarlane et al. (2012) used digital images taken with a high resolution camera to estimate frazil particles sizes while in suspension in the same frazil tank under the same experimental conditions (i.e. same mechanical stirring speed and air temperature). They found that the frazil particle size distribution in the tank could be fitted by a log-normal distribution with a mean diameter of 0.80 mm and a range of particle diameters from 0.04 mm to 5.08 mm.

Frazil particles sampled from natural rivers have generally ranged from 0.1 to 5.0 mm in diameter (Osterkamp, 1978; Osterkamp and Gosink, 1983; Wueben, 1984; Morse and Richard, 2009). However, in those field studies only a few particles were manually sampled and thus do not provide a sufficient sample size to

represent the population of particles. Rough estimates of frazil concentrations in rivers between 10^4 and 10^7 particles/m^3 have been reported using underwater photographs of frazil particles in the field (e.g. Osterkamp and Gosink, 1983). The only direct measurement of frazil ice point concentration in the field was conducted using an instrument based on water electric conductivity developed by Tsang (1985). This instrument was tested on the Beauharnois Canal, Quebec where the measured time series concentrations ranged from 0 to 0.25% (Tsang, 1984), and on the Lachine Rapids on the St. Lawrence River, Quebec, where the measured concentration profile (through the depth) ranged between 0 and 0.03% (Tsang, 1986). Unfortunately, this instrument was not built for practical continuous field deployment and need to be calibrated each time with direct measurements of frazil particles' shape and the flow velocity. A number of other methods have been developed to measure frazil ice properties (size and shape) and concentration in rivers (e.g. Lever et al., 1992; Yankielun and Gagnon, 1999; Doering and Morris, 2003). However, all of these methods have proven to be impractical for use in the field.

Recently, it have been shown that Shallow Water Ice Profiling Sonars (SWIPS) [ASL Environmental Sciences Inc., Canada], originally designed to measure ice cover thicknesses in rivers, can also detect the presence of suspended frazil ice (e.g. Marko and Jasek, 2010a and b; Morse and Richard, 2009; Richard et al., 2010). These sonars transmit acoustic pulses up through the water column and the acoustic signals reflected by the targets in the water column can be related to the size and number of the acoustic targets in the insonified volume (Urick, 1983). Researchers studying sediment transport and aquatic organisms in rivers and estuaries have been using acoustic backscatter measurements to estimate the concentration and particle sizes for more than two decades (e.g.: Greenlaw, 1979; Kristensen and Dalen, 1986; Thorne et al.,1993; Thevenot and Kraus, 1993).

Two basic approaches have been used to estimate particles sizes and concentrations from acoustic measurements. The first approach consisted of establishing regression equation between laboratory sampled concentrations and

the corresponding acoustic signal (Kristensen and Dalen, 1986). This same technique was applied to the measurement of suspended frazil ice concentrations by Ghobrial et al. (2012a). Frazil ice was generated in a specially designed laboratory frazil tank while deploying upward looking sonars to insonify the suspended frazil ice particles. A sieving technique was used to make direct measurements of frazil ice concentrations in the tank. Two upward looking sonars were used for this study, one high (546 kHz) and one low (235 kHz) frequency. Acoustic measurements of the backscattered intensity at each sonar frequency were correlated with the corresponding sampled frazil ice concentration. The resulting regression equations can then be used to estimate suspended frazil ice concentrations based on volume backscattered strength assuming that the population of frazil particles are homogeneous (i.e. have the same material characteristics), are uniform in shape, and can be represented by a dominant particle size (i.e. that the variation in the sonar signal is mainly a function of the concentration). The second approach is based on using theoretical or empirical scattering models that have been developed for different target shapes (e.g. Bowman et al., 1969) to estimate particles concentrations and sizes from the sonar data. These models are generally a function of: particle size and shape, acoustic frequency, and the ratios of density and elasticity of the particles (i.e. the frazil ice particles) to the surrounding medium (i.e. water). Most of these parameters are known or can be measured in the laboratory and therefore the backscatter sonar signal is mainly a function of the particles size and concentration. This approach was applied by Marko and Jasek (2010a, b and c) and Richard et al. (2010) to estimate frazil characteristics from sonar data sampled during freeze-up in rivers.

Marko and Jasek (2010a and b) deployed both high (546 kHz) and low (235 kHz) frequency sonars in the Peace River, Canada to monitor suspended and floating ice during freeze-up. They used Rayleigh's (1896) scattering model for small spheres to estimate particles size and concentration from the acoustic signal, sampled during suspended frazil events, by assuming a single sphere radius and estimating the corresponding concentration (referred to as '*single-frequency*'

method). Using this technique, for sphere radii ranging from 0.1 to 0.3 mm, the corresponding estimated frazil ice concentrations varied from 2.1×10^7 to 1.2×10^5 particles/m^3 (0.0088 to 0.0014 %), respectively. Marko and Jasek (2010c) used the ratio of the signal strength from the high and low frequency sonars to estimate both particle diameters and concentration (referred to as the '*two-frequency*' method) from the same field data using the Rayleigh (1896) model. They estimated sphere radii ranged between 0.12 and 0.45 mm for corresponding concentrations between 0.025 and 0.005 %, respectively.

Richard et al. (2010) deployed a 420 kHz Ice Profiling Sonar (IPS) designed for deep water use, and a 1228 kHz Acoustic Doppler Current Profiler (ADCP) in the St. Lawrence River, Canada. The sonar signals were analyzed using Johnson's (1977) scattering model for fluid spheres to estimate frazil disk radii of the 'acoustically equivalent' spheres of the same volume, assuming a diameter to thickness ratio of 15 for frazil disk particles. Using the *single-frequency* method, they estimated disk radii ranging from 0.075 to 0.180 mm for corresponding estimated frazil ice concentrations ranging from 2.8×10^7 to 5.0×10^5 particles/m^3 (0.00025 to 0.00006 %), respectively. The results for the *two-frequency* method were very similar to the single-frequency method, because the IPS returns were very weak, and therefore, its contribution was not significant in the acoustic signal (Richard et al., 2010). For their calculations, they used 2760 m/s as the speed of sound in frazil ice particles. Generally the acoustic properties (sound speed and compressibility) of suspended frazil ice particles have not been studied before.

Theoretical estimations of frazil concentrations and sizes from sonar data involve a lot of assumptions (e.g. regarding frazil particle shape and material properties, as well as sonar accuracy) and these; need to be validated with direct field sampling of frazil in rivers. Therefore, generally the laboratory sampling approach is preferable to the theoretical approaches because it yields more realistic estimates and eliminate some of the uncertainties in the calculations (Kristensen and Dalen, 1986).

The objective of this study was to assess the validity of the laboratory regression equations developed by Ghobrial et al. (2012a) and the applicability of the theoretical scattering models for quantifying frazil ice characteristics based on measured sonar data. First, using the laboratory measurements, the applicability of three scattering models (sphere, prolate spheroid and disk) for predicting suspended frazil concentrations were investigated directly. Then, using acoustic data gathered during the field deployment, the applicability of both the empirical regression equations and the theoretical scattering models were assessed indirectly.

4.2 Site Description, Instrumentation and Methods

The instrument deployment location was in northeast Edmonton, AB, Canada at EPCOR's Clover Bar power generating station (53°35'15" N; 113°22'50" W). The river at this location is ~120 m wide and has an average depth of ~1.9 m at low flow. Fig. 4.1 shows a plan view of the study site, the locations of the instrument platform, and the water depths at a mean daily discharge of 130 m^3/s at the deployment reach. The thermal regime of the river at this location is influenced by discharges from the city's Gold Bar Waste Water Treatment Plant (*WWTP*), located approximately 6 km upstream, and locally from the power plant cooling water outfall located on the east bank ~50 m upstream of the platform location (Fig. 4.1). These warm water discharges caused the local water temperature to fluctuate periodically above 0 °C; which affected the freeze-up processes observed at the site. Also discharges from the *WWTP* might have contained salts that could further depress the freezing point of water (Ashton, 1986); however, the typical effluent discharges of the *WWTP* peak at 3.5 m^3/s and the typical minimum winter flow in the North Saskatchewan River is ~100 m^3/s. Therefore, this effect (if applicable) would likely be negligible.

A high (546 kHz) and low (235 kHz) frequency sonar [ASL Environmental Sciences Inc., Canada] were deployed at the study site during the 2009/2010 freeze-up season. Both sonar units were equipped with auxiliary sensors that

measured the water temperature and the absolute pressure above the sonar transducer. The pressure data was used to estimate the water depth during the deployment period and the water temperature data were used to observe local conditions during the frazil events. A more complete description of the instruments' specifications and the settings used during the deployment can be found in Ghobrial et al. (2012a and 2012b). A 2 MHz Acoustic Doppler Current Profiler [Nortek As., Norway] was used to measure velocity profiles during the deployment. The high and the low frequency sonars, the current profiler, as well as an underwater video camera and light (used to visually monitor the instruments), were mounted on a stainless steel platform (Fig. 4.2) weighing just over 45 kg (100 lbs.). The platform consisted of a 0.9 m by 0.6 m base with a 20 cm high rail installed around the perimeter to prevent damage to the instruments should overturning occur during deployment or removal. The stainless steel was covered with plastic sheeting to prevent adhesion of suspended frazil.

On 15-Oct-09 the instrument platform was towed ~30 m from the east bank using a jet boat and placed on the river bed in ~1.9 m deep water (Fig. 4.1). Communication and power cables, approximately 100 m in length, were bundled together and laid out along the river's bed and up the river bank, leading to a small heated trailer on the top of the bank (Fig. 4.1) containing three rugged laptop computers. Each laptop was connected to one of the three instruments (i.e. the high and the low frequency sonars and the current profiler) making it possible to view the output data in real time and to ensure that the instruments were working properly for the entire duration of the deployment. A monitoring station consisting of a submerged water temperature sensor located ~10 m from the edge of water, an air temperature sensor and a webcam, was installed on the river bank on 15-Oct-09 (Fig. 4.1). Data and images from the monitoring station were sent over a wireless cell phone network to the University of Alberta web server; making it possible to visually monitor the weather and ice conditions at the site. The observation period ended on 13-Jan-10, when the monitoring station and the instrument platform were removed from the deployment site.

4.3 Data Processing

The sonar raw data from the field deployment were processed to calculate the volume backscatter strength, S_v (dB) as it can be analyzed for information about the suspended particle concentration and size distribution (Urick, 1983). The sonar transducer records the Echo Level, *EL* (dB), which is the intensity of backscattered sound at the transducer and S_v is related to *EL* by the sonar equation (Urick, 1983) as follows,

$$S_v = EL - SL + 2TL - 10\log_{10}(V_{geo}) \tag{4.1}$$

where *SL* (dB) is the source level defined as the intensity of sound emitted by the transducer, *TL* (dB) is the one way transmission loss of sound in the water, and V_{geo} is the insonified geometric volume created by the sound pulse at a specific range (m^3). A MATLAB® code was developed to process profiles of the raw sonar data to calculate the volume backscatter strength S_v (dB). A more complete description of the sonars' parameters and the signal processing algorithm can be found in Ghobrial et al. (2012a).

Backscattering of the acoustic intensity from a single target can be described by the backscatter cross section, σ_{bs} (m^2). If a single target or particle exists in the insonified volume, S_v is expressed as,

$$S_v = 10\ \log_{10}\left(\frac{\sigma_{bs}}{A_{ref}}\right) \tag{4.2}$$

where, σ_{bs} (m^2) is the acoustic backscatter cross-sectional area at a distance of 1.0 m from the target's acoustic center, and A_{ref} is a reference area (usually taken as 1 m^2) (Clay and Medwin, 1977). The backscatter cross section, σ_{bs}, is the ratio of the power reflected by the target (W) to the incident intensity, I_i (W/m^2). In real situations, the recorded backscatter intensity by the sonar is composed of contributions from many individual suspended particles, which simultaneously

contribute to the total echo level. In this case, S_v (dB) can be expressed in terms of the volume backscatter coefficient s_v (m^{-1}) as follows,

$$S_v = 10 \log_{10}(s_v R_o) \quad (4.3)$$

where R_o is a reference distance (usually 1 m), and s_v is the volume backscatter coefficient or backscattering cross sectional area per unit volume (m^{-1}) for a population of particles (Clay and Medwin, 1977). Note that s_v is the linear form of the volume backscatter strength, S_v, and can be arithmetically averaged in time or space.

In order to examine the temporal evolution of the suspended frazil events, profiles of the volume backscatter coefficient s_v (m^{-1}), were depth averaged from the minimum lookout distance of the sonar (0.5m) up to the bottom of detected floating pans or the water surface (whichever comes first) in each profile using the algorithm described in Ghobrial et al., (2012b). In addition, to decrease the noise in the data, a 30 minute's moving average was applied to the time series of the depth averaged backscatter coefficient, s_{vd} (m^{-1}). The time averaged s_{vd} (m^{-1}) were then converted to depth averaged volume backscatter strength, S_{vd} (dB) for analysis purposes.

4.4 Scattering Models

4.4.1 Background

A number of theoretical and empirical acoustic backscatter models have been developed relating the backscatter cross section, σ_{bs} of an individual particle, to its size, shape, material properties and the acoustic wavelength (e.g. Rayleigh, 1896). Such models are often obtained as a special case to the exact analytical solution for the integral of the total scattered pressure over the target volume; either by expanding the integrals using spherical harmonic series (e.g. Bowman et al., 1969), or using approximate integral techniques (e.g. Coussios, 2002). Generally most of the scattering models assume that the targets are fixed in place and rigid.

The assumption of a fixed target means that the target does not partake of the acoustic vibration of the fluid particles in which the target is embedded. The rigid target assumption means that it is non-deformable by the incident acoustic wave (Urick, 1983). Real sonar targets (e.g. frazil particles) are always movable in the fluid and non-rigid. Therefore, these theoretically idealized expressions should be viewed as no more than a crude approximation to targets of complex internal construction for which penetration and scattering around edges are suspected to occur (Urick, 1983).

Although there is no general solution to the scattering by particles of irregular shapes, assumptions have been made for $ka << 1$and $ka >> 1$; where k is the acoustic wave number = $2\pi/\lambda$, (where λ is the acoustic wave length), and a is the particle radius (Thorne and Meral, 2008). For $ka << 1$, the *Rayleigh* regime, the wavelength of the incident sound is much greater than the particle circumference. In this regime, it is anticipated that different geometrically shaped particles will behave similarly and it can be shown that the backscatter cross section, σ_{bs} is proportional to k^4. For $ka >> 1$, the *geometric* regime, the particles are much larger than the acoustic wave length, resulting in constructive and destructive interference between the incident and the backscattered acoustic waves, and in geometrical shadowing of the incident wave in the tail region of the particles (Feuillade, 2004).

It has been shown that the backscatter cross section, σ_{bs}, is a strong function of the contrast in density and elasticity between the particle and the surrounding medium in the *Rayleigh* regime, especially for fluid-like targets (Coussios, 2002). Unfortunately, little is known about the elasticity of frazil particles due to the fragility of the particles and the fact that they melt rapidly when they are removed from the supercooled water. Gold (1988) reported values for the modulus of elasticity, E ranging from 6×10^9 to 12×10^9 (Pa) for core samples of fresh water ice. Nadreau and Michel (1984) suggested that the modulus of elasticity, E, of congealed frazil ice layers (classified as S4 ice type), taken from ice cover core samples, can be expressed as a function of the ice temperature as follow,

$$E = 6.1(1 - 0.006T_i) \tag{4.4}$$

where, E is the modulus of elasticity ($\times 10^9$ Pa) and T_i is the ice temperature (°C). For $T_i \approx 0$ °C (assumed to be the temperature of freshly formed suspended frazil particles in supercooled water), Eq. (4.4) gives a value of $E = 6.1\times 10^9$ Pa, which agrees with the lower limit of Gold's (1988) measurements. Since there are no reported values for the modulus of elasticity of suspended frazil particles, a value of $E = 6\times 10^9$ Pa was used in this study. The sound speed in frazil ice particles, c_i, can then be estimated using the following equation,

$$c_i = \sqrt{\frac{E}{\rho_i}} \tag{4.5}$$

where ρ_i (kg/m^3) is the density of frazil ice (Clay and Medwin, 1977). Assuming $\rho_i \approx 920$ kg/m^3 Eq. (4.5) predicts that, $c_i = 2554$ m/s.

Most of the scattering models were developed for specific types of materials of insonified targets. The targets are classified according to the ratio of the density, R_ρ, and the ratio of the sound speed, R_c, of the target to the surrounding medium. The three types of targets are; fluid (R_ρ and $R_c \approx 1$), elastic (R_ρ and $R_c \approx 3$ to 4) and rigid (R_ρ and $R_c \rightarrow \infty$) (Stanton, 1989). In the case of frazil ice particles suspended in rivers, the medium is always fresh water close to 0°C ($\rho_w = 1000$ kg/m^3 , $E_w = 2\times 10^9$ Pa, and $c_w = 1403$ m/s), and therefore, $R_\rho = 0.92$, and using c_i of 2554 m/s, the corresponding $R_c = 1.82$. Accordingly, it was concluded that the best approximation, given these values of R_ρ and R_c, was to model the frazil ice particles as fluid targets.

In the next section, a review of three scattering models for fluid targets of different geometric shapes: sphere, prolate spheroid and disk, is provided. In Fig. 4.3 the basic geometry and the different dimensions used by the scattering models for each shape are illustrated. The sphere model was chosen because it has been widely used for modeling scattering from suspended sediments (e.g. Thorne et.

al., 1993), marine organisms (e.g. Greenlaw, 1979), as well as suspended frazil ice (Richard et al., 2010). The prolate spheroid and the disk models were chosen because they may be more realistic approximations to the geometric shape of frazil ice particles.

4.4.2 Sphere Model

Scattering by an "*ideal*" spherically shaped target was first investigated by Lord Rayleigh (1896). The basic assumption for his theoretical derivation was that the particle size is always much smaller than the incident wave length, or that ka <<1. This assumption allows diffraction of the acoustic waves around individual particles. In this case, the backscatter cross section, σ_{bs} (m^2) can be written as (Medwin and Clay, 1998),

$$\sigma_{bs} = 4\pi a^2 (ka)^4 \left[\left(\frac{1 - R_\rho R_c^{\,2}}{3R_\rho R_c^{\,2}} + \frac{1 - R_\rho}{1 + 2R_\rho} \right)^2 \right] \tag{4.6}$$

Note that in Eq. (4.6), the parameters in the square bracket are constant; therefore the backscatter cross section is directly proportional to k^4 and a^6. Anderson (1950) derived an exact analytical solution to the scattering by an ideal fluid sphere of diameters up to several wave lengths; which expands to cover the *Rayleigh* regime as well as the *geometric* regime, and is given by,

$$\sigma_{bs} = 4\pi a^2 \frac{\left| \sum_{m=0}^{M-1} \frac{(-1)^m (2m+1)}{1 + iC_m} \right|^2}{(ka)^2} \tag{4.7}$$

where m is the mode number, M is the number of modes needed to obtain acceptable results, and C_m is defined by,

$$C_m = \frac{\left(\frac{\alpha_m(k'a)}{\alpha_m(k'a)}\right)\left(\frac{n_m(ka)}{j_m(k'a)}\right) - \left(\frac{\beta_m(ka)}{\alpha_m(ka)}\right) R_\rho R_c}{\left(\frac{\alpha_m(k'a)}{\alpha_m(k'a)}\right)\left(\frac{j_m(ka)}{j_m(k'a)}\right) - R_\rho R_c} \tag{4.8}$$

where the wave number inside the particle $k' = k / R_c$, j_m and n_m are the spherical Bessel and spherical Neumann functions, respectively of order m, and α_m and β_m are defined as follows,

$$\begin{aligned} \alpha_m(ka) &= m j_{m-1}(ka) - (m+1) j_{m+1}(ka), \\ \alpha_m(k'a) &= m j_{m-1}(k'a) - (m+1) j_{m+1}(k'a), \\ \beta_m(ka) &= m n_{m-1}(ka) - (m+1) n_{m+1}(ka) \end{aligned} \tag{4.9}$$

It can be shown that when $M \geq ka+3$, the sum is approximately the same as for an infinite number of modes (Medwin and Clay, 1998). In the low frequency region, $ka << 1$, the Anderson solution is exactly the same as that derived by Rayleigh. In the high frequency regime, $ka >> 1$, the geometrical scattering region, the backscatter cross section is a complex function of the frequency with many peaks and troughs which are caused by constructive and destructive interference of the incident and diffracted waves by the sphere (Feuillade and Clay, 1999; Feuillade, 2004).

Johnson (1977) was able to construct a "*high-pass*" model that follows the Rayleigh scattering at $ka << 1$, and at $ka >> 1$, the model has an asymptotic value that is consistent with the peaks of Anderson's (1950) model, when applied to real fluid targets. The combination of Rayleigh scatter and geometrical scatter operate as if the particle is a high pass filter with cutoff of $ka \approx 1$ (Medwin and Clay, 1998). Johnson's model does not require the computation of spherical Bessel or Neumann functions and is given by,

$$\sigma_{bs} = 4\pi a^2 \left[\frac{2(ka)^4}{2+3(ka)^4} \right] \left[\left(\frac{1-R_\rho R_c^{\,2}}{3R_\rho R_c^{\,2}} + \frac{1-R_\rho}{1+2R_\rho} \right)^2 \right] \tag{4.10}$$

Fig. 4.4 presents plots of the non-dimensional backscatter cross section σ_{bs} / πa^2 versus the corresponding *ka* calculated using the Rayleigh (1896), Anderson (1950), and Johnson (1977) models for real fluid targets (R_ρ = 1.016, and R_c = 1.033) and frazil ice targets (R_ρ = 0.92, and R_c = 1.82). As shown in Fig. 4b, when the Johnson model is applied to frazil ice targets the predicted curve does not follow the peaks of Anderson's model exactly. However, the *high pass* model did reach an asymptotic limit at *ka* >1 that is still in a good agreement with Anderson's peaks. The main advantage of Johnson's model is that the equations are much simpler to evaluate compared to Anderson's model but the main disadvantage is that is does not describe the modal interferences at *ka* >>1 (the *geometric* regime). It is well known that ice targets in water are not "ideal" spheres; therefore, applying an exact analytical solution (i.e. Anderson, 1950) would at best be an *approximation* to the real case. In addition, when sound is scattered by a population of particles, the modal interferences that occur at individual particles will be negligible and the total scattering strength will resemble a smoothed version of the exact modal solution such as Johnson's *high-pass* model (Stanton, 1989). For these reasons, Johnson's (1977) model was used as the *sphere* model in this study.

4.4.3 Prolate Spheroid Model

Stanton (1989) extended Johnson's (1977) approach to develop a generalized high pass model that can be applied to fluid, elastic and rigid materials. Stanton's model can be applied to idealized shaped targets (e.g. spheres, prolate spheroids, and cylinders) and non-idealized targets (irregular shapes) by inserting empirical shape factors that compensate for the effect of the shape irregularity; these can be determined numerically or experimentally. When applied to an ideal sphere, Stanton's general solution yields exactly the same expression proposed by

Johnson (1977). In this study, the model proposed by Stanton (1989) for an ideal prolate spheroid was adopted because it was assumed to be a more realistic approximation to the scattering by frazil particles or flocs, than an ideal sphere; especially as most of the suspended frazil particles photographed at varying angles in the laboratory, appeared as ellipses (Clark and Doering, 2006; McFarlane et al., 2012). As shown in Fig. 4.3, the model was developed to calculate the backscatter cross section when the incident acoustic wave is normal to the major axis of the prolate spheroid and is expressed as follows,

$$\sigma_{bs} = \frac{16}{9}\pi b^2 \left[\frac{(ka)^4 \alpha_\pi^2 G}{1 + \left[\frac{16}{9}(ka)^4 \alpha_\pi^2 \right] \Big/ (R_e^2 F)} \right] \tag{4.11}$$

where, a and b are the lengths of the semi minor and semi major axes of the prolate spheroid (see Fig. 4.3), F and G are empirical functions that account for any deviation in shape from an "*ideal*" prolate spheroid (in this study, F and G were assumed =1); α_π is a coefficient computed for backward scattering and is defined as,

$$\alpha_\pi = \left(\frac{1 - R_\rho R_c^{\,2}}{2 R_\rho R_c^{\,2}} + \frac{1 - R_\rho}{1 + R_\rho} \right) \tag{4.12}$$

R_e is the reflection coefficient defined as,

$$R_e = \left(\frac{R_\rho R_c - 1}{R_\rho R_c + 1} \right) \tag{4.13}$$

The ratio of semi major axis, b to the semi minor axis, a of the prolate spheroid was assumed to be analogous to the frazil disk diameter to thickness ratio. A ratio of 10 for b / a was adopted for the calculations of the backscatter cross section using the prolate spheroid model. This ratio for typical frazil disk particles is an average value between the ratios of ~ 6 to 9 reported by Daly and Colbeck (1986)

and ~ 12 to 16 reported by Clark and Doering (2006). The non-dimensional backscatter cross section of the prolate spheroid, expressed as σ_{bs} / πb^2, and computed using Stanton's (1989) model, is plotted versus *ka* in Fig. 4.5a using the material properties estimated for frazil ice particles (R_ρ = 0.92, and R_c = 1.82). Comparing Figs. 4.5a and 4.4b, it can be seen that the prolate spheroid model behaves very similarly to Johnson's sphere model, but with a slightly lower asymptotic limit of 0.05 for the non-dimensional backscatter cross section at *ka* >1, compared to a value of 0.10 for the sphere model.

4.4.4 Disk Model

Most of frazil particles observed in the laboratory and sampled from the field are disk shaped and ranged in diameter from ~0.05 to ~6.00 mm (e.g. Clark and Doering, 2006; Daly, 1994; Ghobrial et al., 2012a, McFarlane et al., 2012). Therefore, a scattering model developed for disk shaped particles to estimate the backscatter cross section of frazil ice particles would potentially be the most accurate. There is no exact solution available for scattering of sound by a fluid disk of non-zero thickness (Coussios, 2002). Solutions of backscatter cross section for disks of zero thickness are available (Bowman et al., 1969) but these solutions are not applicable to real sonar targets because infinitesimally thin particles will have no compressibility and, therefore, the backscatter cross section will not be a function of the particle's material properties. Recently, Coussios (2002) used approximate integral techniques (referred to as the 'Born approximation') to solve the scattering field (in all directions) by fluid disks of non-zero thickness. The Born approximation assumes that the scattered wave intensity is much smaller than that of the incident wave, so that the total scattering field within the scattering region can be approximated by the incident field only. This assumption is valid only for fluid-like targets (R_ρ and $R_c \approx 1$), which most of the incident waves are expected to penetrate. Coussios (2002) showed that the resulting model is accurate up to $ka \approx 1$, above which the model show increasing errors. It is expressed as follows,

$$\sigma_{bs} = k^4 a^4 \frac{t^2}{4} \left| \left[\frac{J_1(a\sqrt{m_1^2 + m_2^2})}{a\sqrt{m_1^2 + m_2^2}} \right] \frac{\sin(m_3 \frac{t}{2})}{m_3 \frac{t}{2}} \left[\gamma_k + \gamma_\rho \cos\theta \right] \right|^2 \tag{4.14}$$

where, a is the disk radius (m), t is the disk thickness (m), J_1 is the Bessel function of the first kind and order of one,

$$\gamma_k = \frac{k_i - k_w}{k_w}, \quad \gamma_\rho = \frac{\rho_i - \rho_w}{\rho_i}, \tag{4.15}$$

where, γ_k and γ_ρ are the normalized compressibility and density contrast between the particle material (ice) and the surrounding fluid (water), $k_i = 1 / E_i$, (Pa^{-1}) and $k_w = 1 / E_w$ (Pa^{-1}) are the compressibility of ice and water, respectively,

$$m_1^2 + m_2^2 = k^2[\sin^2\theta_i + \sin^2\theta_o - 2\sin\theta_i \sin\theta_o \times \cos(\phi_i - \phi_i)],$$

$$m_3 = k(\cos\theta_i - \cos\theta_o), \tag{4.16}$$

$$\cos\theta = \sin\theta_i \sin\theta_o \cos(\phi_i - \phi_i) + \cos\theta_i \cos\theta_o,$$

where, θ_i (degree) is the angle between the normal axis (z-axis) and the incident sound wave, θ_o (degree) is the angle between the normal axis (z-axis) and the reflected sound at the observer (receiver), ϕ_i and ϕ_o (degree) are the projections of θ_i and θ_o, respectively in the disk (x-y) plane (see Fig. 4.3).

For the calculations of σ_{bs}, a value of 10 was also used for the disk diameter to thickness ratio, which corresponds to a ratio of a / t = 5. The normalized backscatter cross section $\sigma_{bs} / \pi a^2$ for frazil ice disk particles estimated using Eq. (4.14), is plotted versus ka in Fig. 4.5b. Comparing Fig. 4.5b with Figs. 4.4b and 4.5a, it can be noticed that, for the same non-dimensional backscatter cross section, the disk model predicts larger particles sizes than the sphere or the prolate

spheroid models. Coussios's (2002) disk model is very similar to Anderson's (1950) solution as it provides a general solution that solves for both the *Rayleigh* regime and the constructive and destructive interferences in the *geometric* regime (Fig. 4.5b). It was found that, in the Rayleigh regime, disk particles are proportional to k^4 and are independent of the angle of incidence (Coussios, 2002). In the *geometric* regime, different angles of incidence of the acoustic waves only shift the peaks and troughs of the modal interferences to a slightly higher or lower *ka*. Also it is shown in Fig. 4.5b that the peaks of the model decrease sharply starting at $ka \approx 10$ and the model does not appear to approach an asymptotic limit in the geometric regime ($ka >> 1$). This might be due to the fact that the mathematical approximation used to develop the model (i.e. the Born approximation) yields to accurate results for $ka \leq 1$. A more detailed sensitivity analysis of the behavior of the disk model to various input parameters can be found in Coussios (2002).

4.4.5 Estimation of Concentration and Particle Size Using Scattering Models

Based on the assumption that the particles are randomly distributed in space, the scattering cross sections of individual particles are simply summed (Clay and Medwin, 1977). Therefore, s_v (m^{-1}) at a specific range above the transducer can then be expressed as,

$$s_v = \sum_i \left(N_{vi} \sigma_{bs_i} \right) \tag{4.17}$$

where N_{vi} is the number of the ith size of particles per unit volume (m^{-3}) having a backscatter cross section of σ_{bsi} (m^2). Typically s_v is calculated from the sonar measurements and, if the particles are of known sizes and characteristics, σ_{bs} can be estimated using any of the scattering models described above and the number of particles in the insonified volume N_v (m^{-3}) can be calculated from Eq. (4.17). The volume of individual particles of size i, V_{pi} (m^3), can be estimated for each

geometric shape (see Fig. 4.3), and the particles' concentration can then be calculated as follows,

$$C = \frac{\left(N_{vi} V_{pi}\right)}{V_{tot}} \times 100 \tag{4.18}$$

where, C is the frazil concentration (%), and V_{tot} is the total volume (m^3). In this study, V_{tot} was taken as 1 m^3 to estimate the concentration per unit volume. There are two unknowns in the acoustic measurements: the particles size and concentration. In the *single-frequency* method, one unknown must be assumed for the other to be deduced. In the *two-frequency* method, sonar measurements are made at two acoustic frequencies and the set of equations can be solved simultaneously to solve for both unknowns (Greenlaw, 1979). If measurements are made at more than two acoustic frequencies, Eq. (4.17) can be written in matrix form to solve for a distribution of particles; this is the *multi-frequency* method (Greenlaw, 1979). In this study, sonar measurements were made at two frequencies (546 kHz and 235 kHz); therefore, both the *single-frequency* and the *two-frequency* methods could be applied.

Single-frequency acoustical estimates are widely used for aquatic organism assessment as they provide consistent and sufficiently accurate concentration estimates. The main assumptions of the *single-frequency* method are that a single, known particle size dominates the acoustic scattering and that shadowing effects are negligible (Holliday and Pieper, 1995). The average size of aquatic organisms can be estimated from laboratory experiments, field sampling or numerical models and therefore it is common practice to assume a mean organism size and then their concentration can be computed using Eqs. (4.17) and (4.18) (Holliday and Pieper, 1995). The disadvantage of this method is that it is difficult to differentiate between changes in concentration and particle size distribution (Gartner, 2004). Thus, a change in the size distribution could be misinterpreted as a change in concentration. In this study, the *single-frequency* method was used to assess the validity of the scattering models for frazil ice particles using the

laboratory data because direct measurements of frazil concentrations and particles size distribution were available (Ghobrial et al., 2012a; McFarlane et al., 2012).

The *two-frequency* method was first proposed by Greenlaw (1979) based on Johnson's (1977) simplified sphere model. If it can be assumed that a single particle size dominates the acoustic scattering, then the volume backscatter coefficient, s_v, is proportional to the backscatter cross section, σ_{bs} [see Eq. (4.17)]. In this case the ratio of the volume backscatter coefficients is equal to the ratio of the backscatter cross sections at the two frequencies (i.e. $s_{v1}/s_{v2}=\sigma_{bs1}/\sigma_{bs2}$ where indices 1 and 2 denote the high and low frequencies, respectively). Measurements of the ratio s_{v1}/s_{v2} can then be used to provide estimates of a single particle size, using theoretical predictions of $\sigma_{bs1}/\sigma_{bs2}$. The dominant radius, $\bar{a}$, predicted using Johnson's (1977) sphere model, can be determined using Eqs. (4.10) and (4.17) and the resulting equation is,

$$\bar{a} = \left| \frac{2}{3k_1^4} \frac{(k_r^4 - \sigma_r)}{(\sigma_r - 1)} \right|^{0.25} \tag{4.19}$$

where, $k_r = k_1 / k_2$ and $\sigma_r = \sigma_{bs1} / \sigma_{bs2}$ are the ratios of the wave numbers and the backscatter cross-section, respectively (Greenlaw, 1979). This same concept can be applied to Stanton's (1989) simplified prolate spheroid model using Eqs. (4.11) and (4.17), and the dominant semi minor axis, $\bar{a}$ is given by,

$$\bar{a} = \left| \frac{9}{16\alpha_\pi^2} \left(\frac{k_r}{k_1} \right)^4 \frac{\left(1 - \frac{\sigma_r}{k_r^4} \right)}{(\sigma_r - 1)} \right|^{0.25} \tag{4.20}$$

Fig. 4.6 presents a plot of σ_r versus the sphere radius or prolate spheroid semi minor axis, $\bar{a}$ (mm) predicted using Eqs. (4.19) and (4.20), for acoustic frequencies of 546 kHz and 235 kHz. In Fig. 4.6, at $\bar{a}$ < 0.2 (mm), σ_r is proportional to k_r^4 and approaches an asymptotic limit of 29.1 (i.e. the Rayleigh

regime) for both the sphere and the prolate spheroid models. As $\bar{a}$ increases, σ_r decreases and both models predict an asymptotic limit of 1.0 at $\bar{a}$ > 1.0 (mm) (i.e. the geometric regime). Two main conditions must be met for this technique to be valid: (1) σ_r must always be between the two asymptotic limits (i.e $1.0 \leq \sigma_r \leq 29.1$); and (2) the distribution of particles contributing to the acoustic scattering must span over the transition from the Rayleigh regime to the geometric regime (i.e. the distribution of $\bar{a}$ must cover sizes from less than 0.2 mm to larger than 1.0 mm) (Holliday and Pieper, 1995). If any of these conditions are violated, predicting the size and the concentration using this method will result in non-realistic values (Holliday and Pieper, 1995). Another disadvantage of this method is that it cannot be applied to general solutions (i.e. Anderson, 1950; Coussios, 2002) with complex series functions (e.g. Bessel or Neumann functions) because separation of variables is impossible for these functions (Powers, 2006). For suspended frazil sonar data gathered from the laboratory and the field using the 546 kHz and the 235 kHz sonars, σ_r was often above the asymptotic limit of 29.1; therefore, the *two-frequency* method was not valid for concentration and size prediction.

4.5 Applicability of Scattering Models to Laboratory Results

A series of laboratory experiments, reported by Ghobrial et al. (2012a), were conducted to correlate the backscatter acoustic intensity with frazil ice concentration. Frazil was generated using mechanical stirring to produce turbulence in a specially designed frazil tank located in the cold room facility at the University of Alberta. The high (546 kHz) and the low (235 kHz) frequency sonars were deployed on the bottom of the tank and used to insonify the suspended frazil ice particles. The stirring was stopped once the concentration of frazil reached a certain level in the tank, then frazil particles were sieved vertically and the mass concentration was calculated. The depth average volume backscatter strength, S_{vd} (dB) at the moment the frazil was sampled using the sieve was correlated to the corresponding frazil concentration, C (%). The resulting regression equations for the high and low frequency sonars, respectively, are

$$C = 10^{(-8.015+0.048*RB)} \quad (4.21)$$

and

$$C = 10^{(-9.363+0.066*RB)} \quad (4.22)$$

where, RB (dB) is the relative backscatter given by,

$$RB = SL + 10\log_{10}(V_{geo}) + S_v \quad (4.23)$$

where, SL is the transducer source level (dB) and V_{geo} (m^3) is the insonified geometric volume at a specific range above the transducer (Thevenot et al., 1992). During these experiments, measured mass concentrations ranged from 0.012% to 0.135% (Ghobrial et al., 2012a). McFarlane et al. (2012) found that the frazil particle size distribution in the tank (using the same air temperature and level of mechanical stirring) could be fitted by a log-normal distribution with a mean diameter of 0.80 mm and a range of particle diameters from 0.04 mm to 5.08 mm. They also observed that the shape of the size distribution is almost constant during the course of an experiment (i.e. mean particle sizes do not change significantly with the increase of frazil concentration in the tank).

In order to assess the applicability of the scattering models to these laboratory results, the *single-frequency* method was used. The sphere (Johnson, 1977), prolate spheroid (Stanton, 1989), and disk (Coussios, 2002) models were used to estimate the backscatter cross section, σ_{bs} (m^2) for assumed frazil particle sizes. The predicted σ_{bs} and the measured depth average backscatter coefficient s_{vd} (m^{-1}) could then be used with Eq. (4.17) and (4.18) simultaneously, to estimate frazil ice concentration, C (%). Three particle sizes were assumed for each scattering model so that the resulting predicted concentrations from the model varied over a range that represent a lower envelope, a mean value, and a higher envelope to the concentrations estimated using the laboratory correlation equations and the experimental data points (i.e. the actual sieve concentration measured at the end

of each experiment). Results from this analysis are illustrated in Fig. 4.7 that shows plots of concentration, C (%) versus the depth average volume backscatter strength, S_{vd} (dB). The experimental data points, the laboratory regression equations, and the estimated concentrations from three particles sizes for different scattering models are also presented.

It is evident from Fig. 4.7 that the estimated concentrations from the scattering models support the general trend of the laboratory measured concentrations. That is, they all increase at approximately the same rate as S_{vd} increases. This implies that the laboratory data can in fact be modeled using these scattering models. Fig. 4.7 also shows that a relatively narrow range of particle sizes was needed to envelope approximately all the laboratory measurement points. The exceptions were the points corresponding to concentrations, $C < 0.025\%$ and $S_{vd} < -40$ (dB) for the high frequency sonar; which might be because the sieving technique was not as sensitive as the high frequency sonar to concentrations below this value (Ghobrial et al., 2012a).

Comparing the low frequency results (Figs. 4.7a, c, and e) with the high frequency results (Figs. 4.7b, d, and f), it can be seen that, in general, the range of particle sizes that envelope the high frequency data is slightly wider and of larger size than the range that envelopes the low frequency data. For example, looking at the disk model in plots 4.7e and 4.7f, the envelope of particle sizes for the low frequency sonar ranged from 0.15 mm to 0.25 mm compared to 0.21 mm to 0.35 mm for the high frequency sonar. This difference might be because the high frequency sonar is more sensitive to smaller particles and can detect more suspended frazil particles due to its shorter wave length than the low frequency sonar. As a result, a weaker backscattering intensity was measured with the low frequency sonar for the same frazil concentrations which resulted in a lower S_{vd} (dB) range for the low frequency experimental data. Lower S_{vd} means lower estimated concentrations from the laboratory equations and consequently requires smaller particle sizes to envelope the laboratory data.

The fact that a narrow range of particle sizes was able to envelope approximately all the laboratory measurement points in Fig. 4.7, means that the population of frazil ice in the laboratory can be represented by a single dominant size. These representative sizes can be estimated by averaging the envelope limits of the high and the low frequency data for each scattering model (see Fig. 4.7) and were found to be equal to a radius of 0.058 mm for the sphere model (Fig. 4.7a and 4.7b), a semi major axis of 0.27 mm for the prolate spheroid model (Fig. 4.7c and 4.7d), and a radius of 0.25 mm for the disk model (see Fig. 4.7e and 4.7f).

The particle sizes estimated for the prolate spheroid and the disk models were very close to each other and in a better agreement with the average disk radius of 0.40 mm observed in the laboratory (McFarlane et al., 2012) than the size estimated using the sphere model. Therefore, the sphere model was excluded from further consideration. Since the disk model is a better approximation to the actual shape of frazil ice particles, it was chosen over the prolate spheroid for predicting frazil concentration from the field data. This application is discussed next.

4.6 Field Results

4.6.1 Synopsis of Frazil Events and Sonar Results

Time series of the air temperature, T_a (°C), and the water temperature, T_w (°C), from 3-Nov-09 to 12-Jan-10 are plotted in Fig. 4.8. Detected suspended frazil events and three time periods dependent on the surface ice conditions (i.e. frazil pans, complete ice cover, or open lead), are labeled in Fig. 4.8. The water temperature decreased gradually from 3-Nov-09 and the first supercooling was observed on 12-Nov-09 (Fig. 4.8). As a result, frazil ice started to form upstream and frazil pans were continuously observed at the site form 13-Nov-09 until 5-Dec-09. On 14-Nov-09, two successive suspended frazil events were detected at 06:45 and at 19:15, each with an approximate duration of ~4:00 hrs. During these two events, the water was supercooled to approximately -0.08°C and the air temperature was between -2 and -5°C. Warmer air temperatures for the next week, combined with warm water discharges from the city *WWTP*, resulted in

above zero water temperatures and, consequently, no frazil events were observed during this week. As the daily air temperatures started to decrease again, reaching an average below 0°C on 21-Nov-09, the water temperature supercooled occasionally until it stayed below 0°C from 23-Nov-09 until 1-Dec-09. During this time period, three frazil events were detected on 25-Nov-09, 28-Nov-09, and 1-Dec-09. These three events were very similar; they all occurred in the morning hours (between 05:00 and 08:00) and were two to three hours in duration. Starting on 1-Dec-09, air temperatures decreased gradually and reached -15˚C on 4-Dec-09. During this period, the water was continuously supercooled to approximately -0.09 °C and two frazil events were detected on 2-Dec-09. The first started at 05:00 and lasted ~6 hours, and the second started at 16:00 and lasted for ~11 hours.

Colder air temperatures resulted in a significant increase in surface ice concentrations; approaching 80 to 90%, by 4-Dec-2009 and the ice front progressed upstream past the study site on 6-Dec-09. The air temperature was between -20 and -30 °C from 6-Dec-09 to 16-Dec-09 and a solid ice cover was present at the site during this time period (Fig. 4.8). Generally, the presence of an ice cover at the water surface will reduce the heat loss rate to the atmosphere, preventing the supercooling of water and the generation of suspended frazil (Daly, 2008). As a result, no frazil events were detected by the sonars during the ice cover period. Starting from 16-Dec-09, warmer air temperatures combined with warm water outflows from the Gold Bar *WWTP* caused the water temperature at the site to be consistently above 0°C, initiating an open lead that started at the *WWTP* outfalls ~ 6 km upstream and progressing downstream to the study site by 17-Dec-09. This open lead persisted above the transducers until 13-Jan-10, the day the instruments were retrieved. Despite the cold air temperatures observed (Fig. 4.8a); only one significant frazil event occurred during this time period, on 1-Jan-10 at 06:45, just after the air temperature had reached a minimum of -35°C. This is probably because of the thermal energy associated with the warm water outflows from the *WWTP* was insulated from the cold air under the partial ice

cover upstream, preventing the water most of the times from reaching supercooling before it arrive at the site. This single frazil event during the open lead period lasted for 4.5 hours while the water was supercooled to -0.09°C.

Fig. 4.9 presents a 24 hour time period of profiles of the volume backscatter strength S_v (dB) (color coded) and the corresponding time series of the depth averaged volume backscatter strength, S_{vd} (dB) for both the high and the low frequency sonars on 14-Nov-09 and illustrate that the two frazil events on 14-Nov-09 were only detected by the high frequency sonar. The sonar signals from all of the suspended frazil events were very similar to the two events shown in Fig. 4.9, differing only in magnitude and duration of the event. Typically during each frazil event, the time series of S_{vd} (dB) increased gradually until it reached a peak value, and then decreased as the event ended (Fig. 4.9c). Table 4.1 presents a summary of the detected frazil events during the 2009/2010 freeze-up deployment and shows that most of the frazil events were detected in the morning hours when air temperatures were coldest. Events detected during the frazil pan period (events F1 to F7 in Table 4.1) had peak S_{vd} (dB) values that ranged between -50 and -45 (dB) for the high frequency sonar but were not detected with the low frequency sonar. Only the frazil event observed during the open lead period (event F8) was detected with both sonars with a relatively high peak S_{vd} of -38 (dB) and -56 (dB) for the high and the low frequency units, respectively. This event was likely detected with the low frequency sonar because it was the strongest event with the highest peak S_{vd} of -38 dB, which is 7 dB higher than the next highest events F4 and F6 (Table 4.1).

4.6.2 Quantifying Suspended Frazil from the Sonar Outputs

Given the general inability of the low frequency sonar to detect suspended frazil, and the fact that σ_r was always greater than 29.1 when a frazil event was detected by both sonar units; it was not feasible to test the *two-frequency* method with this field data. Therefore, only the *single-frequency* method was tested, with the representative particle size being assumed and the concentrations predicted. This

allowed for an indirect assessment of the applicability of the disk scattering model (Coussios, 2002) for determining suspended frazil concentrations in the field. As a first hypothesis, it was assumed that the frazil particles generated in the laboratory and those detected in the field had the same approximate shape and range of sizes, enabling the time series of S_{vd} (dB) measured during all of the detected frazil events to be converted to frazil concentrations, C (%), using the laboratory correlation equations [i.e. Eq. (4.21) and (4.22)]. The disk scattering model (Coussios, 2002) was then used to compute suspended frazil concentrations for a variety of representative frazil disk radii and these concentrations were then compared to those obtained with the laboratory correlation equations. The disk radii associated with the calculated disk model concentrations that best matched the concentrations estimated using the laboratory correlations were then compared to the representative disk size observed in the laboratory, to see if there were any consistencies. The application of this technique is illustrated in Fig. 4.10 for the high frequency data of a typical freeze-up (frazil pans period) event on 28-Nov-09 (event F4, Fig. 4.10a), and for both the high and the low frequency data for the open lead event on 1-Jan-10 (event F8, Fig. 4.10b and 4.10c, respectively).

Fig. 4.10 shows that, in general, the time series of estimated concentrations from the laboratory equations and from the disk scattering model are reasonably comparable and that a single representative particle size can model most of the ranges of concentrations detected during each event. This indicates that the scattering model and the laboratory equations responded similarly to the variations in S_{vd} (dB). There are two possibilities for this similarity: either that observed frazil ice particles in the field are similar to frazil particles generated in the laboratory so that the sonar signal is mainly a function of concentration, or that the particle sizes in the field change continuously with concentration so that the resulting sonar backscattered signal when modeled with a single particle size, happened to agree with the laboratory equations' estimated concentrations. The latter is very unlikely to occur, therefore, it was believed that it is an acceptable approximation to model frazil ice particles in the field using a dominant

representative size. This conclusion was supported by field observations of suspended frazil particles using time lapse underwater photographs, reported by Osterkamp and Gosink (1982 and 1983). They concluded that during a frazil event, the size distribution of frazil particles remains roughly constant and that their concentration varied about an order of magnitude throughout the event. This implies that the assumption that the sonar signal is mainly a function of concentration is valid.

The estimated peak frazil concentrations and deduced disk radii for all of the frazil events are listed in Table 4.2. For the freeze-up frazil events (F1 to F7), peak concentrations and disk radii ranged between 0.012 % and 0.022%, and between 0.13 mm and 0.15 mm, respectively. For the open lead event (F8), the peak concentration from the high and the low frequency data were 0.049% and 0.042%, respectively; and the disk radii deduced from the high and low frequency data were 0.19 mm and 0.21 mm, respectively (Table 4.2). The fact that concentrations and disk radii predicted from the laboratory equations and the theoretical model for the high and the low frequency sonar data are in such close agreement for the same frazil event, supports the hypothesis that the frazil ice particles produced in the North Saskatchewan River were similar in size and shape to the particles generated in the frazil ice tank. This seems plausible because the frazil ice must have been generated in the open lead that extended only ~ 6 km upstream where the city *WWTP* is located. Given that the water would first have to cool to below 0 °C, this means that the zero degree isotherm was likely not too far upstream and thus the detected frazil was probably recently generated. Freshly formed frazil in the field is more likely to be similar to frazil generated under laboratory conditions. Given the apparent validity of this assumption, it appears that reasonable estimates of suspended frazil concentrations can also be obtained with the laboratory regression equations. In addition, these results also suggest that the estimated speed of sound in frazil ice of 2554 m/s used in this study is reasonable.

A wide range of frazil concentrations were estimated in previous studies: in the laboratory between 0.01 and 0.60% (Ettema et al., 2003; Ye et al., 2004; Ghobrial et al., 2012a) and in the field from 0 to 0.03 % (Tsang, 1986) and from 0 to 0.25% (Tsang, 1984). In this study, the concentrations estimated in the field using the laboratory equations were between ~ 0.01 and 0.05% which is within the ranges previously reported. The deduced disk radii from the scattering models ranged from 0.13 and 0.21 mm which is within the means of the size distributions of particles radii measured in previous laboratory studies of 0.10 mm (Daly and Colbeck, 1986), 0.65 mm (Clark and Doering, 2006), and 0.40 mm (McFarlane, 2012). No previous field data describing the size distribution of suspended frazil ice are available for comparison. The speed of sound in frazil ice of 2554 m/s used in this study is consistent with the value of 2760 m/s used by Richard et al. (2010) for frazil in the St. Lawrence River, Canada.

4.7 Summary and Conclusions

Acoustic field data gathered with upward looking sonars during freeze-up have been processed and analyzed to provide estimates of frazil concentration and particle sizes in rivers. First, the applicability of three scattering models (sphere, prolate spheroid, and disk) were assessed by applying these models to the sonar laboratory data reported by Ghobrial et al. (2012a), to estimate the corresponding concentration. It was found that the model estimated concentrations follow the same approximate trend of the laboratory data, and that laboratory measurements can be modeled using a single particle size. These results support the hypothesis that the size distribution of frazil particles does not change significantly with concentration and that the sonar signal is primarily a function of the concentration.

Eight frazil events with varying duration and magnitude were detected during the field deployment. During all of these events, time series of the estimated concentrations from the laboratory equations and the disk scattering model were very similar; they always vary with the same approximate magnitude and trend

during each frazil event. Also it was found that almost one particle size can model approximately all the range of concentrations estimated during each event. These findings validate the assumption that observed frazil ice particles in the field are similar to frazil particles generated in the laboratory. This implies that the sonar backscattered signal is mainly a function of concentration, and that it is an acceptable approximation to model frazil ice particles in the field using a dominant representative size.

The freeze-up events (seven events during frazil pan period) ranged in concentration between 0.012 and 0.022% and disk radius between 0.13 and 0.15 mm; and were only detected with the high frequency sonar. Only the open lead frazil event was detected with both the high and the low frequency sonars. During this event, concentrations and sizes estimated from the high and the low frequency sonars were very close ($C \approx 0.045$ % and $a \approx 0.20$ mm). In order for the high and the low frequency sonars to predict the same concentrations values from the same suspended frazil population using the laboratory equations, the frazil ice observed in the field and generated in the laboratory must have the same approximate shape and size. Results from this technique need to be validated either with multi-frequency measurements or with direct observations (e.g. photographic measurements) close to the upward looking sonar to provide local measurements of the concentrations and the sizes near the transducer head.

Tables

Table 4.1 Time and duration of the frazil events detected during the 2009/2010 freeze-up field deployment and the peak depth average volume backscatter strength, S_{vd} (dB) for each frazil event, measured with the high (546 kHz) and the low (235 kHz) frequency sonars. Also, the air temperature, T_a (°C) and the water temperature, T_w (°C), averaged over the duration of the event are listed. Events F1 to F7 were detected during the frazil pans period, and event F8 was detected in the open lead.

Event	Start time and date	Duration (h)	T_a (°C)	T_w (°C)	Peak S_{vd} (dB)	
					High freq	Low freq
F1	06:45 14-Nov-09	3:30	-5	-0.08	-50	-
F2	19:15 14-Nov-09	4:15	-2	-0.08	-47	-
F3	05:00 25-Nov-09	3:00	-10	-0.08	-50	-
F4	06:00 28-Nov-09	3:15	-7	-0.09	-45	-
F5	08:00 01-Dec-09	2:15	-5	-0.08	-46	-
F6	05:00 02-Dec-09	6:00	-12	-0.09	-45	-
F7	16:00 02-Dec-09	11:00	-12	-0.08	-47	-
F8	06:45 01-Jan-10	4:30	-25	-0.09	-38	-56

Table 4.2 Peak estimated suspended frazil concentration, *C* (%) and the corresponding deduced frazil disk radius, *a* (mm) from the high (546 kHz) and the low (235 kHz) frequency sonar data for the frazil events detected during the 2009 freeze-up field deployment.

Event	Peak *C* (%)		*a* (mm)	
	High freq	Low freq	High freq	Low freq
F1	0.014	-	0.13	-
F2	0.018	-	0.14	-
F3	0.012	-	0.13	-
F4	0.022	-	0.15	-
F5	0.018	-	0.14	-
F6	0.021	-	0.15	-
F7	0.020	-	0.14	-
F8	0.049	0.042	0.19	0.21

Figures

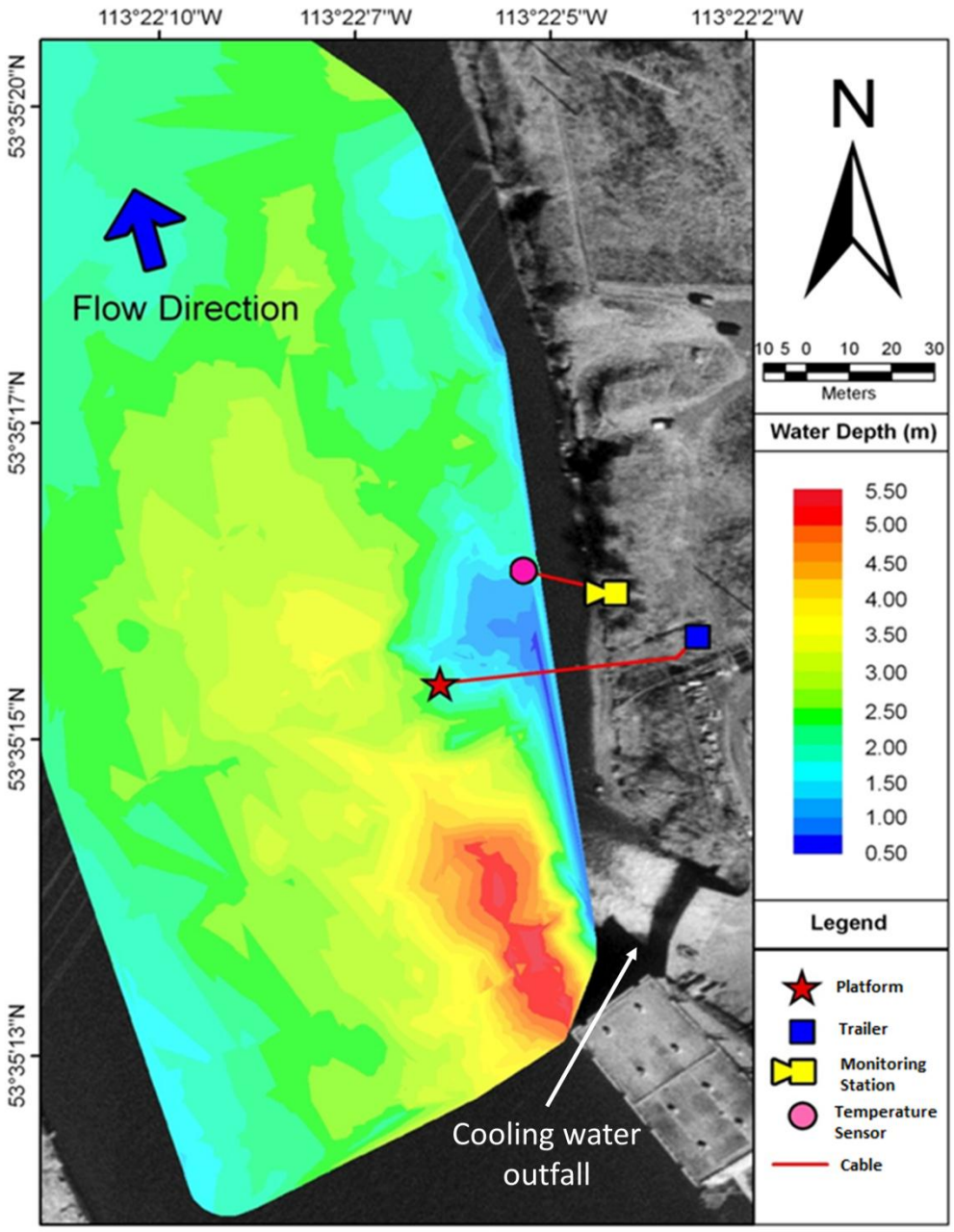

Fig. 4.1. An aerial photograph of the deployment site with the bathymetric survey in 0.5 m increments plotted in color showing the locations of the instrument platform, temperature sensor, monitoring station (Webcam) and trailer. The power station's cooling water outfall and the river-water pump house are also shown.

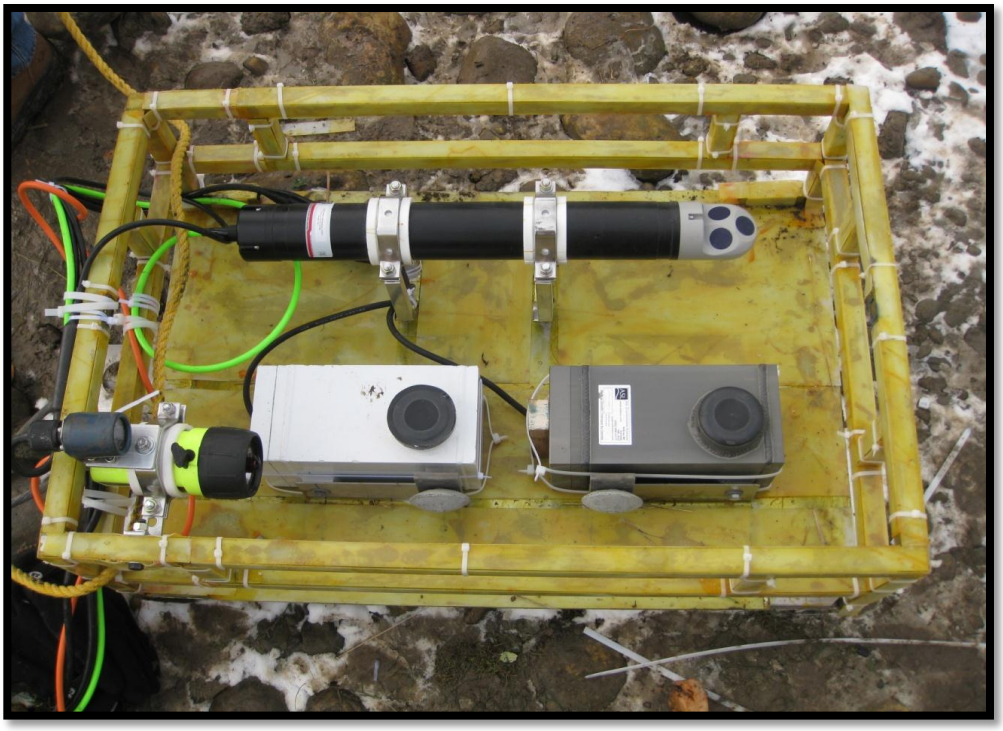

Fig. 4.2. Picture of the deployment platform used to hold the high and the low frequency sonar units, the water current profiler, and the underwater video camera and light.

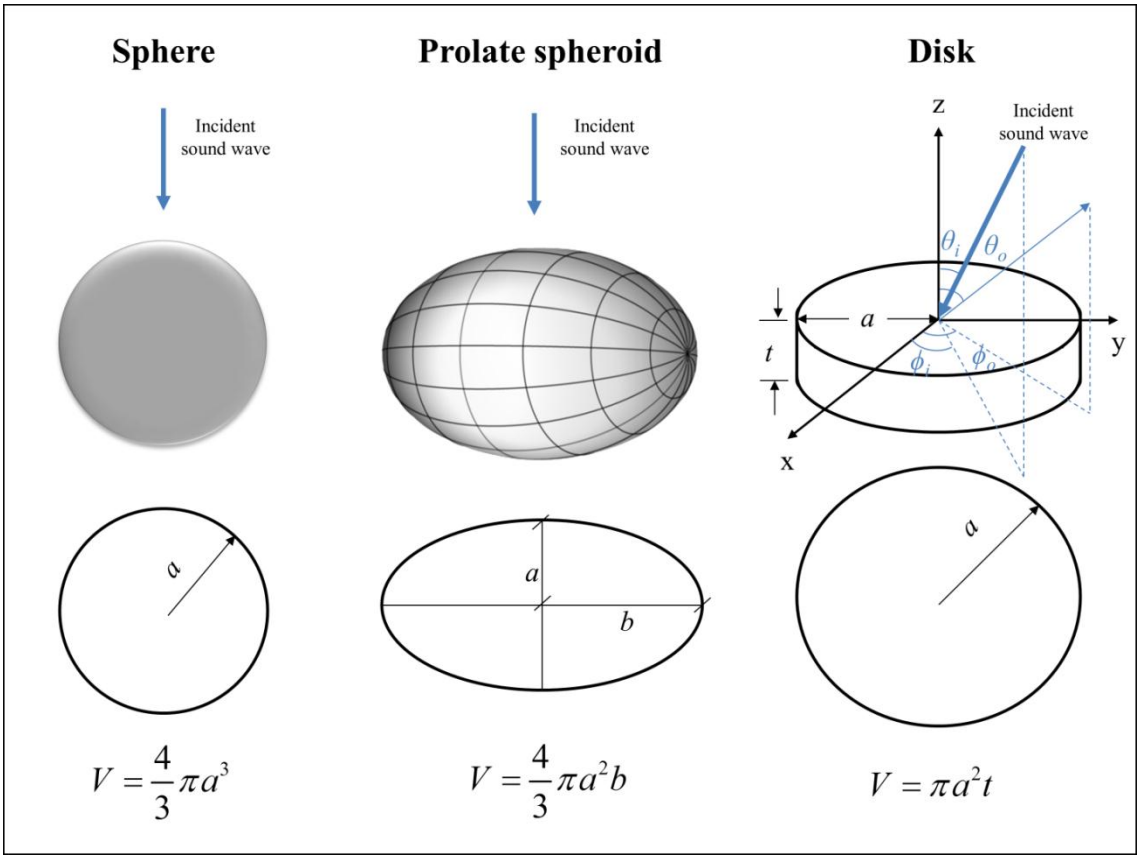

Fig. 4.3. A schematic diagram illustrating the basic geometry and the definition of the different dimensions used by the scattering models for each shape: *a* is the radius of sphere, the semi-minor axis of the prolate spheroid, and the disk radius; *b* is the semi major axis of the prolate spheroid; and *t* is the disk thickness. Note: the disk geometry and angles were adapted from Coussios (2002).

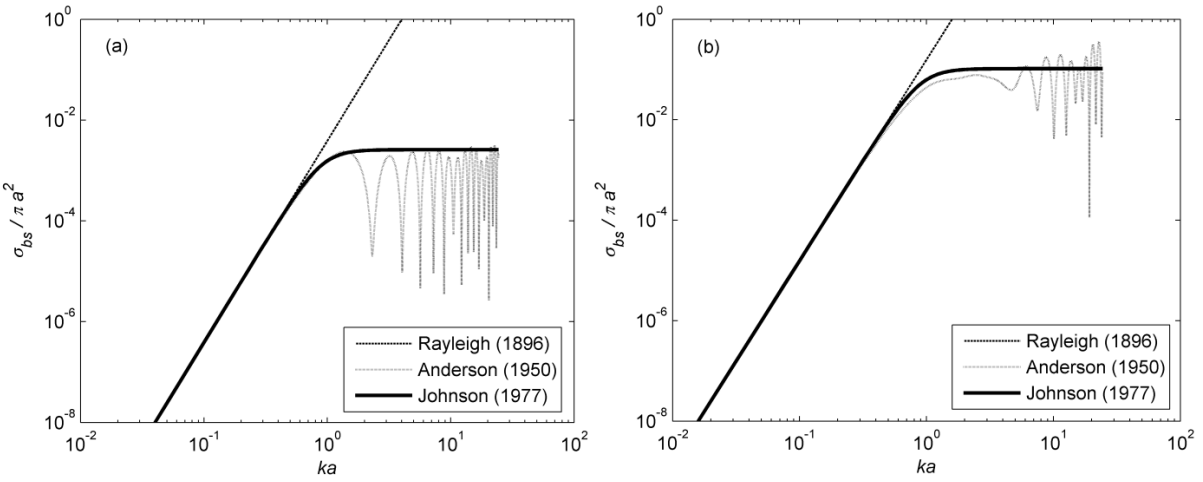

Fig.4.4. plot of the non-dimensional backscatter cross section, $\sigma_{bs} / \pi a^2$, versus the non-dimensional particle size, *ka*, estimated using Rayleigh (1896), Anderson (1950), and Johnson's (1977) sphere models for: (a) typical fluid target (euphausiid) of $R\rho$ = 1.016 and Rc = 1.033 (adapted from Johnson, 1977), and (b) frazil ice particles of $R\rho$ = 0.92 and Rc = 1.82.

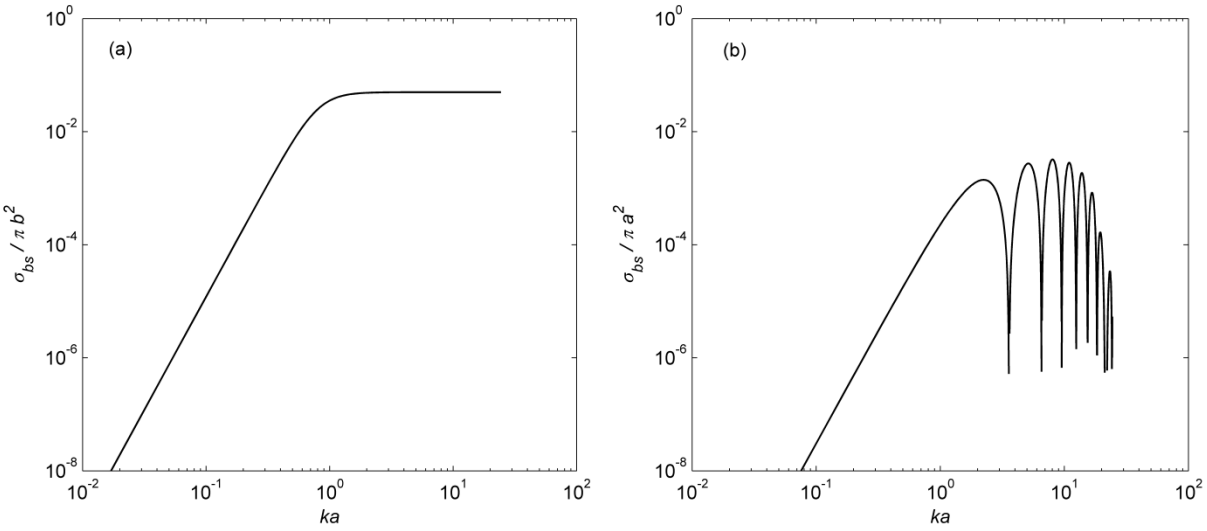

Fig. 4.5. plot of the non-dimensional particle size, *ka* versus: (a) the non-dimensional backscatter cross section, $\sigma_{bs} / \pi b^2$, calculated using an aspect ratio of 10 for *b* / *a* for the prolate spheroid (Stanton, 1989), and (b) the non-dimensional backscatter cross section, $\sigma_{bs} / \pi a^2$, calculated using an aspect ratio of 10 for 2*a* / *t* for the disk model (Coussios, 2002); computed for frazil ice particles ($R\rho$ = 0.92 and *Rc* = 1.82).

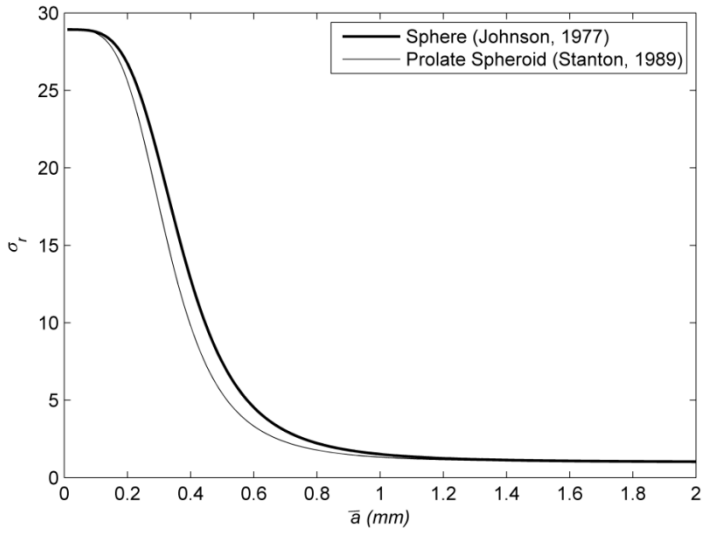

Fig.4.6. Plot of the ratio of the backscatter coefficient, σ_r , from the high to the low frequency data, versus the dominant radius, $\bar{a}$ (mm) for Johnson's (1977) sphere model and Stanton's (1989) prolate spheroid model.

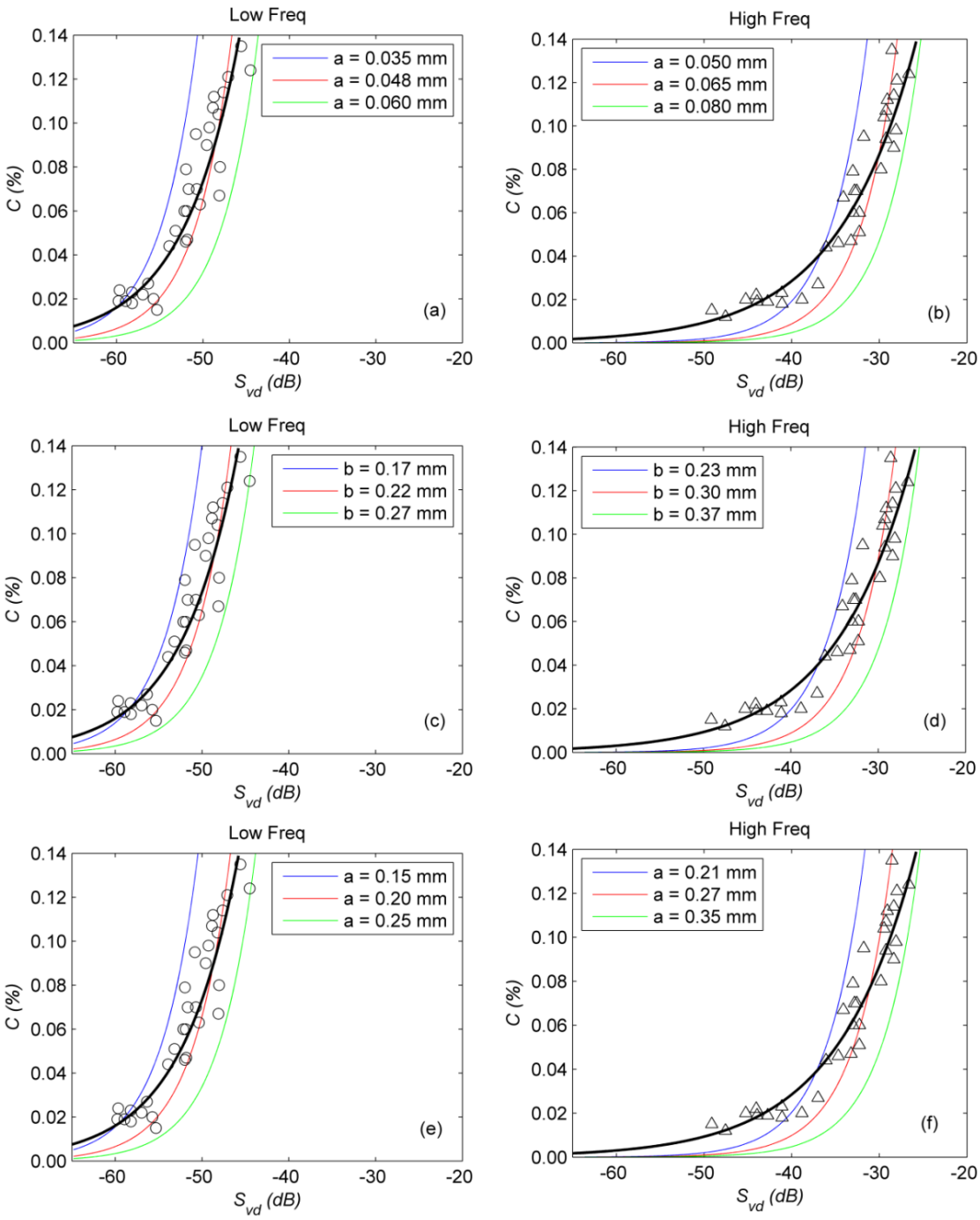

Fig. 4.7. Depth averaged volume backscattered strength, S_{vd} (dB) versus Concentrations, C (%) estimated for three particle sizes for the sphere mode in (a) and (b), the prolate spheroid model in (c) and (d), and for the disk model in (e) and (f). Also the experimental data points: (○) for the low frequency in (a), (c) and (e) and (Δ) for the the high frequency in (b), (d), and (f) together with their corresponding regression equations (solid black line) are plotted.

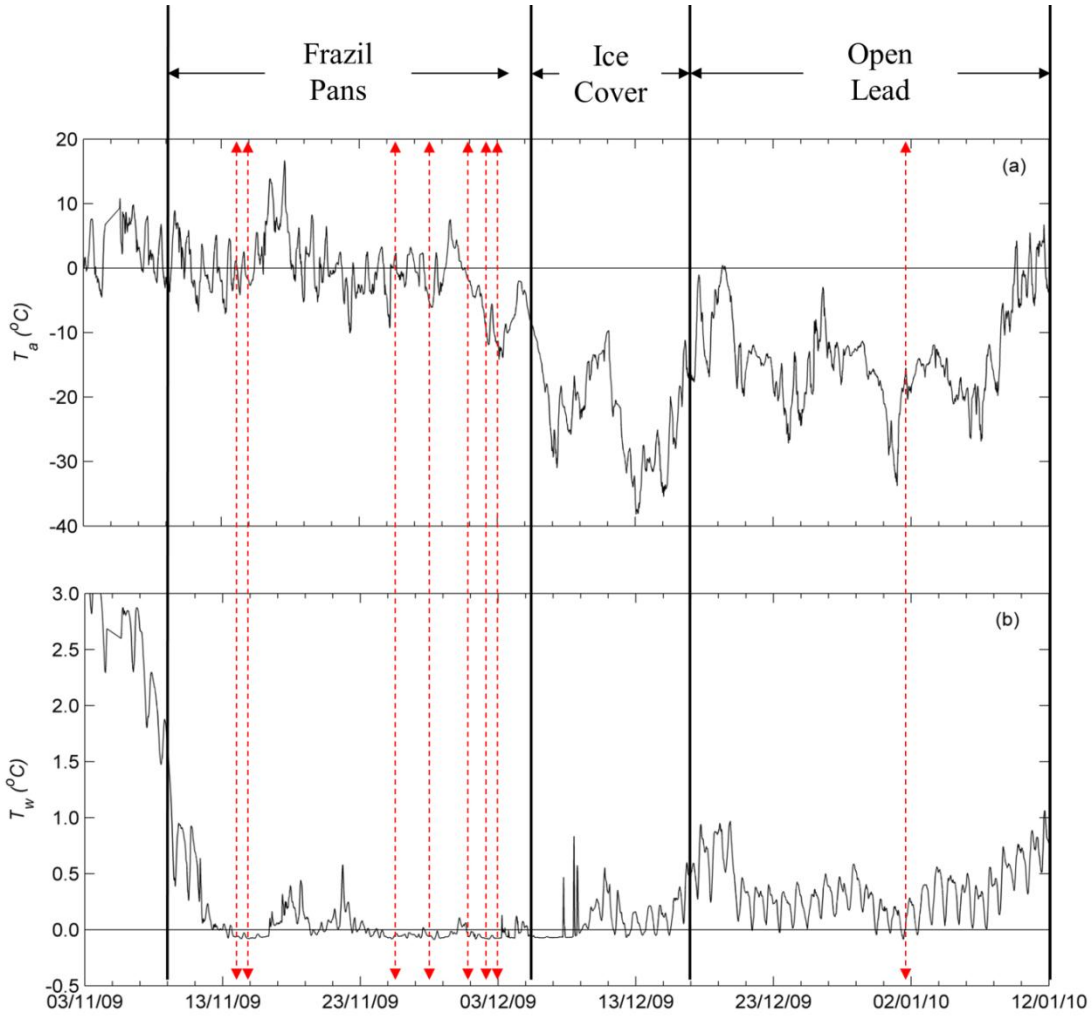

Fig. 4.8. Time series of 30 minutes moving average of: (a) air temperature, T_a (ºC), and (b) water temperature, T_w (ºC), measured at the deployment site from 03-Nov-09 to 12-Jan-10 and labeled with the observed surface ice conditions. The red dotted vertical arrows indicate approximately the dates of the detected frazil events.

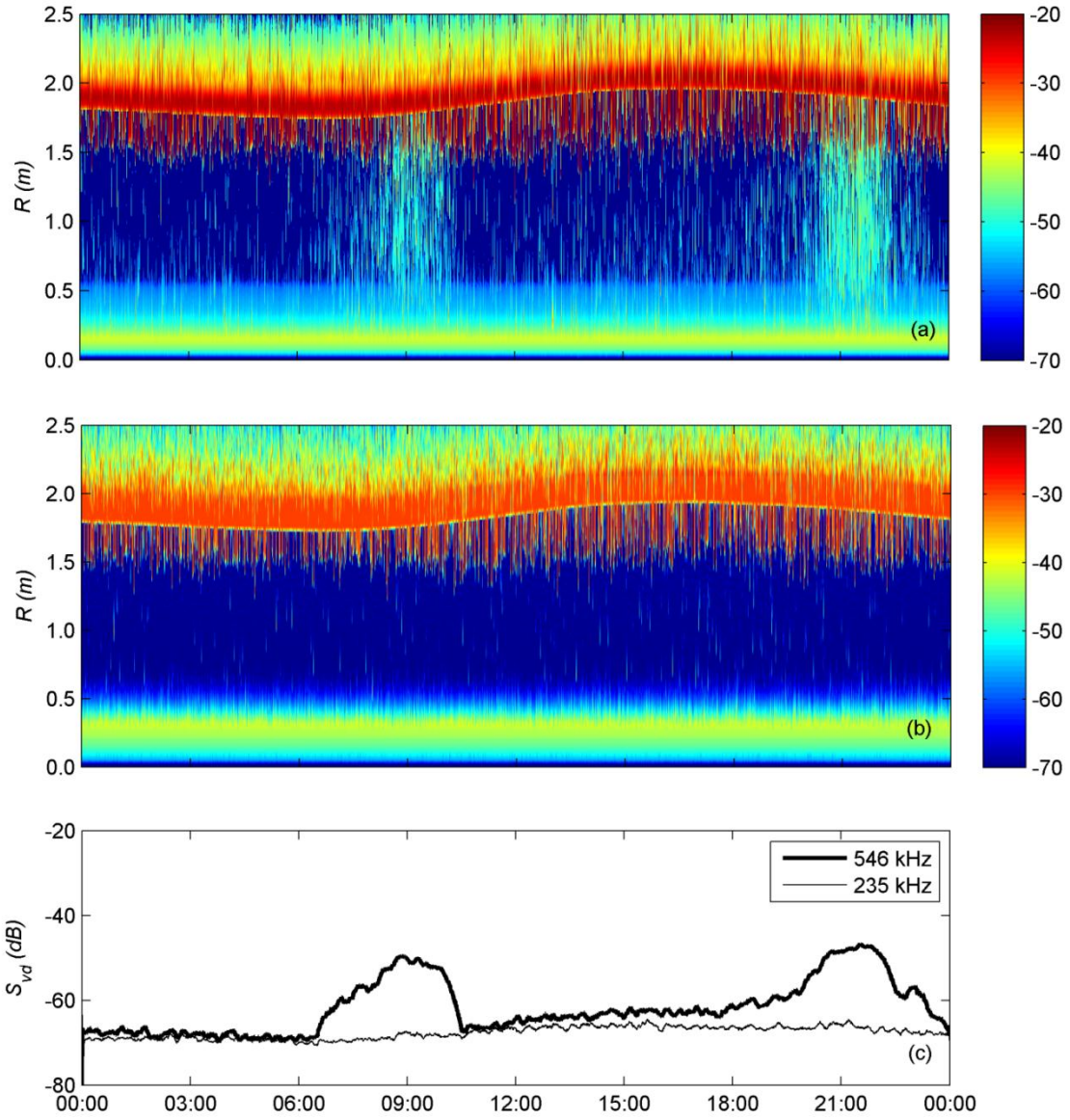

Fig. 4.9. Time series data of 24 hrs time period on 14-Nov-09 showing 2-D plot of S_v (dB, color coded) data, range R (m) above the transducer versus time (hrs) for (a) the high and (b) the low frequency data; (c) the depth average volume backscatter strength, S_{vd} (dB) computed from the high (546 kHz) and the low frequency (235 kHz) data in (a) and (b). Note: the two frazil events on 14-Nov-09 were only detected with the high frequency sonar and the low frequency signal did not show any variation from the background noise.

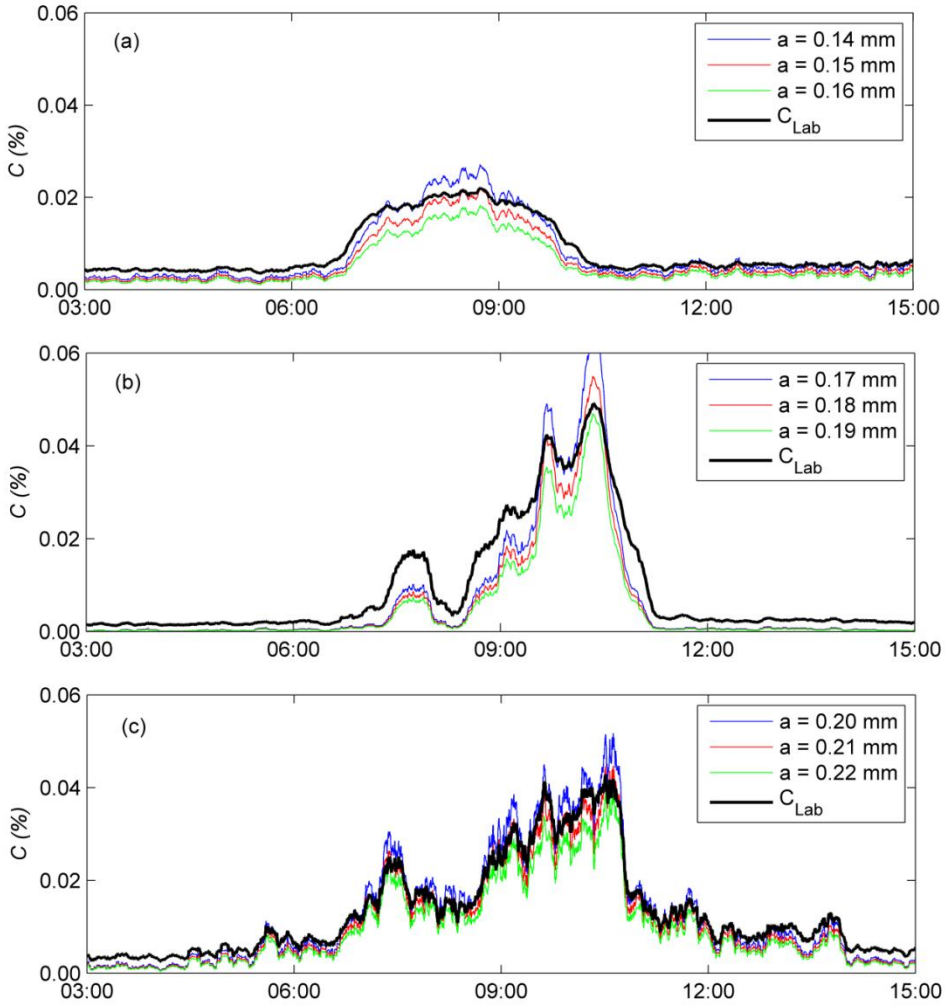

Fig. 4.10. Time series of concentrations, *C* (%) estimated using the laboratory regression equations (solid black line), and using the disk model for various disk radii, *a* (mm) for: (a) the high frequency data from the frazil event on 28-Nov-09 (event F4), (b) and (c) the high and the low frequency data, respectively, for the frazil event on 1-Jan-10 (event F8).

References

Anderson, V.C., 1950. Sound scattering from a fluid sphere. Journal of the Acoustical Society of America 22, 426–431.

Ashton, G. (Ed.), 1986. River and Lake Ice Engineering. Water Resources Publications, Littleton, CO.

Bowman, J.J., Senior, T.B.A., Uslenghi, P.L.E. (Eds.), 1969. Electromagnetic and Acoustic Scattering by Simple Shapes. North-Holland, Amsterdam. 728 pp.

Clark, S., Doering, J.C., 2006. Laboratory Experiments on Frazil-Size Characteristics in a Counter Rotating Flume. Journal of Hydraulic Engineering, 132(1), 94-101.

Clay, C.S., and Medwin, H., 1977. Acoustical Oceanography. Wiley-Interscience, New York. 544 pp.

Coussios, C-C., 2002. The significance of shape and orientation in single-particle weak-scatterer models. J. Acoust. Soc. Am., Vol. 112, No. 3, 906-915.

Daly, S.F., 1994. International Association for Hydraulic Research Working Group on Thermal Regimes: Report on Frazil Ice. U.S. Army Corps of Engineers Special Report 94-23. 43p.

Daly, S.F., 2008. Evolution of frazil ice. Proceedings of the 19th IAHR International Symposium on Ice, Vancouver, BC, Canada, pp. 29-47.

Daly, S.F., and Colbeck, S., 1986. Frazil Ice Measurements in CRREL's Flume Facility. Proc. Syrup. Ice 1986. Int. Assoc. Hydraul. Res., Iowa City, Iowa, pp. 427--438.

Doering, J.C., and Morris, M.P., 2003. A Digital Image Processing System to Characterize Frazil Ice. Canadian Journal of Civil Engineering, 30: 1–10.

Ettema, R., Chen, Z., and Doering, J., 2003. Making Frazil Ice in a Large Ice Tank. Proceedings of the 12th Workshop on the Hydraulics of Ice Covered Rivers, Committee on River Ice Processes and the Environment, Edmonton, Canada, 13 pp.

Feuillade, C., 2004. Animations for visualizing and teaching acoustic impulse scattering from spheres. J. Acoust. Soc. Am. 115 (5), 1893-1904.

Feuillade, C. and Clay, C.S., 1999. Anderson (1950) revisited. J. Acoust. Soc. Am. 106, 553–564.

Gartner, J.W., 2004. Estimating Suspended Solids Concentrations from Backscatter Intensity Measured by Acoustic Doppler Current Profiler in San Francisco Bay, California. Marine Geology 211, no. 3-4: 169-187.

Ghobrial, T.R., Loewen, M.R., and Hicks, F.E., 2012a. Laboratory calibration of upward looking sonars for measuring suspended frazil ice concentration. Cold Reg. Sci. Technol. (70): 19-31.

Ghobrial, T.R., Loewen, M.R., and Hicks, F.E., 2012b. Continuous monitoring of river surface ice during freeze-up using upward looking sonar. Manuscript to be submitted to the journal of Cold Regions Science and Technology.

Gold, L.W., 1988. On the elasticity of ice plates. Can. J. Civ. Eng. 15.pp. 1080-1084.

Greenlaw, C.F. 1979. Acoustical estimation of zooplankton populations. Limnology and Oceanography 24(2): 226–242.

Holliday, D.V., and Pieper, R.E., 1995. Bioacoustical oceanography at high frequencies. ICES J. mar. Sci., 52: 279-296.

Jasek, M., Ghobrial, T.R., Loewen, M.R., Hicks, F.E., 2011. Comparison of CRISSP modeled and SWIPS measured ice concentrations on the Peace River. In Proceedings of 16th Workshop on River Ice Winnipeg, Manitoba, pp 249-273.

Johnson, R. K., 1977. Sound scattering from a fluid sphere revisited, J. Acoust. Soc. Am., 61(2), 375-377. (Erratum: Sound scattering from a fluid sphere revisited, J. Acoustic. Soc. Am., 63(2), 626, 1978.)

Kristensen, A., and Dalen, J., 1986. Acoustic estimation of size distribution and abundance of zooplankton. J. Acoust. Soc. Am. 80 (2): 601- 611.

Lever, J., Daly, S., Rand, J., Furey, D., 1992. A Frazil Ice Concentration Meter. Proceedings of the 11th IAHR Symposium, Banff, Canada, 1362-1376 .

Marko, J.R., Jasek, M., 2010a. Sonar Detection and Measurements of Ice in a Freezing River I: Methods and Data Characteristics. Cold Regions Science and Technology. 63, 121–134.

Marko, J.R., Jasek, M., 2010b. Sonar Detection and Measurement of Ice in a Freezing River II: Observations and Results on Frazil Ice. Cold Regions Science and Technology. 63, 135–153.

Marko, J.R., Jasek, M., 2010c. Frazil Monitoring by Multi-frequency Shallow Water Ice Profiling Sonar (SWIPS): Present Status. Proceedings of the 20th IAHR International Symposium on Ice, Lahti, Finland, June 14 to 18, 2010.

Martin, S., 1981. Frazil Ice in Rivers and Oceans. Ann. Rev. Fluid Mechanics, 13:379-97.

McFarlane, V., Loewen, M.R., and Hicks, F.E., 2012. Laboratory Experiments to Determine Frazil Ice Properties. Proceedings of the Annual General Conference of the Canadian Society of Civil Engineers, Edmonton, Alberta, Canada, June 6 to 9, 2012.10p.

Medwin, H., and Clay, C.S., 1998. Fundamentals of Acoustical Oceanography. Academic Press, San Diego, 712 pp.

Morse, B., and Richard, M., 2009. A Field Study of Suspended Frazil Ice Particles. Cold Regions Science and Technology, Volume: 55, pp 86–102.

Nadreau, J-P. and Michel, B., 1984. Ice properties in relation to ice forces. Proceedings of the 7th IAHR Ice Symposium, 1984, Hamburg, Germany.

Osterkamp, T.E., 1978. Frazil ice formation: A review. Journal of the hydraulic division, ASCE, 104(HY9): 1239-1255.

Osterkamp, T.E., and Gosink, J. 1983. Frazil Ice Formation and Ice Cover Development in Interior Alaska Streams. Journal of Cold Regions Science and Technology, v 8 p 43-56.

Powers, D.L., 2006. Boundary Value Problems and Partial Differential Equations. Fifth Edition, Elservier Academic Press, Amsterdam, 501pp.

Rayleigh, J., 1896. The Theory of Sound, Vol. 2 (Dover, New York, 1945).

Richard, M., Morse, B., Daly, S.F. and J. Emond, 2010. Quantifying suspended frazil ice using multi-frequency underwater acoustic devices. River Research and Applications. DOI: 10.1002/rra.1446.

Stanton, T.K., 1989. Simple approximate formulas for backscattering of sound by spherical and elongated objects. J. Acoustic. Soc. Am. 86 (4) 1499-1510.

Thevenot, M.M., and Kraus, N.C., 1993. Comparison of Acoustical and Optical Measurements of Suspended Material in the Chesapeake Estuary. J. Marine Environmental Engineering, 1: 65– 79.

Thevenot, M.M., Prickett, T.L., Kraus, N.C., 1992. Tylers Beach,Virginia, Dredged Material Plume Monitoring Project 27 September to 4 October 1991. Dredging Research Program Technical Report DRP-92-7, US Army Corps of Engineers, Washington, DC, 204 pp.

Thorne, P.D., Hardcastle, P.J., and Soulsby, R.L., 1993. Analysis of Acoustic Measurements of Suspended Sediments. Journal of Geophysical Research, vol:98, No: C1, pages:899-910.

Thorne, P.D., and Meral, R., 2008. Formulations of the scattering properties of suspended sandy sediments for use in the application of acoustics to sediment transport processes. Continental Shelf Research (28) 309-317.

Tsang, G., 1982. Frazil and Anchor Ice: a Monograph. Natural Resources Council Subcommittee on Hydraulics of Ice Covered Rivers, Ottawa, Ontario, Canada, 90 p.

Tsang, G., 1984. Concentration of frazil in flowing water as measured in laboratory and in the field. Proc. 1984 Ice Symp. Int. Assoc. Hydraul. Res., Hamburg, Germany, Vol. III: 99-111.

Tsang, G., 1985. An Instrument for Measuring Frazil Concentration. Cold Regions Science and Technology, Volume: 10, Issue: 3, Pages: 235-249

Tsang, G., 1986. Preliminary report on field study at Lachine Rapids on cooling of river and formation of frazil and anchor ice. Proceedings of the 4th Workshop on the Hydraulics of Ice Covered Rivers, Montréal, Canada, pp. F5.1-5.51.

Urick, R.J., 1983. Principles of Underwater Sound. 3rd Edition. McGraw-Hill, Inc., 423 pp.

Wueben, J.L., 1984. The rise pattern and velocity of frazil ice, CRIPE, Proceedings of the 3rd Workshop on the Hydraulics of Ice Covered Rivers, Fredericton, NB.

Yankielun, N., Gagnon, J., 1999. Laboratory Tests of a Time-Domain Reflectometry System for Frazil Ice Detection. Canadian Journal of Civil Engineering, 26: 168–176.

Ye, S.Q., Doering, J.C., Shen, H.T., 2004. A Laboratory Study of Frazil Evolution in a Counter Rotating Flume. Canadian Journal of Civil Engineering, 31(6), 899-914.

CHAPTER 5: Conclusions and Recommendations

5.1 Summary and Conclusions

This research aimed at developing a technique for obtaining quantitative measurements of suspended frazil ice and surface ice characteristics in rivers using the shallow water ice profiling sonars. A series of laboratory controlled experiments were conducted in a specially designed frazil ice tank located in the University of Alberta Cold Room Facility. Two shallow water ice profiling sonars: one low (235 kHz) and one high (546 kHz) frequency were deployed on the bottom of the frazil tank, and direct sieve measurements of frazil ice concentrations were correlated with the corresponding sonar backscatter signal. The measured concentrations ranged from 0.012 % to 0.135 %. Sieved frazil ice particles were examined under a microscope to determine the average shape and size of the particles. The majority of the observed frazil ice particles were disk shaped and ranged from 0.25 to 4.25 mm in diameter.

A significant correlation was observed between the sonar signals and the frazil concentration measurements in the laboratory. A linear least square regression analysis was used to fit a logarithmic equation to relate the relative backscatter to the frazil concentration. The resulting coefficients of determination, R^2, were 0.96 and 0.93 for the high and low frequency data, respectively. The maximum concentration that can be measured before saturating the high frequency sonar signal was found to be ~0.15 %. The low frequency sonar signal was never saturated even when frazil flocs were present in the tank. The regression equations predict that the minimum concentrations that can be measured using the high and the low frequency sonars is 0.0034 % and 0.017 %, respectively, due to the background noise level.

A series of field experiments were conducted using a high and a low frequency sonars, an acoustic Doppler current profiler, and an on-shore monitoring station

equipped with digital cameras and temperature sensors during the 2009/2010 freeze-up season on the North Saskatchewan River in Edmonton, Alberta. These field experiments aimed at gathering sonar field data of surface ice and suspended frazil ice during freeze-up. An algorithm was developed to process the raw sonar and current profiler data in order to extract the surface ice concentration, pan drafts and lengths. Statistical tests of the similarity of the results from the high (546 kHz) and low frequency sonar (235 kHz) units showed that either instrument is suitable for the purpose of surface ice measurements. The ice measurements computed from the sonar data were validated with laboratory tests, webcam images and in-situ measurements demonstrating that this technique provides reliable measurements of local surface ice characteristics.

The freeze-up season was divided into three distinct time periods: frazil pans, ice cover, and open lead. The frazil pans period was further sub-divided into three phases: Phase I was defined as the ice initiation phase, phase II as the consistent surface ice concentration phase, and phase III as the transition between the pan phase and the formation of the continuous ice cover. At the deployment site, pan characteristics observed early during Phase I and during the open lead periods, were very similar. Pan/raft drafts and lengths were approximately 0.1 m and 1.0m, respectively. During Phase II (consistent surface ice concentrations), pan drafts generally ranged between 0.1 to 0.4 m and pan lengths between 1.0 and 3.0 m, with the ratio of draft to length ranging between 0.1 and 0.2. An exponential expression was proposed to model the field measurements of the non-dimensional near-surface velocity to its corresponding surface concentration during the frazil pans/rafts period. However, the parameters of this equation are site specific and need to be validated for each deployment.

Acoustic field data gathered during suspended frazil events have been processed and analyzed to provide estimates of frazil concentration and particle sizes in rivers using laboratory regression equations and theoretical scattering models. First, the applicability of theoretical scattering models to frazil ice particles was assessed by applying these models to the sonar laboratory data. Frazil ice particles

were modeled as fluid disk targets based on assumed sound speed in ice of 2554 m/s, and a diameter to thickness ratio of 10. It was found that the model estimated concentrations follow the same approximate trend of the laboratory data, and that laboratory measurements can be modeled using a single particle size. These results support the hypothesis that the size distribution of frazil particles does not change significantly with concentration and that the laboratory regression equations are primarily a function of the concentration.

Laboratory regression equations were used to directly predict suspended frazil concentrations from the sonar data gathered during suspended frazil events. This assumed that frazil observed in the field is similar (in shape and range of sizes) to laboratory generated frazil. The disk scattering model was used to deduce the dominant particle size that matches the concentrations estimated from the laboratory equations. Using this methodology, the peak concentrations ranged between 0.012 and 0.022% and the corresponding disk radii ranged between 0.13 and 0.15 mm during the freeze-up events (seven events during frazil pan period); and were only detected with the high frequency sonar. Only one event during the open lead period was detected with both the high and the low frequency sonars. During this event, the peak concentration from the high and the low frequency data were 0.049% and 0.042%, respectively; and the disk radii deduced from the high and low frequency data were 0.19 mm and 0.21 mm, respectively.

It was found that time series of the estimated concentrations from the laboratory equations and the scattering model were in a reasonable agreement, and that almost one particle size can model approximately all the range of concentrations estimated during each event. Also, when the same frazil event was detected with the high and the low frequency (the open lead event), the laboratory regression equations predicted very close concentrations values ($C \approx 0.045$ % and $a \approx 0.20$ mm) from both sonar instruments. These findings validate the assumption that observed frazil ice particles in the field are similar to frazil particles generated in the laboratory, which implies that the sonar backscattered signal is mainly a function of concentration, and that it is an acceptable approximation to model

frazil ice particles in the field using a dominant representative size. Given the apparent validity of this assumption, it appears that reasonable estimates of suspended frazil concentrations in the field can be obtained with the laboratory regression equations. In addition, these results also suggest that the estimated speed of sound in frazil ice of 2554 m/s used in this study is reasonable.

5.2 Recommendations for Future Research

The techniques and findings presented in this research are very promising. The upward looking sonar proved to be a robust tool for continuous measurements of suspended frazil ice as well as surface ice properties in rivers. However, in the field deployment, these measurements are limited in space to the instrument location. Therefore, in order to provide a complete monitoring of surface freeze-up processes, additional monitoring methods such as remote sensing, aerial photographs, or web-based on-shore cameras, are required to interpret the sonar results. Also, the water temperature should be monitored up to several kilometers upstream in order to determine the location of the zero degree isotherm. This will allow better understanding of the formation and transport of frazil ice in rivers and can be used to correlate frazil ice characteristics (concentration and sizes) detected with the sonar at the instrument location with the distance traveled by the suspended frazil particles upstream.

In this study, the laboratory equations and the fluid disk scattering model were used in conjunction to estimate suspended frazil concentrations and particle sizes. The accuracy of these estimates need to be validated either with multi-frequency measurements or with direct observations (e.g. photographic measurements) close to the upward looking sonar to provide local measurements of the concentrations and the sizes near the transducer head. Estimation of frazil characteristics from the scattering model was based on a single particle size and fixed diameter to thickness ratio. Therefore, a more sophisticated algorithm that can model a size distribution (compared to a single size) of frazil ice with varying diameter to thickness ratios is needed for a more accurate prediction of frazil concentrations

from the sonar signal using the scattering models. Theoretical scattering models depend mainly on the contrast in density and the speed of sound between the insonified targets (i.e. frazil ice particles) and the surrounding medium (i.e. water). Although in this study efforts have been made to come up with the most appropriate approximation of the sound speed in frazil ice particles, but the need is to measure the acoustic characteristics of frazil ice particles in the laboratory in order to refine the results of this research.

Appendices

Appendix A. Slush Layer Experiments

Motivation and Background

Accumulation of frazil slush underneath ice covers and frazil pans can interfere with navigation, block water intakes used for drinking water, manufacturing, and oil refining by accumulating over the intakes screens. One of the most adverse impacts is the blockage of water intakes at hydroelectric power plants that can cause a complete shutdown of the generators for significant amounts of time. Many engineering solutions have been investigated and developed to minimize intake blockage by frazil ice and slush accumulation (Daly, 1991). Development of effective solutions has proven difficult because of a lack of understanding of the frazil ice formation process and a lack of accurate measurements of slush characteristics in rivers.

There have been very few laboratory studies conducted investigating the formation of fresh water slush (e.g. Hanley and Michel, 1977). Field experiment by Beltaos and Dean (1981) on the Smoky River, Alberta, found that the slush porosity (water content) underneath hanging dams varied from 43 to 65%. Dean (1977) found from observations on St. Lawrence River, Quebec, that the slush accumulations is a mixture of frazil ice and larger pieces of solid ice with porosities varying from 50 to 60%. Lawson and Brockett (1990) measured slush porosities between 0.35 and 0.65% from core samples off a solid ice cover on Tanana River, Alaska. Dean (1986) developed field technique to sample frazil accumulations and measure its characteristics. He reported slush porosities between 45 to 60% for recent deposition of slush in a low velocity reach. Andres and Spitzer (1989) suggested a value of 70% for modeling the floating slush porosity on Peace River, AB. This value was suggested so that the uncompact

floating slush would have higher porosity than the sampled accumulations of slush from underneath hanging dams and near the bank at isolated locations.

The ability to develop a robust technique to measure the thickness and porosity (defined as the percentage water content) of slush layers would be extremely useful. Upward looking sonars can typically detect the lower boundary of slush layers but it is not clear how useful they will prove to be for measuring the properties of slush layers. The transmitted signals must penetrate into the slush layers and the backscattered signals must not be saturated in order for the measurements to be successful. This follows from the fact that both the lower boundary and the water surface must be detected in order for the slush layer thickness to be computed. If this is possible then the accuracy of the estimated thickness depends primarily on how accurately the sound speed in the slush layer is known. The sound speed in slush is thought to be a function of porosity, sound frequency and air content. Marko and Jasek (2010a, b) estimated that sound speeds in slush layers found beneath the ice cover on the Peace River were approximately 15 % lower than the fresh water value of 1403 m/s.

Experiments reported by Williams et al. (1992) on the sea ice skeletal layer (lower porous layer) are considered the seminal study on acoustic properties of porous sea ice. They found that the sound speed is inversely proportional to the slush porosity with values ranging from the sea water sound speed 1450 m/s at the water/ice interface to the pure ice sound speed 3850 m/s (0% porosity). The objective of these experiments was to obtain estimates of the speed of sound in slush layers of varying porosities, and to examine the relationship between the amplitudes of the backscattered acoustic pulses and the porosity.

Experimental Methods

The same basic experimental setup used for the suspended frazil experiments was used for the slush layer experiments. The following experimental procedure was used during all the slush experiments. First the cold room temperature was set to -

10 ºC and the four bottom-mounted propellers were turned on to a speed of 300 rpm. Both the high and the low frequency SWIPS were deployed and set to the lowest available gain of one to minimize the received acoustic energy and decrease the likelihood of data saturation. The different SWIPS parameters used during the slush experiments are summarized in Table A.1.

The experiment was allowed to progress until large frazil flocs had formed in the tank. At that time the propellers were stopped, and the frazil flocs were allowed to float to the surface and form a slush layer. Preliminary experiments showed that slush layers formed in this manner were approximately 2 to 3 cm thick. These thin layers could not be detected by either the high or the low frequency SWIPS. In order to produce thicker layers four Plexiglas paddles were used to push the slush into a 0.5 m by 0.5 m area in the centre of the tank. This resulted in thicker slush layers directly over top of the two SWIPS units (see Fig. A.1). Next, the slush layers were left to stabilize at the surface for approximately 10 minutes and then SWIPS data collection was stopped. Slush layer thickness measurements were made at 9 locations (3 × 3 grid) using a hook-shaped point gauge mounted on top of the tank. The water surface elevation and elevation at the bottom of the slush layer were also recorded. The average slush thickness t_{slush} was computed using the 9 measurements and this average value was used for the calculation of slush porosity and sound speed.

Three sieve samples were then taken, each from different areas of the slush layer (see Fig. A.2). The sieves were 15.5 cm diameter stainless steel sieves, having a cross sectional area of 0.019 m^2 and mesh size of 1.8 mm. The sieves were lowered below the slush layer, moved to an undisturbed spot, and then pulled up vertically to sieve a specific volume of slush. The sieved samples were then weighed and averaged and the porosity, p (%) of the slush was calculated as follows,

$$p = \frac{V_w}{V_{tot}} \times 100 = \frac{V_{tot} - V_i}{V_{tot}} \times 100 = 1 - \frac{(M_i - 7.2)}{A_{sieve} \times t_{slush} \times \rho_i} \times 100 \qquad \text{(A.1)}$$

where, V_{tot} is the total sieved volume (cm^3), V_w is the water volume (cm^3), V_i is the ice volume (cm^3), A_{sieve} is the area of the sieve (cm^2), ρ_i is the density of frazil ice assumed to be 0.92 g/cm^3 and M_i is the average mass of the sieved ice (g). Note that 7.2 g was subtracted from M_i to account for the capillary water attached to the sieve. The slush generated in each experiment was scooped and stored in a cooler sitting in the cold room. The stored slush could then be placed between the paddles in the next experiment to produce even thicker slush layers with lower porosities. Preliminary experiments showed that slush layers comprised of only stored slush (i.e. stored in the cooler) and of a combination of freshly formed and stored slush generated porosities of ~80 to 85%. These porosities always saturated the high frequency SWIPS signals. The saturated signals prevent the detection of the water surface through the slush. Only using freshly formed slush (porosities of ~85 to 90%) could we detect the water surface with the high frequency SWIPS. The backscatter signal from the low frequency was always noisy. Neither the bottom of the slush nor the water surface could be identified from the low frequency signal.

Results and Discussion

Fig. A.3 presents a 2D plot of the processed S_v from the high frequency SWIPS for a typical slush layer experiment. The different stages of the slush layer experiment are also shown. Depth average volume backscatter strength S_{vd} was calculated for the slush layer for each experiment. For the gain setup used during these experiments, S_{vd} ranged from -7.0 to -8.5 dB and from -22.5 to -28.5 dB for the high and low frequency respectively.

Slush porosity was calculated during each experiment using Eq. (A.1); freshly formed slush generated porosities of ~85 to 90%. These porosities are higher than the 35 to 65% porosity reported from field observations of frazil accumulations underneath hanging dams and at river banks. Frazil flocs in these accumulations were compacted by the flow which resulted in these lower porosities.

In order to estimate the sound speed in the slush layer, the water surface must be detected through the slush. The sound speed in slush was estimated using the following,

$$c_{slush} = c_{dep} \times \frac{t_{slush}}{t_{dep}} \quad \text{(A.2)}$$

Where, c_{slush} is the estimated sound speed in slush (m/s), c_{dep} is the sound speed used during deployment (m/s), t_{slush} is the measured slush thickness (m), and t_{dep} is the detected slush thickness (m) with the SWIPS using c_{dep}. Measured slush thicknesses in the tank ranged from ~10 to 15 cm. As illustrated in Fig. A.4a, there is a vertical shift in the detected water surface due the change of sound speed in the slush; t_{dep} and t_{slush} are also shown. The vertical resolution is 1.1 cm and this corresponds to the maximum digitization rate of 64 kHz for both SWIPS units in the vertical. Fig. A.4b shows that for the low frequency, the water surface was not well defined through the slush. Also the bottom of the slush was not detected clearly at this low frequency because of the very high porosity. Therefore, measurements of sound speeds using the low frequency were not possible during these experiments. Table A.2 summarizes the experimental results from the 6 successful slush experiments using only freshly formed slush.

Sound speeds ranging from ~1270 to 1403 m/s were estimated using Eq. (A.2) for slush porosities ranging from ~85 to 90%. There was no clear trend between the measured slush porosities and the estimated sound speeds and backscatter strength. The sound speed was expected to increase in porous slush following the observations of Williams et al. (1992) in porous sea ice layer. Estimated sound speeds in Table A.2 are comparable to ~1200m/s estimated by Marko and Jasek (2010a, b). It is important to note the difference between the formation of the sea ice skeletal layer and the fresh water slush layer. The skeletal layer in sea ice is formed by the removal of dissolved salts from the ice and this forms porous

channels in the ice cover. In fresh water, slush layers are formed by the accumulation of frazil flocs that eventually rise to the surface.

Field tests conducted by ASL[*] suggested that this lower sound speed in fresh water slush layer is due to the presence of microscopic air bubbles. It was observed that when air bubbles are present in the mixture, the sound speed is almost independent of the slush porosity. Air bubbles can be entrained in the river by small scale breaking surface waves. Also as the water in the tank cools, the dissolved oxygen comes out of solution and forms small air bubbles. These air bubbles cannot overcome the turbulence in water and remain suspended because of their small sizes and corresponding small rise velocities. Void fraction of 0.001 % can decrease the sound speed of the mixture by 10 % due to its low bulk compressibility (Crocker, 1998). Such very small concentrations of air bubbles were not visible with the naked eye but their presence would explain the observed slush layer sound speeds. Gherboudj et al. (2007) studied the air inclusions in ice core samples from the Saint François River (Quebec, Canada) and the Athabasca River (Alberta, Canada). They found that the concentration of air inclusions in the ice cover is highly dependent on both the ice type as well as the rate of freezing. In frazil ice, the presence of air inclusions was consistent and air bubbles were found to be irregular in shape with observed diameters ranging from 0.001 to 1.0 cm.

Summary and Conclusions

Frazil slush layers were generated in the frazil tank by the accumulation of frazil flocs at the water surface. Vertical paddles were used to thicken the slush. Slush thicknesses were measured using a point gauge, and slush porosities were measured using a sieving technique. The slush layer thicknesses in the tank ranged from 10 to 15 cm with porosities from 85 to 90%. The low frequency SWIPS data was noisy and as a result no quantitative slush thickness or sound speed measurements were possible at this frequency. Using stored slush with

[*] Personal communication with John Marko, ASL (January 2010)

porosities below 85% always resulted in saturated high frequency SWIPS signals. This fact limits the ability of the high frequency SWIPS to measure field generated slush with reported porosities between 35 and 65%. Using only freshly generated slush, sound speeds in the slush were found to range from 1270 to 1403 m/s. The sound speeds below 1403 m/s are probably due to the presence of tiny fraction of air bubbles in the slush. There was no clear trend between the measured slush porosity and thickness, and the sound speed and the SWIPS backscatter signal levels. The sound speed is also dependent on the sound frequency; therefore modification should be done to the current gain board on the low frequency unit to investigate the variation of sound speed as a function of the sound frequency.

Tables

Table A.1 SWIPS parameters used for the slush experiments.

Parameter	**High Freq**	**Low Freq**
pulse length τ (μs)	17	68
gain	1	1
ping frequency (Hz)	1	1
sensor frequency (Hz)	1	1
sound speed c_{dep} (m/s)	1403	1403
input voltage (V)	15	15

Table A.2 Summary of results of the slush layer experiments.

Exp#	M_{ice} **(g)**	t_{slush} **(cm)**	p **(%)**	**High Frequency**			**Low Frequency**		
				t_{dep} **(cm)**	c_{slush} **(m/s)**	S_{vd} **(dB)**	t_{dep} **(cm)**	c_{slush} **(m/s)**	S_{vd} **(dB)**
97	253	14.2	90.1	15.3	1302.1	-7.6	-	-	-23.6
98	227	10.9	88.5	12.0	1274.4	-8.5	-	-	-28.5
99	275	12.0	87.2	12.0	1403.0	-7.2	-	-	-22.5
100	214	12.1	90.2	13.2	1286.1	-7.1	-	-	-25.3
101	253	9.9	85.8	9.9	1403.0	-8.2	-	-	-26.8
105	236	11.0	88.1	-[*]	-	-7.0	-	-	-22.7

[*] The high frequency SWIPS signal attenuated before reaching the surface; therefore measurements of sound speed were not possible for this experiment.

Figures:

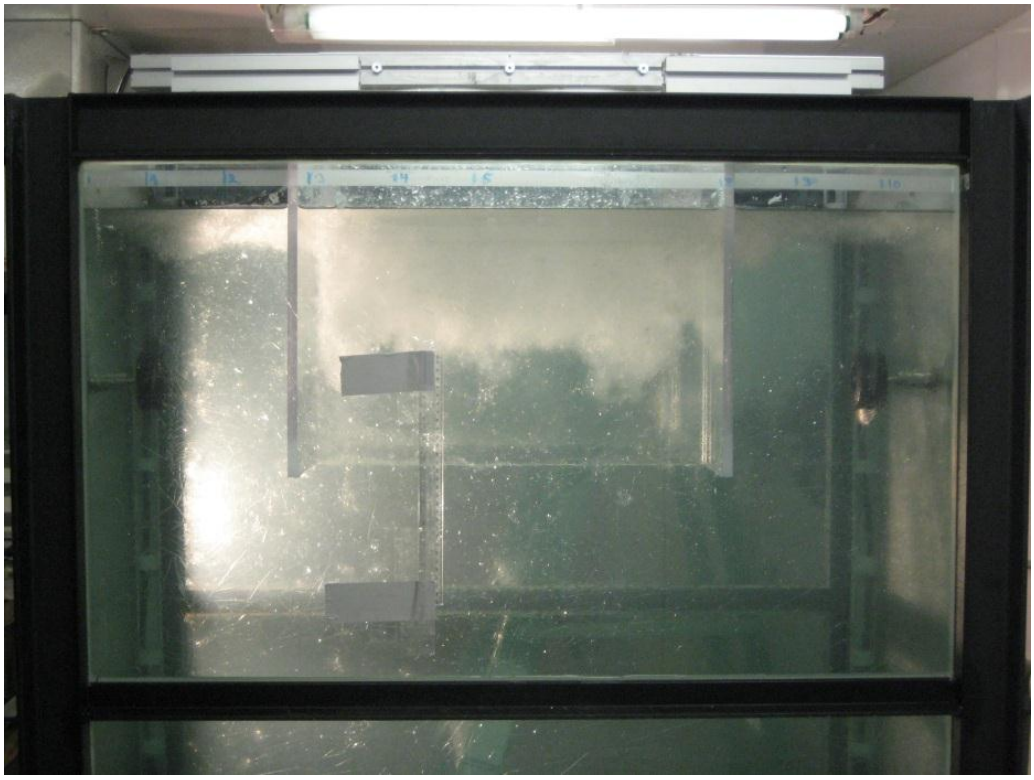

Fig. A.1. Image of the top half of the frazil tank with the slush layer formed at the surface. The slush has been squeezed to the center using Plexiglas paddles.

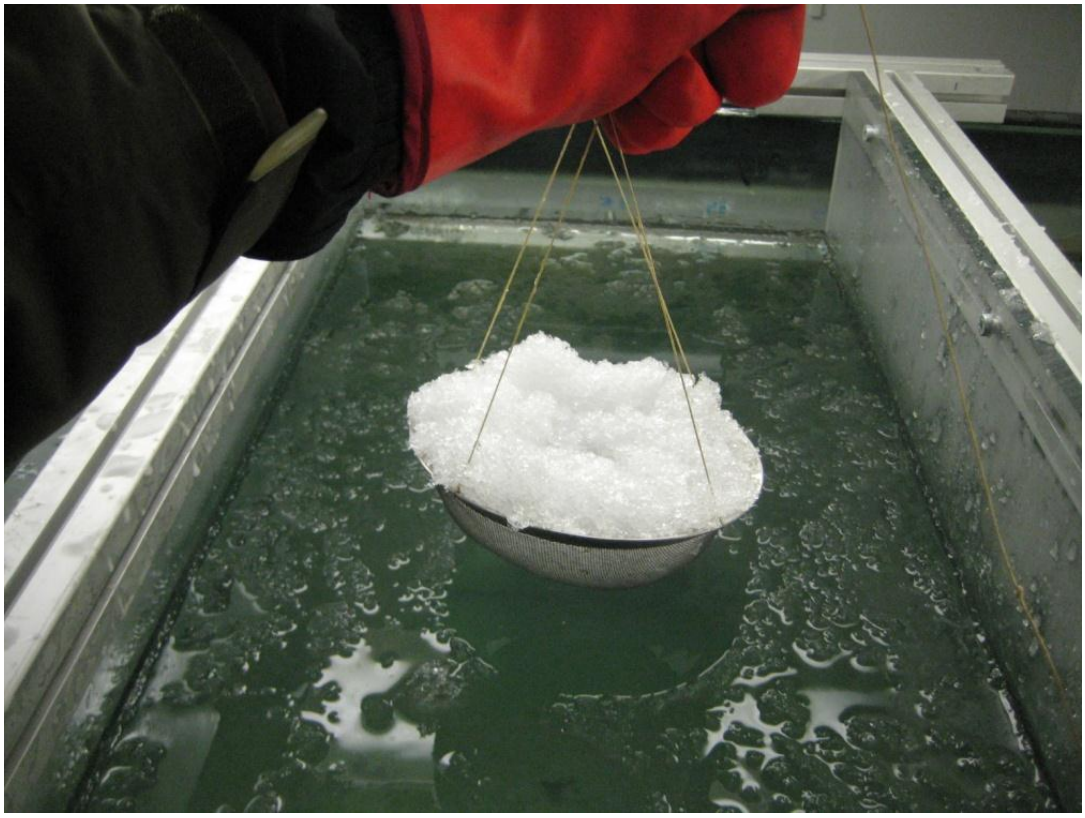

Fig. A.2. A picture taken from the tank top showing a sample of sieved slush to be used for porosity calculations.

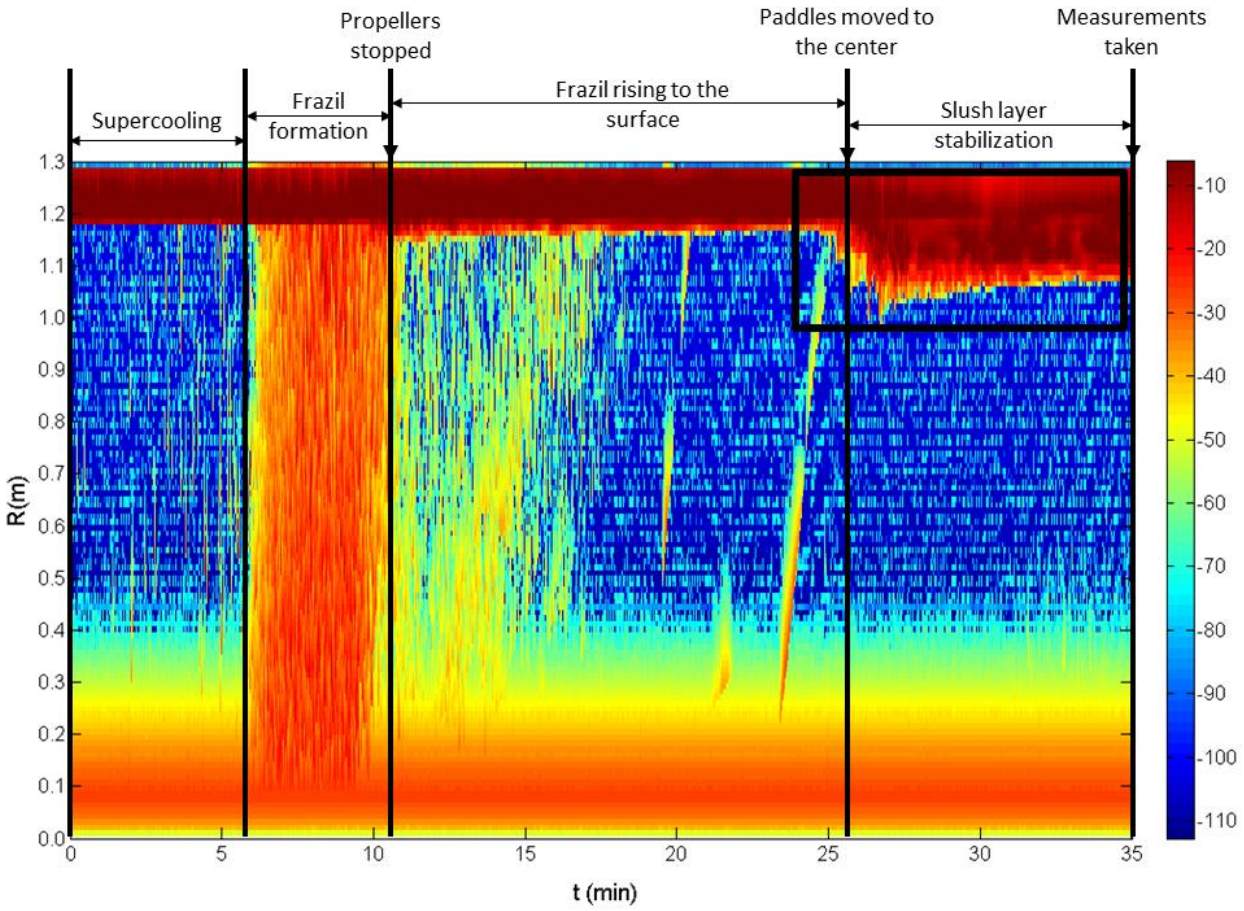

Fig. A.3. 2D plot showing different steps of a typical slush experiment (Exp#98); range R (m) versus time t (min) and processed S_v (dB) color coded. A box is pointing at the stabilizing surface slush layer.

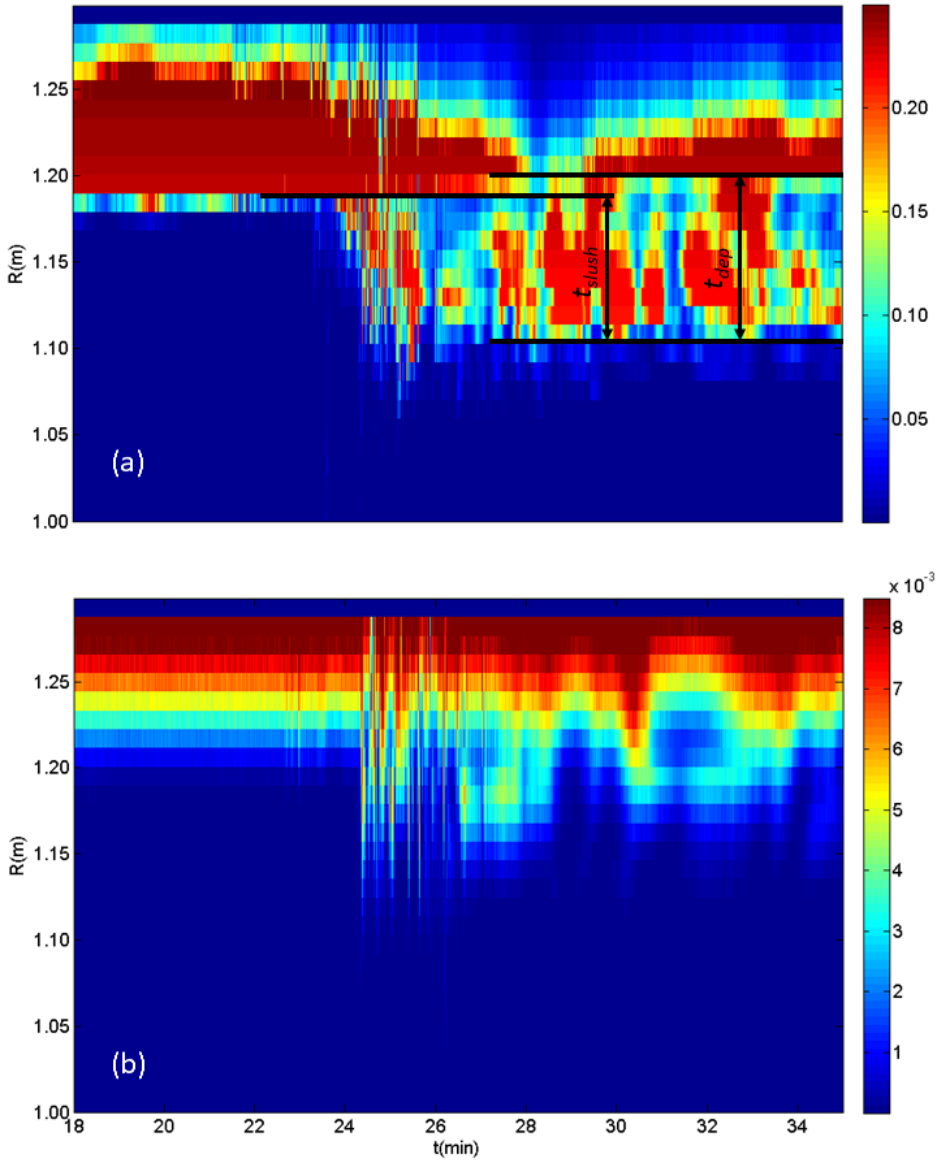

Fig. A.4. 2D plot of processed s_v (m^{-1}) color coded for a typical slush experiment (Exp#98) zooming at the stabilized slush layer; range R (m) versus time t (min) for (a) the high frequency, and (b) for the low frequency. Note: t_{slush} and t_{dep} are illustrated for the high frequency.

References

Daly, S.F., 1991. Frazil Ice Blockage of Intake Trash Racks. Cold Regions Technical Digest No. 91-1

Hanley, T. O'D., Michel, B., 1977. Laboratory formation of border ice and frazil slush. Can. J. Civ. Eng. 4:153-60.

Beltaos, S. and Dean, A.M., 1981. Field investigations of a hanging ice dam. Proceedings of the 6th IAHR Symposium, 1981, Quebec, Canada, 475-488.

Dean, A.M., 1977. Remote sensing of accumulated frazil and brash ice. Proceedings of the third National Hydrotechnical Conference, Can. Soc. Civ. Eng. Quebec, pp. 693–704.

Lawson, D. E., Brockett, B. E., 1990. In-situ sampling and characterization of frazil ice deposits. Cold Regions Science and Technology, Volume 17, Issue 3, Pages 193-205

Dean, A.M., 1986. Field techniques for obtaining engineering characteristics for frazil ice accumulations. Proceedings of the 8th IAHR Ice Symposium, 1986, Iowa City, USA.

Andres, D.D. and Spitzer, M.O., 1989. Inter-station storage losses during freeze-up on large rivers. Proceedings of the 23rd IAHR Symposium, 1989, Ottawa, Canada.

Marko, J.R., and Jasek, M., 2010a. Sonar Detection and Measurements of Ice in a Freezing River I: Methods and Data Characteristics. Cold Regions Science and Technology. 63, 121–134.

Marko, J.R., and Jasek, M., 2010b. Sonar Detection and Measurement of Ice in a Freezing River II: Observations and Results on Frazil Ice. Cold Regions Science and Technology. 63, 135–153.

Williams, K.L., G.R. Garrison and P.D. Mourad, 1992. Experimental examination of growing and newly submerged sea ice including acoustic probing of the skeletal layer. J. Acoust. Soc. Am., 92, 2075-2092.

Crocker, J. M., 1998. Handbook of Acoustics. Wiley-Interscience Inc., New York, USA. 1461p.

Gherboudj, I.A., M. Bernier, F. Hicks, and R. Leconte, 2007. Physical Characterization of Air Inclusions in River Ice. Journal of Cold Regions Science and Technology, 49(3): 179-194.

Appendix B. Heat Transfer Modeling of Frazil Experiments

This appendix summarizes a complementary analysis of the laboratory data using a simple heat transfer model. The equations used to model the laboratory conditions and estimate the frazil concentrations are listed below together with the associated assumptions.

The energy equation for ice and water mixture assuming conductive heat transfer only from the surface can be expressed as follow:

$$\frac{d(D_{equ}\, e_T)}{dt} = \frac{-Q_{wa}}{\rho_w} \qquad \text{(B. 1)}$$

Where: D_{equ} = equivalent water depth (m) for surface heat transfer only, e_T= total energy consumed by water cooling and ice formation (J/kg), t = time (sec), Q_{wa} = net rate of heat exchange per unit area between water and air from all sides of the tank (W/m^2), ρ_w = density of water (kg/m^3)

The tank is constructed from 2 glass sides (1.25*1.2 m), 2 stainless steel sides of (0.8*1.25 m), stainless steel bottom of (1.2*0.8 m), and in direct contact with air from the top (1.2*0.8 m). The heat is being transferred from all the sides. The equivalent water depth D_{equ} is calculated as the depth of a rectangular prism having a volume equal to the volume of water in the tank and a base area equal to the total tank sides' areas.

Using a simplified energy budget equation, Q_{wa} is expressed as,

$$Q_{wa} = h_{all}\,(T_w - T_a) \qquad \text{(B. 2)}$$

Where: h_{all} = overall heat transfer coefficient per unit area between water and air (W/m^2/ºC) from all tank sides, T_w = water temperature (ºC), and T_a = air temperature (ºC).

For two or more heat transfer processes from different surfaces acting in parallel, heat transfer coefficients simply add. Note: this method does not take into account the effect of forced convective heat transfer due to flow turbulence. Therefore the overall heat transfer coefficient, h_{all} (W/m^2/ºC) can be calculated as follow

$$\frac{1}{h_{all} \times A_{tot}} = \sum_i \left(\left(\frac{1}{h_i} + \frac{t_{s_i}}{K_i} \right) \times \frac{1}{A_i} \right) \quad \text{(B. 3)}$$

where, A_{tot} (m^2) is the total areas of all tank sides, i is the number of different tank sides, h_i (W/m^2/ºC) is the heat transfer coefficient for each individual material, A_i is the contact area (m^2) of water with each surface, K_i (W/m/°C) is the thermal conductivity of each material, and t_{si} is the wall thickness (m) for each tank side. For D_{equ} of 0.1734 m, the h_{all} was 12.5 (W/m^2/ºC).

The total net energy consumed by cooling the water and forming the ice is calculated as follows,

$$e_T = C_p(1 - M_i)T_w - \frac{\rho_i}{\rho_w} M_i L_i \quad \text{(B. 4)}$$

Where: C_p = specific heat capacity of water (J/kg/ºC), M_i = volumetric concentration of frazil ice particles (m^3/m^3), ρ_i = density of ice (kg/m^3), L_i = latent heat of ice (J/kg)

For small M_i equation (B.4) above can be approximated and water temperature is calculated as,

$$T_w \approx \frac{e_T}{C_p} \quad \text{(B. 5)}$$

Putting equations (B.4) and (B.5) into equation (B.1), the energy equation can be expressed as,

$$\frac{d(D_{equ}\, e_T)}{dt} = \frac{-h_{all}\,\left(\frac{e_T}{C_p} - T_a\right)}{\rho_w} \tag{B.6}$$

Discretizing equation (B.6) in time,

$$\frac{D_{equ}\,(e_T^{n+1} - e_T^n)}{\Delta t} = \frac{-\theta\, h_{all}\left(\frac{e_T^{n+1}}{C_p} - T_a\right)}{\rho_w} - \frac{(1-\theta) h_{all}\left(\frac{e_T^n}{C_p} - T_a\right)}{\rho_w} \tag{B.7}$$

Where: n is the time discretization counter, Δt is the time step (sec), and θ is the implicitness coefficient usually taken as 0.5.

Rearranging equation (B.7) and solving for e_T^{n+1}

$$e_T^{n+1} = \frac{\left[\left(D_{equ} - \frac{(1-\theta)\Delta t\, h_{all}}{\rho_w C_p}\right) e_T^n + \frac{\Delta t\, h_{all} T_a}{\rho_w}\right]}{\left(D_{equ} + \frac{\theta\, \Delta t\, h_{all}}{\rho_w\, C_p}\right)} \tag{B.8}$$

Then from equation (B.4), isolating T_w and discretizing in time, we can calculate water temperature for the next time step as follow,

$$T_w^{n+1} = \frac{e_T^{n+1} + \frac{\rho_i}{\rho_w} M_i^n L_i}{C_p(1 - M_i^n)} \tag{B.9}$$

Conservation of mass for suspended frazil particles is expressed as,

$$\frac{d\,(D_{equ}\, M_i)}{dt} = \frac{-Q_{wi}}{\rho_i L_i} \tag{B.10}$$

Where: Q_{wi} = net rate of heat exchange between water and ice (W/m^2) and can be calculated as follow,

$$Q_{wi} = h_{wi}(T_i - T_w) \tag{B.11}$$

Where: T_i = ice temperature taken as 0ºC, h_{wi} = the heat transfer coefficient between water and ice (W/m^2/ºC). Discretizing equation (B.11) in time,

$$Q_{wi}^{n+1} = h_{wi}^{n+1}(-T_w^n) \quad \text{(B. 12)}$$

and h_{wi} can be calculated as follow,

$$h_{wi} = \alpha\,(M_i + M_o) \quad \text{(B. 13)}$$

Where: M_o = the initial seeding concentration of frazil to start the frazil production (m^3/m^3), α is a coefficient equal to 71063348 obtained from fitting equation (B.7) to the experimental data reported by Ye and Doering (2004).

Discretizing equation (B.13) in time,

$$h_{wi}^{n+1} = \alpha\,(M_i^n + M_o) \quad \text{(B. 14)}$$

Discretizing equation (B.10) in time,

$$\frac{D_{equ}(\,M_i^{n+1} - M_i^n)}{\Delta t} = \frac{-\theta\, Q_{wi}^{n+1}}{\rho_i L_i} - \frac{(1-\theta)Q_{wi}^n}{\rho_i L_i} \quad \text{(B. 15)}$$

Therefore, instantaneous frazil ice concentration M_i^{n+1} is calculated from equations (B.12), (B.14), and (B.15) as follows,

$$M_i^{n+1} = M_i^n - \frac{\theta\,\Delta t\, Q_{wi}^{n+1}}{D_{equ}\,\rho_i L_i} + \frac{(1-\theta)\Delta t\, Q_{wi}^n}{D_{equ}\,\rho_i L_i} \quad \text{(B. 16)}$$

Using equation (B.16), the frazil concentration was calculated as a function of time and the initial seeding concentration. The computed concentrations and rate of frazil production were found to be significantly dependent on the amount of initial seeding, something that could not be controlled in the experiments. Fig. B.1 show the experimental results (T_{sp} (°C) and C (%)) versus time of supercooling, t_{sp} (min) together with the heat transfer model outputs for different initial seeding concentration M_o of 1E-4, 1E-7, and 1E-12.

An alternative technique has been tried to estimate frazil concentrations from the measured water temperatures from each experiment. The measured rate of cooling dT/dt (ºC/min) during each experiment together with the supercooling duration, t_{sp} (min) (which is the time from the onset of supercooling until the frazil was sampled and sieve concentration was measured), were used to predict the corresponding frazil concentration from the heat transfer model. A comparison between measured (using sieving technique) and modeled (using the heat transfer model) frazil concentrations at the end of each experiment is presented in Fig. B.2. As shown in Fig. B.2, the fact that measured frazil concentrations with the sieve were not correlated with the duration or degree of supercooling, prevented the modeled frazil concentration from matching with the measured concentrations at various range of concentrations.

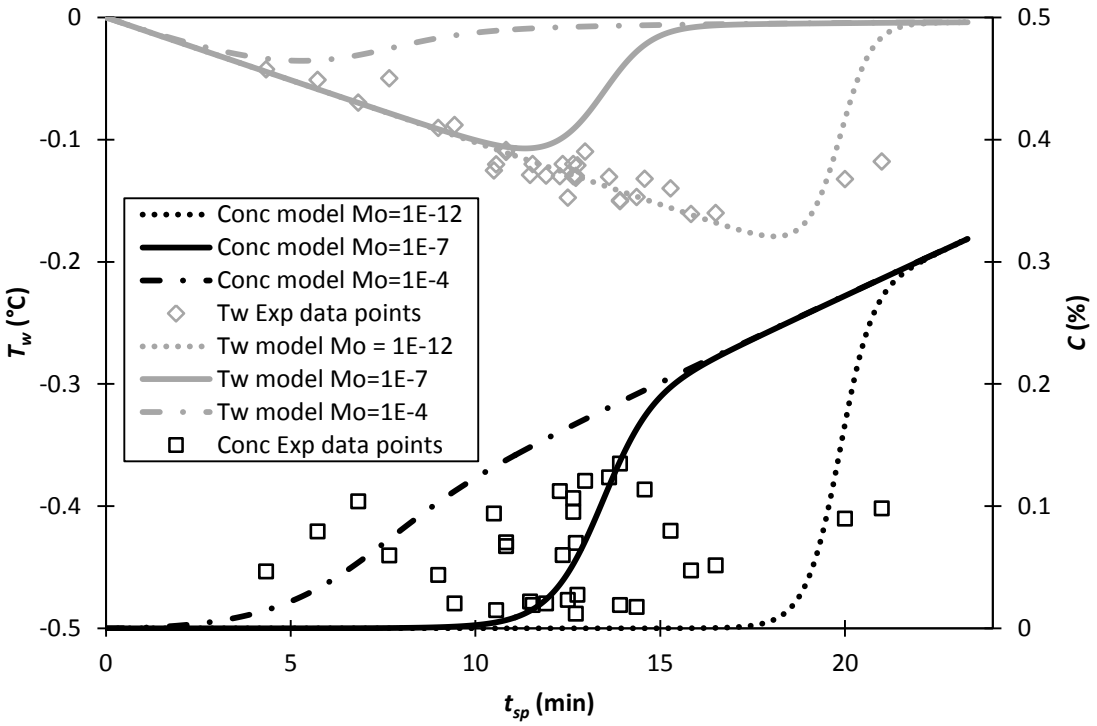

Fig. B.1 Comparison of experimental supercooling temperatures and concentrations with the modeled supercooling curve and the corresponding frazil production curve for different initial seeding concentrations, M_o, of 1E-4, 1E-7, and 1E-12. Water temperature, T_w (°C), is on left y-axis and frazil concentration, C (%), is on right y-axis, versus time t_{sp} (min) from the start of the supercooling.

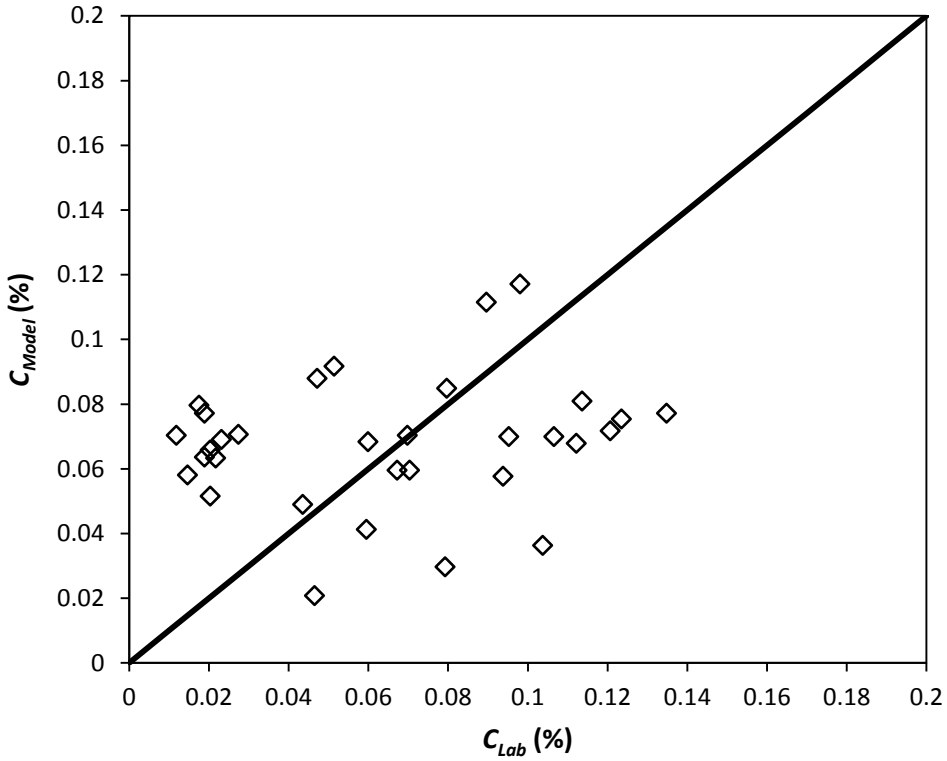

Fig. B.2 Comparison between measured frazil concentration C_{Lab} (%), and the corresponding modeled concentration C_{Model} (%) using the heat transfer model.

References

Ye, S.Q., Doering, J., and Shen, H.T., 2004. A laboratory study of frazil evolution in a counter-rotating flume. Canadian Journal of Civil Engineering, 31(6), 899-914.

Andrishak, R. and Hicks, F.E., 2008. Simulating the Effects of Climate Change on the Winter Regime of the Peace River. Canadian Journal of Civil Engineering, 35: 461-472.

Ye, S.Q. and Doering, J. 2004. Simulation of the supercooling process and frazil evolution in turbulent flows. Canadian Journal of Civil Engineering, 31, 915-926.

Ettema, R., Karim, M.F., Kennedy, J.F., 1984. Laboratory Experiments on Frazil Ice Growth in Supercooled Water. Cold Regions Science and Technology, 10: 43-58.

Appendix C. Matlab Codes Developed for Processing and Analyzing Dataset

A digital copy of the MATLAB programs is available on attached DVD.

#	**Code Name**	**Description**
1	EnvelopeDetector_correction	Correction to the low and high frequency raw data to account for the non-linearity of the envelope detector of both sonar units
2	RiseTimeResponse_Correction	Correction to the high frequency raw signal to have the same response time as the low frequency signal
3	frazil_exp_processing	Processing the raw sonar data from the frazil experiments to compute S_v (dB) from the high and the low freq including: signal corrections (envelope detector and response time), depth averaging and filtering.
4	EXP_DATA_REGRESSION	Developing regressions equations to fit the logarithmic correlation equation to the sonar data and the corresponding measured concentration using the least square technique for the low and high frequency data.
5	microscope_size_distribution_histograms	Generating histograms of particles sizes from microscope images per experiment and for a lumped histogram from all experiments

6	ImageProcessing_frazilconc_particleSize	Algorithm to compute frazil concentration and particle size distribution from laser images taken during the frazil experiments (not used in this study)
7	FieldDataProcessing_24hr	The main field processing algorithm that calculates: pan draft, lengths and surface ice concentration, and processes the raw sonar signal to compute the profiles and depth average time series of volume backscatter strength. Note: the algorithm can only process a maximum of 24 hr. data due to the limited capacity of the PC used for the processing
8	Aqdp_velocity_mean_max_surf	The algorithm that extracts the mean, max and surface velocity from the AquaDopp data
9	plot_raw_counts	Plots 2D profiles of the raw counts from the field deployment, the hydro-meteorological conditions, and the computed pan drafts and lengths, and surface ice concentration
10	Concatenate_ratio_2009110100_2010011309	concatenate the ratio of the high to the low frequency signal from individual 24 hrs chunks of the processed signal
11	Concatenate_aqdp_and_weather_2009110100_2010011309	concatenate the aquadopp and weather station data from individual 24 hrs chunks of the processed data
12	Concatenate_high_and_low_variables_2009110100_201001	concatenate the processed depth averaged sonar signal from the high to the low

	1309	frequency from individual 24 hrs chunks of the processed signal
13	Downsampling_FieldData	smoothing and downsampling pan drafts, lengths, and surface concentrations, estimated from the sonar data gathered during the field deployment to 30 minute moving average from 1 Hz sampling freq
14	plot_season_30min_avg	Plotting the 30 minutes moving average outputs for the field data including: air temp, water temp, water depth, depth averaged velocity, surface concentration, pan drafts, pan lengths, and the ratio of pan draft over pan length
15	high_Vs_low_Cs_tp_lp_hist	Comparing histograms of pan drafts, lengths, and surface concentrations from the high and the low freq
16	surf_vel_Vs_Cs	extracting and plotting the mean and surface velocity together with the corresponding surface concentration for phase I, II, and III
17	Frazil_event_processing	Processing field sonar signal during frazil events to compute profiles and depth averaged volume backscatter strength
18	Downsampling_Frazil_data	smoothing and downsampling processed sonar data during frazil events to 1 minute moving average from 1 Hz sampling freq
19	Frazil_events_plotting	plotting 2D profiles and time series of depth average volume backscatter strength from

		the field deployment during frazil events
20	scattering_models	formulation of the scattering models: for sphere: Rayleigh (1896), Anderson (1950), Johnson (1977); prolate spheroid, Stanton (1989); and disk, Coussius (2002)
21	scattering_models_sensitivity_DiameterToThickness_and_angle	The effect of changing the diameter to thickness ratio and the angle of orientation on modeling the sound scattering using the sphere, prolate spheroid, and the disk model
22	scattering_models_sensitivity_compressibility	The effect of changing the compressibility (sound speed) on modeling the sound scattering using the sphere, prolate spheroid, and the disk model.
23	EXP_DATA_REGRESSION_sensitivity_DiameterToThickness	The effect of changing the diameter to thickness ratio on modeling the laboratory data
24	EXP_DATA_REGRESSION_sensitivity_compressibility	The effect of changing the compressibility (sound speed) on modeling the laboratory data
25	frazil_exp_analysis	Applying scattering models to sonar data from individual frazil experiment
26	Frazil_event_analysis	Estimating the frazil concentration from the sonar signal using laboratory regression equations, and deducing the corresponding particle sizes using scattering models

27	Supercooling_and_Frazil_Production_HeatTrans	An Excel spreadsheet to estimate frazil concentration in laboratory setup using the simplified heat transfer model in Appendix B